Turbulent Mixing in Stably Stratified Flows

Final Report for Office of Naval Research Grant
N00014-04-1-0687

David A. Hebert and Stephen M. de Bruyn Kops

March 1, 2008

This final report for Office of Naval Research Grant N00014-04-1-0687 is substantially similar to: D. A. Hebert, *Turbulent Mixing in Stably Stratified Flows*, PhD Dissertation, University of Massachusetts Amherst, 2007. It is submitted with approval of the copyright holder of that publication.

REPORT DOCUMENTATION PAGE

Form Approved
OMB No. 0704-0188

1. REPORT DATE *(DD-MM-YYYY)*	2. REPORT TYPE	3. DATES COVERED *(From - To)*
01-03-2008	Final	JUN 2004 - DEC 2007

4. TITLE AND SUBTITLE

Turbulent Mixing in Stably Stratified Flows

5a. CONTRACT NUMBER

5b. GRANT NUMBER
N00014-04-1-0687

5c. PROGRAM ELEMENT NUMBER

6. AUTHOR(S)

Hebert, David A
de Bruyn Kops, Stephen M

5d. PROJECT NUMBER

5e. TASK NUMBER

5f. WORK UNIT NUMBER

7. PERFORMING ORGANIZATION NAME(S) AND ADDRESS(ES)
University of Massachusetts Amherst
70 Butterfield Terrace
Amherst, MA 01003

8. PERFORMING ORGANIZATION REPORT NUMBER
n/a

9. SPONSORING/MONITORING AGENCY NAME(S) AND ADDRESS(ES)
Office of Naval Research
875 North Randolph Street
Arlington, VA 22203-1995

10. SPONSOR/MONITOR'S ACRONYM(S)
ONR

11. SPONSOR/MONITOR'S REPORT NUMBER(S)
n/a

12. DISTRIBUTION/AVAILABILITY STATEMENT

Approved for Public Release; distribution is Unlimited

13. SUPPLEMENTARY NOTES

14. ABSTRACT High resolution direct numerical simulations are used to investigate the dynamics of turbulence in flows subject to strong stable stratification, which are common in natural settings. Results are presented for two categories of simulations, uniform and non-uniform density stratification. For all simulated flows, the density stratification was held constant in time, and there was no ambient shear. Flows with uniform density stratification are first analyzed to help provide clear insight to physical processes, followed by flows with non-uniform density stratification which better represent the stratification occurring in nature.

15. SUBJECT TERMS
Turbulence, mxing stable stratification

16. SECURITY CLASSIFICATION OF:			17. LIMITATION OF ABSTRACT	18. NUMBER OF PAGES	19a. NAME OF RESPONSIBLE PERSON
a. REPORT	b. ABSTRACT	c. THIS PAGE			de Bruyn Kops, Stephen M.
UU	UU	UU	SAR	101	19b. TELEPHONE NUMBER *(Include area code)* 413 545 0206

Contents

List of Tables

List of Figures

Chapter 1

Introduction

Turbulent fluid motions are typically characterized by several features including randomness in both space and time, vorticity, an energy cascade from large to small scales where energy dissipation occurs, and a large increase in diffusion of properties (i.e., temperature, salinity) compared with molecular diffusion [McDougal et al., 1988]. These features of turbulent flows are usually caused by some sort of flow instability. In homogeneous flows, instabilities are usually related to the Reynolds number, which can be thought of as the ratio of inertial to viscous forces. As Reynolds number increases, inertial forces overcome viscous dissipation, and instabilities grow until they overtake the flow. In a density stratified flow, a gravity force is present which acts as a stabilizing force, giving rise to a buoyancy force that must be overcome as well as viscous forces for the fluid to become turbulent. This suggests that the Froude number, which can be considered a ratio of inertial to gravity forces, will also be important in determining if a flow becomes turbulent. Moreover, the addition of a buoyancy force helps create a situation where the transition to turbulence is marked by intermittent turbulent patches in the flow, rather than a smooth transition throughout the flow as in a homogeneous flow. The characterization of this intermittency of turbulence within a density stratified flow is an area of active research.

When one considers the fact that the atmosphere and ocean are density stratified fluids, it can be said that the vast majority of the flows on Earth take place in stratified fluids. They occur in the ocean below the mixed layer, in the stratosphere, and in the nocturnal atmospheric boundary layer (at night the sun does not provide energy to mix the atmosphere near the Earth). Turbulence often occurs in these flow regimes due to free shear instabilities (e.g., Kelvin-Helmholtz), internal wave breakdown, and wakes of structures such as islands, mountains, and submarines. Turbulence in these areas has impact ranging from weather prediction to pollution dispersion. It is this area of geophysical turbulence that will be the focus of this dissertation.

An important effect of stratification is that gravity allows internal gravity waves to form. Internal waves have the ability to propagate energy throughout the flow [e.g., Riley and Lelong, 2000, Slinn and Riley, 1996, Winters et al., 1995]. Turbulence caused by the breakdown of internal gravity waves can affect the mixing of heat and elements within the fluid [Lombard and Riley, 1996a,b, Slinn and Riley, 1996, 1998]. While important in density stratified flows, breakdown of internal waves will not be examined in this study. Rather, the focus of this study will be turbulence formed by free shear instabilities by flows dominated by vortical modes. The remainder of this chapter contains description of density stratification that occurs in nature, followed by a literature review of density

stratified flows. Chapter 2 contains theoretical considerations including a derivation of the equations of motion and a description of the Boussinesq approximation. Chapter 3 contains results of studies that investigate vertical shear and dissipation rate, buoyancy Reynolds number, and parameterization of turbulence using Taylor-Green simulations and uniform density stratification. Chapter 4 contains results of investigations that study the effect of non-uniform density gradient on simulated wake flow, including a method of calculating potential energy in non-uniform stratification. Chapter 5 contains conclusions and proposed future work.

Notation Several equations are introduced in this document, and often it is difficult to distinguish between dimensional and nondimensional quantities. As such, a convention is adopted in this document where $\tilde{(\cdot)}$ is used to denote dimensional quantities, while unmarked quantities (i.e., no tilde) will denote nondimensional quantities.

1.1 Density Stratification in Fluids

In the atmosphere and ocean, distinct layers form that are characterized by the rate of temperature (and hence density) change with height. The atmosphere is typically separated into four layers; starting from the Earth's surface and increasing in height these layers are the troposphere, stratosphere, mesosphere, and thermosphere [e.g., Brasseur and Solomon, 1984, Labitzke and van Loon, 1999, Lutgens and Tarbuck, 1995]. The ocean is typically divided into three regions; starting from the ocean surface and increasing in depth these layers are the mixed layer, the thermocline, and deep water [Colling, 2002, Gill, 1982]. This section contains a brief description of each layer and its significance to geophysical turbulence, and the reader is referred to the aforementioned references for further discussion on the atmosphere and ocean.

1.1.1 Atmosphere

The troposphere is the lowest layer in the atmosphere. It varies in height, spanning from the Earth's surface to approximately 18km over the tropics, while spanning to approximately 10km over the Earth's poles. The troposphere contains approximately 80% of the total air mass of the Earth, and is where all weather phenomenon takes place. During the day solar heating of the Earth's surface give rise to convection currents in the troposphere, causing the troposphere to be well mixed. At night solar heating ceases, and radiative cooling causes a stable density stratification layer to form in the lower 3-5km of the troposphere. Hence, this layer is referred to as the nocturnal boundary layer.

The adiabatic change in temperature with height is called the lapse rate, $\widetilde{G}$, and is defined as [Gill, 1982, p.50]:

$$\widetilde{G} \equiv -\frac{\Delta\widetilde{T}}{\Delta\tilde{z}} \tag{1.1}$$

$$\widetilde{G} = \tilde{g}\tilde{\alpha}\widetilde{T}/\tilde{c}_p\,, \tag{1.2}$$

where $\tilde{g}$ is the gravitational acceleration, $\widetilde{T}$ is the temperature, and $\tilde{c}_p$ is the specific heat, $\widetilde{\alpha}$ is the thermal expansion coefficient at constant pressure $\tilde{p}$, and humidity (or salinity in the ocean) $\widetilde{S}$:

$$\widetilde{\alpha} = -\frac{1}{\tilde{\rho}}\frac{\partial\tilde{\rho}}{\partial\widetilde{T}}\bigg|_{p,S}\,. \tag{1.3}$$

Since there is a negative sign in front of $\widetilde{G}$ in (1.1), and altitude is measured from the ground upwards, $\widetilde{G}$ is a measure of the *decrease* in temperature with height. $\widetilde{G}$ can (and does) become negative (signifying an increase in temperature with altitude), particularly in the stratosphere and thermosphere. $\widetilde{G}$ of the troposphere is taken on average to be 6.5°C/km, but can vary locally and depends on humidity content. For example, the nocturnal boundary layer is stably stratified, and has a negative $\widetilde{G}$. Also, it is possible for cooler air to be trapped near the Earth's surface, resulting in a locally stable stratification layer with positive $\widetilde{G}$. An area of cooler air trapped near the surface is termed a thermal inversion, and can cause pollutants and smog to be trapped near the Earth's surface instead of being convected away from the surface. Thermal inversions commonly occur when cool, moist air from the ocean blows over land and when a warm front moves into a region, trapping low temperature underneath. Westerly winds off the Pacific Ocean make Los Angeles an ideal location for temperature inversions to form, causing the city's famous smog.

The upper bound of the troposphere is the tropopause. The tropopause is marked by a sharp change in $\widetilde{G}$, and signifies the boundary between the troposphere and stratosphere. The location of the tropopause decreases in altitude from approximately 18km in the tropics to approximately 10km near the poles.

The stratosphere spans from the tropopause to approximately 50km above the Earth's surface, and with the troposphere contains 99% of the Earth's air mass. The lower 2-10km of the stratosphere is near isothermal (i.e., $\widetilde{G}$ is near 0°C/km), while above 20km $\widetilde{G}$ becomes negative (increase in temperature with height). The negative $\widetilde{G}$ is believed to be caused by the absorption of ultraviolet radiation from the sun by ozone. Since density decreases with temperature for most (if not all) gases, the increase in temperature with height causes a very stable density stratification (hence the name stratosphere). The stable stratification acts as a barrier to vertical currents from the troposphere and inhibits vertical motion within the stratosphere. Such inhibition of vertical motion will result in motions to preferentially grow in the horizontal, which is of interest regarding mixing of elements and chemical reactions that take place in the stratosphere.

The area where $\widetilde{G}$ becomes positive again is called the stratopause, and marks the separation between the stratosphere and the mesosphere.

The mesosphere and thermosphere, while playing vital roles in heat absorption from the sun, are uninteresting from a fluid mechanics perspective. The mesosphere ranges from approximately 50km to 85km, while the thermosphere ranges from 85km to 500km. The lapse rate in the mesosphere is approximately 2°C/km, while in the thermosphere temperature increases with height as solar photons are absorbed. It is interesting to note that the northern lights occur in the thermosphere, and that the international space station has a stable orbit in the upper thermosphere

1.1.2 Ocean

The mixed layer of the ocean varies in depth, spanning from the ocean surface to a depth of approximately 10m near the poles, 200m in the mid-latitudes, and 50m-100m in the tropics. This layer is called the mixed layer because wind and waves cause it to be well mixed, resulting in temperature and salinity profiles that are close to uniform. Nearly all sunlight is absorbed in the mixed layer, causing temperatures in excess of 30°C.

The lapse rate $\widetilde{G}$ of seawater is much smaller than that of the atmosphere, since air is much more compressible that seawater. $\widetilde{G}$ has a typical value of 0.125°C/km, and ranges between 0.1 and 0.2°C/km [Fofonoff and Millard, 1983, p.38]. Note that $\widetilde{G}$ is positive for

the ocean, but marks decrease in temperature with depth, since depth is measured from sea level downward from the sea surface (as opposed to the atmosphere where height is measured upward from the surface).

The thermocline ranges from the bottom of the mixed layer to approximately 1000m. The region is called the thermocline because temperature drops rapidly, as much as 40°C/km near the top of the layer, cooling the thermocline to near 10°C at its lower boundary. This drop in temperature causes an increase in density with depth, hence the region is sometimes referred to as the pycnocline. Since density increases with depth, the thermocline is stably stratified. Since the thermocline is a link between the surface and the deep ocean, the dynamics of the thermocline are important and play a role in such topics as pollution dispersion, motion of small food sources (e.g., plankton), and heat dissipation between the surface and deep ocean.

The deep ocean extends from the bottom of the thermocline to the ocean floor. In the deep ocean temperature and salinity (and hence density) are relatively uniform. Interestingly, local patches of high density water are formed at the surface in cold regions including the North Atlantic off the coast of Greenland and in the Antarctic near the Ross and Weddell Seas where surface water freezes. When ocean water freezes it is fresh water that converts to solid mass, leaving a higher salinty, higher density fluid. (This process is called brine rejection [Colling, 2002, p.213]). These cold, high density sources of water sink from the surface and through the thermocline, forming a convective current. This convective current, along with wind driven currents, is referred to as the "conveyor belt," and helps bring water from the deep ocean to the surface in the mid-latitude Pacific. The rate of travel along the conveyor belt is on the order of 1000 years.

1.2 Review of Previous Work

1.2.1 Wake turbulence in stratified fluids

Wakes are generated when there is relative motion between a body and adjacent fluid. Wakes in stratified fluid can be found in many settings, including such as those generated by airplanes, and submarines, mountains, and buildings. When analyzing wakes in stratified fluids, the Froude (F) and Reynolds (Re) numbers are typically defined in terms of the object size and velocity. Many experiments involve towing a sphere in a tank containing a density stratified fluid, leading to common F and Re definitions:

$$\mathrm{F} = \frac{\widetilde{U}}{\widetilde{\mathrm{N}}\widetilde{R}}, \quad \mathrm{Re} = \frac{\widetilde{U}\widetilde{R}}{\tilde{\nu}},$$

where $\widetilde{U}$ is sphere velocity, $\widetilde{R}$ is sphere radius, and $\widetilde{\mathrm{N}} = \tilde{g}/\tilde{\rho}_0 d\bar{\rho}/dz$ is buoyancy frequency. Here $\tilde{g}$ is the gravitational acceleration constant, $\tilde{\rho}_0$ is a reference density, and $\bar{\rho}$ is the background density.

Scaling arguments from Spedding et al. [1996a] show that $\mathrm{F} \geq 3$ for initial active turbulence (turbulence with the ability to overturn) to occur. Chomaz et al. [1993] demonstrate that the wake behaves initially as a homogeneous fluid for $\mathrm{F} > 4.5$. In the late wake, many researchers have found these initial vortices to increase in horizontal length and decrease in vertical length, forming "pancake eddies" [Bonnier et al., 1998, Flor et al., 1995, Spedding et al., 1996a,b]. In addition, Spedding et al. [1996a,b] have shown the wake width profile to be the same as an unstratified flow, but with peak velocity an order of magnitude larger than unstratified flow.

It has been noted that horizontal planes in the wake are similar to monopole or dipole formation [Riley and Lelong, 2000]. While many studies on the evolution of dipoles have been carried out [Garten et al., 1998, Praud and Fincham, 2003, Spedding, 2002], an interesting study is that of Billant and Chomaz [2000b]. They show that vertical columnar dipoles undergo a "zig-zag" instability, causing the dipoles to be divided into separate pancake vortex layers. They note this instability to occur between $0.13 < \mathrm{F}_{h0} < 0.21$, with $\mathrm{F}_{h0} = \widetilde{U}_0/(\widetilde{\mathrm{N}}\widetilde{R})$ based on the initial dipole traveling velocity and radius.

1.2.2 Mixing Efficiency

Mixing is a small scale process affecting the thermodynamic makeup of a fluid. It is irreversible, as the fluid can not be returned to its original, pre- mixed state. Mixing is important in geophysical flows as it relates directly to the dynamics of heat, chemicals, and pollutants in the atmosphere and ocean. Mixing is often quantified by an "efficiency", or a relation between the rate of conversion of available potential energy to background potential energy (each defined below) to the rate of lost to viscous dissipation. There are differing definitions of mixing efficiency in the literature which will be examined in the following paragraphs. Prior to defining mixing efficiency, the concepts of available and unavailable potential energy are discussed.

Discussion of potential energy in geophysical settings usually involves the concepts of available and background potential energy, first suggested by Lorenz [1955]. He noted that in order to convert the total potential energy in the Earth's atmosphere to kinetic energy the temperature needed to reach absolute zero, and all mass would be located at sea level ($\tilde{z} = 0$); conditions that cannot readily occur. (It is estimated that potential energy makes up 25% of the total energy (internal + potential + kinetic) in the Earth's atmosphere, while only 2% is kinetic energy [Gill, 1982, pg.81]). Instead, the potential energy $\widetilde{E}_p$ that is available for conversion to kinetic energy is said to be the result of any deviation from a background (or rest) potential energy, $\widetilde{E}_b$. $\widetilde{E}_b$ is a state that would exist if the fluid were adiabatically redistributed (i.e., no heat transfer) to a minimum energy state. The available potential energy is the total potential energy, $\widetilde{\mathcal{P}}$, minus the background potential energy:

$$\widetilde{E}_p = \widetilde{\mathcal{P}} - \widetilde{E}_b \,.$$

Here $\widetilde{\mathcal{P}}$ is defined as $\tilde{\rho}(\tilde{z})\tilde{g}\tilde{z}$, and where $\tilde{\rho}(\tilde{z})$ is density as a function of vertical position $\tilde{z}$ and $\tilde{g}$ is the gravitational acceleration. Due to fluid motions, at a given instant $\tilde{\rho}(\tilde{z})$ may not be in its lowest energy state. $\widetilde{E}_b$ is the minimal potential energy attainable through the adiabatic redistribution of $\tilde{\rho}$ [Thorpe, 1977, Winters et al., 1995] (further discussion on the computation of $\widetilde{E}_b$ is found in §4.2.2), and any change to $\widetilde{E}_b$ is deemed mixing. Similar explanations for $\widetilde{E}_b$ and $\widetilde{E}_a$ can be found in Staquet [2000] and Peltier and Caulfield [2003].

There are two definitions of mixing efficiency in the literature. One definition of mixing efficiency is the ratio of energy lost to background potential energy to the rate of kinetic energy dissipation lost to internal energy [e.g Winters et al., 1995]:

$$\Gamma_a = \frac{\widetilde{\chi}}{\widetilde{\epsilon}}\,, \tag{1.4}$$

where $\widetilde{\chi}$ is the irreversible rate of potential energy dissipation to background or unavailable potential energy. A second definition of mixing efficiency is the proportion of kinetic energy lost by the fluid that leads to mixing, leading to the relation [e.g., Peltier and Caulfield,

2003]:

$$\Gamma_b = \frac{\widetilde{\chi}}{\widetilde{\chi} + \widetilde{\epsilon}}. \tag{1.5}$$

Both Γ_a and Γ_b are easily computed in numerical simulations. However, in field experiments, $\widetilde{\chi}$ and $\widetilde{\epsilon}$ are difficult to make at the same time due to time requirements for measuring each quantity [Gargett and Moum, 1995]. It would be beneficial to measure one quantity (usually ϵ) and relate it to the other. This is done through the flux Richardson number R_f, defined as either the fraction of shear turbulent kinetic energy spent increasing potential energy [Smyth et al., 1996] or the ratio of loss of kinetic energy to buoyancy flux to that produces by shear [Gargett and Moum, 1995]. Both definitions lead to the relation:

$$\mathrm{R_f} = \frac{\widetilde{B}}{\widetilde{B} + \widetilde{\epsilon}}, \tag{1.6}$$

where $\widetilde{B} = -(\tilde{g}/\tilde{\rho}_0)\tilde{\rho}'\tilde{w}'$ is the turbulent buoyancy flux, and primes indicate fluctuating component (with $\tilde{w}'$ vertical fluctuating velocity). In its current form, (1.6) does not relate to mixing, just the fraction of the loss of kinetic energy put into potential energy. To relate this to mixing, density is assumed to be linear in temperature, and the buoyancy flux can be written in terms of $\widetilde{\chi}$:

$$\widetilde{B} = -\frac{1}{2}\widetilde{\chi}\left(\frac{\partial \widetilde{T}}{\partial \tilde{z}}\right)^2 \frac{\partial \tilde{\rho}}{\partial \tilde{z}}.$$

This allows $\mathrm{R_f}$ to be related to mixing by means of a dissipation flux coefficient:

$$\Gamma_d = \frac{\mathrm{R_f}}{1 - \mathrm{R_f}} \tag{1.7}$$

and mass diffusivity parameter [Osborn, 1980]:

$$\tilde{\kappa}_\rho = \Gamma_d \frac{\widetilde{\epsilon}}{\widetilde{\mathrm{N}}^2} \tag{1.8}$$

In oceanic applications, Γ_d is often considered a constant with value 0.2 as suggested by Osborn [1980]. This value is then used to compute $\widetilde{\chi}$ based on measures of $\widetilde{\epsilon}$ [Smyth et al., 1996]. However, measurements of heat flux and $\widetilde{\epsilon}$ have shown Γ_d to vary between 0.1 to 0.4 in the open ocean [Moum, 1990] to 0.7 in turbulent tidal front [Gargett and Moum, 1995].

1.2.3 Fossil Turbulence

The topic of fossil turbulence is championed by Gibson [1980], although he states the concept has been developed by others as early as 1969. Fossil turbulence is defined as "the remnant fluctuation in any hydrophysical field produced by active turbulence which persists after the fluid is no longer actively turbulent (overturning) on the scale of the fluctuation" [Gibson, 1980, 1987]. Gibson's hypothesis is that the vast majority of the ocean is fossilized turbulence with very few patches of active turbulence.

The concept of fossilization is as follows: an "actively turbulent" patch is formed by some instability. In an actively turbulent patch, inertial forces are greater than buoyancy forces, and vertical overturning will occur. The onset of fossilization occurs when the inertial forces of the largest scales become equal to the buoyancy forces. In this state, the vertical length scale of the patch, $\tilde{L}_P$, becomes equal to the overturning scale $\tilde{L}_o$ (see (2.53)). These large

scales are now considered fossilized since they can not overturn. As energy is dissipated (via $\widetilde{\epsilon}$), the inertial force of the large scales diminishes. Then, without energy input, buoyancy, inertial, and viscous forces will all be equal. At this state, assuming isotropy, a transition kinetic energy dissipate rate is defined as $\widetilde{\epsilon}_{tr} = 25\tilde{\nu}\widetilde{\mathrm{N}}^2$.

Once fossilized, the patch is now in a state of microstructure events. The fossilized patch then exhibits "secondary turbulence events," presumably due to instabilities within the original turbulent patch. These secondary turbulence events entrap additional fluid into the fossilized patch. The size of the patch will expand, and then fossilize by the pathway described above. These secondary events are used to explain large regions of microstructure activity measured in the ocean.

The concept of fossilization is not widely agreed upon. Gregg [1987] cites calculations of time constants that suggest the maximum possible age of the microstructure is well below that required for fossilization. Also, Gregg points to assumptions made by Gibson, namely that $\widetilde{\epsilon}$ (and mixing) are maximum at turbulence collapse, while measurements suggest significant mixing after turbulent collapse.

1.2.4 Mixing in Ocean Boundaries

Vertical mixing in the ocean is important to the transport of heat and salt as well as supplying nutrients from bottom water to the surface for support of biological life. Vertical mixing is often related to an "eddy diffusivity," which is the value used to describe the mixing caused by eddy motion. In the open ocean, measured values of vertical eddy diffusivity are approximately 10-20% of what is required for vertical mixing to occur, suggesting that very little vertical mixing occurs in the open ocean [Slinn and Riley, 1996]. Instead, this results suggests that the majority of mixing in the ocean occurs at the ocean boundaries (e.g., near continental slopes, islands, and other topological features). One method of significant mixing in the oceanic boundaries is believed to be due to internal wave reflection from sloping terrain [Eriksen, 1985, 1998, Slinn and Riley, 1996, 1998]. The process arises when an oncoming internal wave, traveling at some angle θ to the horizontal, reflects from a sloping terrain α that is nearly equal to θ. In this case, linear theory predicts the smaller amplitude wave is reflected with larger amplitude, which can breakdown causing mixing to occur. This process is illustrated in figure 1.1.

Eriksen [1982] has made observations of internal wave fields near sloping topography, noting the likely role of internal wave induced mixing in boundary layers of approximately 100m. The amplitudes of reflected waves have been observed to be much less than linear theory prediction, which is attributed to frictional dissipation near the boundary. Laboratory experiments by Cacchione and Southard [1974] and Cacchione and Wunsch [1974] demonstrate that amplification of reflecting internal waves are in agreement with linear theory for cases away from the critical angle. When the angle of reflection is near the critical angle, the amplitude is much less than predicted. Ivey and Nokes [1989] and Taylor [1993] have found that for critical angle reflection the boundary layer turbulence is either steady or unsteady depending on the slope.

1.2.5 Double Diffusion

The density of the ocean is generally determined by two scalar parameters, temperature and salinity, with molecular diffusivities two orders of magnitude different (e.g., typical temperature and salinity Schmidt numbers for seawater are taken to be $\mathrm{Sc_T} \equiv (\tilde{\nu}/\widetilde{D}_T)$

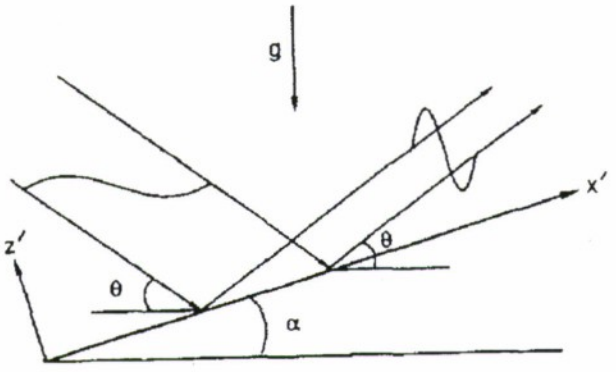

Figure 1.1: Diagram of internal gravity waves reflecting from sloping terrain. As α reaches a critical angle, the wave reflection has a larger amplitude than the incident wave, which leads to instability and wave breakdown. (Taken from Slinn and Riley [1996], Fig. 1)

$= 7$ and $\mathrm{Sc_S} \equiv (\tilde{\nu}/\widetilde{D}_T) = 700$. This indicates that salt diffuses much more slowly than temperature). Also, the contribution of temperature to density is the opposite of salt. That is, when a fluid increases in temperature, its density *decreases*, whereas when salt concentration increases the fluid density *increases*. This combination of large diffusivity difference and opposite contributions to density can lead to a double-diffusion instability [Gargett, 2003]. The classic example is an area of high temperature, high salinity fluid over an area of low temperature, low salinity fluid [Ruddick and Gargett, 2003, Schmitt, 1994]. This scenario is common in the subtropical oceans where warm surface water evaporates, increasing the salinity level at the surface. Since the region is top-heavy in salt, a fluid parcel from the top will flow downward. As the parcel convects downward it will exchange heat, but negligible salt, with the surroundings due to the large difference in diffusivities. Thus, the parcel remains denser than its surroundings and will continue to accelerate downward. Conversely, a fluid parcel gaining heat will become less dense and convect upward. This process leads to the formation of thin "fingers" of salt transport seen in shadowgraphs [Stern, 1960]. Such salt fingers can be found in the ocean at the interface of layers in a thermohaline staircase.

Thermohaline Staircase

A thermohaline staircase is a series of uniform temperature and salinity of layers, separated by thin layers or "sheets" of high temperature and salinity gradients. They are associated with double-diffusive instabilities since similar staircases have been found in laboratory experiments [Kelley, 1987, Stern, 1969, Turner, 1973]. Thermohaline staircases have been documented in nature at several locations, including the Tyrrhenian [Molcard and Tait, 1977] and Mediterranean Seas [Schmitt, 2003], the outflow of the Mediterranean sea into the Atlantic [Elliot and Tait, 1977, Williams, 1974] and in the subtropical Atlantic Ocean [Boyd, 1989, Lambert and Sturges, 1977, Schmitt et al., 1987]. Data from the subtropical Atlantic Ocean from 1960's to 1990's suggest that the staircases are permanent features of the waters where they are located [Schmitt, 2003].

The Caribbean-Sheets and Layers Transects (C-SALT) program was undertaken in 1985 to examine staircase formation and microstructure in the tropical North Atlantic off the

coast of Barbados. Over an area of nearly 1 million km^2, approximately 10 layers of uniform temperature and salinity are generally observed between the depths of 200-800m, each layer ranging from 5-40m in depth. The interface between layers is approximately 1-10m deep in which very large temperature and salinity gradients exist [Schmitt et al., 1987]. The temperature difference in the interfaces between layers ranges between $0.5 - 0.8$°C, and salinity change across the interface is typically 0.1-0.2 psu (practical salinity units). It is noted that these differences are much larger than those reported from the Tyrrhenian (0.1°C and 0.03 psu) and Mediterranean (0.2°C and 0.03 psu) seas.

Microstructure measurements within the C-SALT layer interfaces show several "subinterface" high gradient zones 1-10 cm thick [Gregg and Sanford, 1987, Marmorino, 1987, Schmitt et al., 1987]. Salt fingering occurs in these subinterfaces, and is believed to be the dominant mechanism of mixing and overturning of the thicker layers due to the high levels of mixing vs. the small amount of turbulence measured in these regions [Gregg, 1989]. The enhanced mixing provided by salt-fingering has implications ranging from weather prediction to nutrient replenishment.

The strength of a double-diffusive interface is given by the density ratio R_ρ:

$$R_\rho = \frac{\widetilde{\alpha}\widetilde{T}_z}{\widetilde{\beta}\widetilde{S}_z} \tag{1.9}$$

where $\widetilde{T}_z$, $\widetilde{S}_z$ are the vertical temperature and salt gradients, $\widetilde{\alpha}$ is the thermal expansion coefficient defined in (1.3), and $\widetilde{\beta}$ is the haline contraction coefficient:

$$\widetilde{\beta} = \frac{1}{\tilde{\rho}} \frac{\partial \tilde{\rho}}{\partial \widetilde{S}}\bigg|_{T,p}.$$

Favorable conditions for salt fingering occur when

$$1 < R_\rho < \frac{\tilde{\kappa}_T}{\tilde{\kappa}_S} \approx 100$$

where $\tilde{\kappa}_T$, $\tilde{\kappa}_S$ are the molecular heat and salt diffusivities. It is noted that while this range seems large, the growth rate of salt fingers does not become significant until $R_\rho < 2.0$, with theoretical maximum growth rate at $R_\rho \approx 1.6$. Thus, while most of the ocean is favorable to salt fingering in the sense that $R_\rho > 1.0$, regions with $1.0 < R_\rho < 1.6$ are more likely to show staircase profiles [Schmitt, 1981, 1988].

Differential Diffusion

Double diffusion is a potential energy effect. Differential diffusion is a kinetic energy effect. The underlying cause is same, that salt diffuses about 100 times slower than temperature. However, in the presence of turbulence, the two are often assumed to mix at the same rate (hence have the same eddy diffusivities). This assumption is based in the limit of infinite Reynolds number. However, much of the ocean is mixed by patches of finite Reynolds, finite duration turbulence [Moum, 1996, Smyth et al., 2005]. In these areas of finite Reynolds number, it is certainly plausible that mixing of temperature and salt occurs at different rates due to the large difference in diffusivities between the two. This difference in mixing by turbulence is referred to as differential diffusion and has implication in vertical diffusion of nutrients across the thermocline as well as the accuracy of current mixing models.

Turner [1968] is first credited with demonstrating differential diffusion by mixing a fluid stratified by either temperature or salt (independently) via oscillating grid turbulence and measuring very different turbulent diffusivities. Altman and Gargett [1990] found similar results when varying both temperature and salinity simultaneously. Jackson and Rehmann [2003] found that the ratio of salinity to thermal turbulent diffusivities $\widetilde{K}_S/\widetilde{K}_T$ is between 0.5 and 1 for buoyancy Reynolds number $50 < \mathrm{Re_b} < 500$, values observed in the ocean.

Numerically, the issue of differential diffusion is difficult to examine because of the range of scales required to be resolved [Gargett et al., 2003]. For instance, in a stratified flow the largest scale (smallest wavenumber) that needs to be resolved is the Ozmidov scale $\tilde{L}_o$. The small scales are dependent on the scalar diffusivities, with the wavenumber to be resolved determined by the Batchelor wavenumber

$$\tilde{k}_B = \left(\frac{\widetilde{\epsilon}}{\tilde{\nu}\tilde{\kappa}_\theta^2}\right)^{\frac{1}{4}} = Sc_\theta^{\frac{1}{2}}\tilde{k}_v$$

where $\tilde{k}_v = (\widetilde{\epsilon}/\tilde{\nu}^3)^{1/4}$ is the Kolmogorov wavenumber. For seawater, to model the diffusion of temperature would require $\mathrm{Sc_T}^{1/2} = 7^{1/2} \approx 2.6$ times the resolution than if the Schmidt number was taken as 1. The increase in resolution required for salinity is 26 times ($\mathrm{Sc_S}^{1/2} = 700^{1/2} \approx 26$). This can be a serious limitation in numerical simulations, particularly direct numerical simulations. As a result, tradeoffs must be made between Reynolds number and Schmidt number depending on the available computing resources (this is the case for all flows, not specific to differential diffusion). Gargett et al. [2003], using numerical simulations with a ratio of $\tilde{\kappa}_T/\tilde{\kappa}_S = 0.1$ (rather than 0.01) and maximum $\mathrm{Re} = \widetilde{U}_0\tilde{L}_0/\mathrm{Sc_T} = 99$, show turbulent diffusivity of temperature to be greater than salinity by up to 22%. Smyth et al. [2005] demonstrate differential diffusion in simulations of mixing in breaking Kelvin-Helmholtz billows, utilizing a ratio $\tilde{\kappa}_T/\tilde{\kappa}_S = 0.14$. They note that the turbulent diffusivity is dependent on $\mathrm{Re_b}$, and the ratio of turbulent diffusivities becomes 1 when $\mathrm{Re_b} \approx \mathcal{O}(10^2)$.

Chapter 2

Theoretical Considerations

2.1 Equations of Motion

Fluid flow is described by equations of motion for mass, momentum, and internal energy and an equation of state for the fluid. These equations have the general form:

$$\frac{\partial \tilde{\rho}}{\partial \tilde{t}} + \widetilde{\nabla} \cdot (\tilde{\rho}\tilde{\mathbf{v}}) = 0 \tag{2.1a}$$

$$\frac{\partial \tilde{\rho}\tilde{\mathbf{v}}}{\partial \tilde{t}} + \widetilde{\nabla} \cdot (\tilde{\rho}\tilde{\mathbf{v}}\tilde{\mathbf{v}}) + 2\widetilde{\Omega} \times (\tilde{\rho}\tilde{\mathbf{v}}) = \widetilde{\nabla} \cdot \widetilde{\mathbf{\Pi}} + \tilde{\rho}\widetilde{\mathbf{A}} \tag{2.1b}$$

$$\frac{\partial \tilde{\rho}\tilde{e}}{\partial \tilde{t}} + \widetilde{\nabla} \cdot (\tilde{\rho}\tilde{\mathbf{v}}\tilde{e}) = \widetilde{\nabla} \cdot (\widetilde{\mathbf{\Pi}} \cdot \tilde{\mathbf{v}}) - \widetilde{\nabla} \cdot \tilde{\mathbf{q}} + \tilde{\rho}\tilde{\mathbf{v}} \cdot \widetilde{\mathbf{A}} \tag{2.1c}$$

$$\tilde{\rho} = \tilde{\rho}(C_1, C_2, C_3 \dots), \tag{2.1d}$$

where $\tilde{\rho}$ is the density of the fluid, $\tilde{\mathbf{v}} = (\tilde{u}_1, \tilde{u}_2, \tilde{u}_3)$ is the velocity vector, $\widetilde{\Omega} = (0, \tilde{\Omega}\cos(\phi), \tilde{\Omega}\sin(\phi))$ is the inertial frame rotation rate, $\widetilde{\mathbf{\Pi}}$ is the total stress tensor, $\widetilde{\mathbf{A}}$ is an external acceleration applied to the fluid, $\tilde{e} = \widetilde{E} + \frac{1}{2}\tilde{u}_i^2$ is the sum of internal energy $\widetilde{U}$ and mechanical energy, $\tilde{\mathbf{q}}$ is the heat flux, and $\tilde{p}$ is the thermodynamic pressure. Equation (2.1b), with the Coriolis term $2\widetilde{\Omega} \times (\tilde{\rho}\tilde{\mathbf{v}})$ present, is written with a rotating frame of reference, as is often the case when studying geophysical flows. Equation (2.1d) is an equation of state related to the nature of the fluid. C_x refers to quantities that determine the state of the density. For example, in air C_1, C_2, C_3 might represent pressure, temperature, and humidity, while in sea water the $C's$ might represent pressure, temperature, and salinity. In their present form, equations (2.1) are a set of coupled equations that completely describe the fluid motion. However, solutions to equations (2.1) are nearly impossible to obtain, and certain assumptions must be made to simplify the equations. Such assumptions include assuming a Newtonian fluid, incompressibility, and the Boussinesq assumption, each of which is explained below.

2.1.1 Newtonian Fluid

In order to use equations (2.1), something must be known or assumed about the molecular forces that describe the total stress tensor $\widetilde{\mathbf{\Pi}}$. Under most circumstances, especially in geophysical flows, the fluid is assumed to obey Newton's law of viscosity, originally described by Newton in 1687. Newton's law of viscosity includes two assumptions:

1. $\widetilde{\mathbf{\Pi}}$ is a linear function of velocity gradients and thermodynamic state $\widetilde{\mathbf{\Pi}}(\tilde{\rho}, \tilde{e}, \widetilde{\nabla}\tilde{\mathbf{v}})$.

2. $\widetilde{\mathbf{\Pi}}$ is symmetric.

The first assumption is made because it is desirable to have $\widetilde{\mathbf{\Pi}}$ invariant under Galilean transformation (i.e., $\widetilde{\mathbf{\Pi}}$ is the same in different inertial coordinate systems). Velocity gradients are invariant under Galilean transformation, while the velocity vector itself $\tilde{\mathbf{v}}$ is not Galilean invariant. The second assumption comes about by assuming that the fluid surface cannot support a moment, which forces $\widetilde{\mathbf{\Pi}}$ to be symmetric.

To begin describing $\widetilde{\mathbf{\Pi}}$ mathematically, utilize the fact that pressure acts normal to the surface of a fluid element. Thus, pressure can only reside on the diagonal of $\widetilde{\mathbf{\Pi}}$, allowing $\widetilde{\mathbf{\Pi}}$ to be written in the form

$$\widetilde{\mathbf{\Pi}} = -\tilde{p}\mathbf{I} + \tilde{\tau} \tag{2.2}$$

where $\mathbf{I}$ is the identity tensor, and $\tilde{\tau}$ is the viscous stress tensor. Pressure is negative because in this case because it acts as a compressive stress. Since $\widetilde{\mathbf{\Pi}}$ has been assumed to be symmetric, and pressure is a normal force acting normal to the fluid surface acting only in the diagonal terms, it follows that $\tilde{\tau}$ must be symmetric. Also, from early observations it is assumed that shear stresses in the fluid are linearly related to velocity gradients. Utilizing this information, a constitutive equation for $\tilde{\tau}$ can be formed [Panton, 1996, p.130]:

$$\tilde{\tau} = 2\tilde{\mu}\widetilde{\mathbf{E}} + \tilde{\lambda}(\widetilde{\nabla} \cdot \tilde{\mathbf{v}})\mathbf{I} \tag{2.3}$$

where $\tilde{\mu}$ and $\tilde{\lambda}$ are the first and second coefficients of viscosity respectively, and $\widetilde{\mathbf{E}}$ is the symmetric velocity gradient tensor

$$\widetilde{\mathbf{E}} = \frac{1}{2}\left(\widetilde{\nabla}\tilde{\mathbf{v}} + (\widetilde{\nabla}\tilde{\mathbf{v}})^T\right), \tag{2.4}$$

with superscript T indicating transpose. Equation (2.3) is referred to as the Newtonian constitutive model. Substituting (2.3) into (2.2) yields the total stress tensor for a Newtonian fluid

$$\widetilde{\mathbf{\Pi}} = -\tilde{p}\mathbf{I} + 2\tilde{\mu}\widetilde{\mathbf{E}} + \tilde{\lambda}(\widetilde{\nabla} \cdot \tilde{\mathbf{v}})\mathbf{I}\,. \tag{2.5}$$

Often (2.5) is simplified simplified by using Stokes' hypothesis, which states that thermodynamic and mechanical pressure are equal. This leads to Stokes's assumption of $\tilde{\lambda} = -\frac{2}{3}\tilde{\mu}$.

Now consider the body force $\tilde{\rho}\widetilde{\mathbf{A}}$ and heat flux $\tilde{\mathbf{q}}$ within the flow. For density stratified flows, typically the only body force assumed to act on the flow it that due to gravity (i.e., centripetal acceleration $\widetilde{\mathbf{\Omega}} \times \widetilde{\mathbf{\Omega}} \times \tilde{r}$ is negleged), yielding:

$$\tilde{\rho}\widetilde{\mathbf{A}} = \tilde{\rho}\tilde{\mathbf{g}}\,, \tag{2.6}$$

while heat flux is assumed to obey Fourier's heat conduction law:

$$\tilde{\mathbf{q}} = -\tilde{k}\widetilde{\nabla}\widetilde{T} \tag{2.7}$$

where $\tilde{\mathbf{g}}$ is gravitational acceleration (pointing downward), $\tilde{k}$ is thermal conductivity, and $\widetilde{T}$ is temperature. Substitution of (2.5), (2.6) (2.7) into (2.1) yields the Newtonian equations of motion for stratified flows

$$\frac{\partial\tilde{\rho}}{\partial\tilde{t}} + \widetilde{\nabla} \cdot (\tilde{\rho}\tilde{\mathbf{v}}) = 0 \tag{2.8a}$$

$$\frac{\partial\tilde{\rho}\tilde{\mathbf{v}}}{\partial\tilde{t}} + \widetilde{\nabla} \cdot (\tilde{\rho}\tilde{\mathbf{v}}\tilde{\mathbf{v}}) + 2\widetilde{\mathbf{\Omega}} \times (\tilde{\rho}\tilde{\mathbf{v}}) = -\widetilde{\nabla}\tilde{p} + 2\nabla \cdot (\tilde{\mu}\widetilde{\mathbf{E}}) + \nabla(\tilde{\lambda}\widetilde{\nabla} \cdot \tilde{\mathbf{v}}) + \tilde{\rho}\tilde{\mathbf{g}} \tag{2.8b}$$

$$\frac{\partial \tilde{\rho}\tilde{e}}{\partial \tilde{t}} + \widetilde{\nabla} \cdot (\tilde{\rho}\tilde{\mathbf{v}}\tilde{e}) = -(\widetilde{\nabla} \cdot \tilde{p}\tilde{\mathbf{v}}) + \widetilde{\nabla} \cdot (\tilde{\tau} \cdot \tilde{\mathbf{v}}) + \widetilde{\nabla} \cdot (\tilde{k}\nabla\widetilde{T}) + \tilde{\rho}(\tilde{\mathbf{v}} \cdot \tilde{\mathbf{g}}) \tag{2.8c}$$

$$\tilde{\rho} = \tilde{\rho}(C_1, C_2, C_3 \ldots) \tag{2.8d}$$

where the internal energy equation is left in terms of the viscous stress tensor. Equations (2.8), while telling us something about the kinematic relationship between shear and velocity gradients, are still as set of coupled equations for $\tilde{\rho}$, $\tilde{\mathbf{v}}$, $\widetilde{U}$. A limited number of exact solutions exist, and further simplification is required to obtain more general solutions. The next section addresses transforming (2.8c) to an internal energy equation in terms of temperature.

2.1.2 Internal Energy

The total energy equation (2.8c) is separated into kinetic and internal energy parts. The kinetic energy equation is obtained by taking the dot product of (2.8b) with $\tilde{\mathbf{v}}$,

$$\frac{1}{2}\frac{\widetilde{D}(\tilde{\rho}\tilde{\mathbf{v}}^2)}{\widetilde{D}\tilde{t}} = -\tilde{\mathbf{v}} \cdot \widetilde{\nabla}\tilde{p} + \tilde{\mathbf{v}} \cdot (\widetilde{\nabla} \cdot \tilde{\tau}) + \tilde{\rho}(\tilde{\mathbf{v}} \cdot \tilde{\mathbf{g}}) \tag{2.9}$$

where $\frac{\widetilde{D}}{\widetilde{D}\tilde{t}} = \frac{\partial}{\partial \tilde{t}} + \tilde{\mathbf{v}} \cdot \widetilde{\nabla}$ is the material derivative, and the viscous stress tensor has not been expanded (it will be shown later on that the viscous term can be neglected). Note the loss of the Coriolis term. This is because the quantity $2\widetilde{\boldsymbol{\Omega}} \times (\tilde{\rho}\tilde{\mathbf{v}})$ is $\perp \tilde{\mathbf{v}}$, hence $\tilde{\mathbf{v}} \cdot [2\widetilde{\boldsymbol{\Omega}} \times (\tilde{\rho}\tilde{\mathbf{v}})]$ is zero. Subtracting (2.9) from (2.8c) gives the internal energy equation

$$\frac{\widetilde{D}(\tilde{\rho}\widetilde{U})}{\widetilde{D}\tilde{t}} = -\tilde{p}\widetilde{\nabla} \cdot \tilde{\mathbf{v}} + \tilde{\tau} : \widetilde{\nabla}\tilde{\mathbf{v}} + \widetilde{\nabla} \cdot (\tilde{k}\widetilde{\nabla}\widetilde{T}) \tag{2.10}$$

where the viscous terms have been left as $\tilde{\tau} : \widetilde{\nabla}\tilde{\mathbf{v}}$ for now.

Since temperature can be measured directly, it is desirable to have an equation for temperature $\widetilde{T}$ instead of $\widetilde{U}$. To do this, first redefine (2.10) in terms of enthalpy $\widetilde{H} = \widetilde{U} + (\tilde{p}/\tilde{\rho})$ [Bird et al., 2002, p. 337]:

$$\rho\frac{\widetilde{D}\widetilde{H}}{\widetilde{D}\tilde{t}} = \tilde{\tau} : \widetilde{\nabla}\tilde{\mathbf{v}} + \widetilde{\nabla} \cdot (\tilde{k}\widetilde{\nabla}\widetilde{T}) + \frac{\widetilde{D}\tilde{p}}{\widetilde{D}\tilde{t}}. \tag{2.11}$$

Assuming $\widetilde{H}$ is a function of $\tilde{p}$ and $\widetilde{T}$ only (as is the case for a Newtonian fluid), thermodynamic equilibrium of $\widetilde{H}$ reveals [Panton, 1996, p. 27]

$$\begin{aligned} d\widetilde{H} &= \left(\frac{\partial \widetilde{H}}{\partial \widetilde{T}}\right)_{\tilde{p}} d\widetilde{T} + \left(\frac{\partial \widetilde{H}}{\partial \tilde{p}}\right)_{\widetilde{T}} d\tilde{p} \\ &= \widetilde{C}_p d\widetilde{T} + \frac{1}{\tilde{\rho}^2}\left[\tilde{\rho} - \widetilde{T}\frac{\partial \tilde{\rho}}{\partial \widetilde{T}}\bigg|_{\tilde{p}}\right] d\tilde{p} \\ &= \widetilde{C}_p d\widetilde{T} + \frac{1}{\tilde{\rho}}\left[1 + \widetilde{T}\widetilde{\beta}\right] d\tilde{p} \end{aligned} \tag{2.12}$$

with the thermal expansion coefficient $\widetilde{\beta}$ defined as

$$\widetilde{\beta}(\tilde{p}, \widetilde{T}) \equiv -\frac{1}{\tilde{\rho}}\frac{\partial \tilde{\rho}}{\partial \widetilde{T}}\bigg|_{\tilde{p}}. \tag{2.13}$$

Multiplying (2.12) by $\tilde{\rho}$, and equating the right hand side of (2.11) to (2.12) yields the differential equation for temperature change:

$$\tilde{\rho}\widetilde{C}_p\frac{\widetilde{D}\widetilde{T}}{\widetilde{D}\tilde{t}} = \tilde{\tau} : \widetilde{\nabla}\tilde{\mathbf{v}} + \widetilde{\nabla}\cdot(\tilde{k}\widetilde{\nabla}\widetilde{T}) + \widetilde{T}\widetilde{\beta}\frac{\widetilde{D}\tilde{p}}{\widetilde{D}\tilde{t}} \tag{2.14}$$

It can be shown through scaling analysis that the viscous term is negligible. Defining velocity scale $\widetilde{\mathcal{U}}$ and length scale $\tilde{L}$, the ratio of the major viscous term to inertial terms:

$$\frac{2\tilde{\mu}\widetilde{\mathbf{E}} : \widetilde{\mathbf{E}}}{\tilde{\rho}\widetilde{C}_p(\widetilde{D}\widetilde{T}/\widetilde{D}\tilde{t})} \sim \frac{\tilde{\mu}\widetilde{\mathcal{U}}^2/\tilde{L}^2}{\tilde{\rho}\widetilde{C}_p\widetilde{\mathcal{U}}\widetilde{T}/\tilde{L}} = \frac{\tilde{\nu}}{\widetilde{C}_p}\frac{\widetilde{\mathcal{U}}}{\widetilde{T}\tilde{L}}\,. \tag{2.15}$$

(2.15) is typically $\mathcal{O}(10^{-7})$ [Kundu and Cohen, 2002, p. 120], allowing the viscous term to be neglected. The equations of motion (2.8) can then be written as

$$\frac{\partial\tilde{\rho}}{\partial\tilde{t}} + \widetilde{\nabla}\cdot(\tilde{\rho}\tilde{\mathbf{v}}) = 0 \tag{2.16a}$$

$$\frac{\partial\tilde{\rho}\tilde{\mathbf{v}}}{\partial\tilde{t}} + \widetilde{\nabla}\cdot(\tilde{\rho}\tilde{\mathbf{v}}\tilde{\mathbf{v}}) + 2\widetilde{\boldsymbol{\Omega}}\times(\tilde{\rho}\tilde{\mathbf{v}}) = -\widetilde{\nabla}\tilde{p} + 2\widetilde{\nabla}\cdot(\tilde{\mu}\widetilde{\mathbf{E}}) + \widetilde{\nabla}(\tilde{\lambda}\widetilde{\nabla}\cdot\tilde{\mathbf{v}}) + \tilde{\rho}\tilde{\mathbf{g}} \tag{2.16b}$$

$$\tilde{\rho}\widetilde{C}_p\frac{\widetilde{D}\widetilde{T}}{\widetilde{D}\tilde{t}} = \widetilde{\nabla}\cdot(\tilde{k}\widetilde{\nabla}\widetilde{T}) + \widetilde{T}\widetilde{\beta}\frac{\widetilde{D}\tilde{p}}{\widetilde{D}\tilde{t}} \tag{2.16c}$$

$$\tilde{\rho} = \tilde{\rho}(\tilde{p}, \widetilde{T}, \widetilde{S})\,. \tag{2.16d}$$

Treating the atmosphere as an ideal gas with equation of state $\tilde{p} = \tilde{\rho}\widetilde{R}\widetilde{T}$, $\widetilde{\beta}$ can be shown to be the reciprocal of temperature

$$\widetilde{\beta} = -\frac{1}{\tilde{\rho}}\frac{\partial\tilde{\rho}}{\partial\widetilde{T}}\bigg|_{\tilde{p}} = -\left(\frac{\widetilde{R}\widetilde{T}}{\tilde{p}}\right)\left(\frac{-\tilde{p}}{\widetilde{R}\widetilde{T}^2}\right) = \frac{1}{\widetilde{T}}\,. \tag{2.17}$$

Thus, $\widetilde{\beta}\widetilde{T} = 1$, reducing (2.16c) to:

$$\tilde{\rho}\widetilde{C}_p\frac{\widetilde{D}\widetilde{T}}{\widetilde{D}\tilde{t}} = \widetilde{\nabla}\cdot(\tilde{k}\widetilde{\nabla}\widetilde{T}) + \frac{\widetilde{D}\tilde{p}}{\widetilde{D}\tilde{t}}\,. \tag{2.18}$$

Alternatively, using the relation $\widetilde{C}_p - \widetilde{C}_v = \widetilde{R}$, the equation of state for an ideal gas, and continuity in the form $\frac{\widetilde{D}\tilde{\rho}}{\widetilde{D}\tilde{t}} = -\tilde{\rho}(\widetilde{\nabla}\cdot\tilde{\mathbf{v}})$, (2.18) can be written as [Bird et al., 2002, pg. 337]:

$$\tilde{\rho}\widetilde{C}_v\frac{\widetilde{D}\widetilde{T}}{\widetilde{D}\tilde{t}} = \widetilde{\nabla}\cdot(\tilde{k}\widetilde{\nabla}\widetilde{T}) - \tilde{p}(\widetilde{\nabla}\cdot\tilde{\mathbf{v}})\,. \tag{2.19}$$

2.1.3 Static Stability

A column of fluid is said to be stable when higher density parcels are located below lower density parcels (i.e., density decreases with height). Since density is a function of both temperature and pressure, compressibility effects may become important in determining static stability. For example, consider a fluid element at some height z_1 that is displaced adiabatically (no heat transfer with the environment) to some lower elevation (and higher pressure) z_2. As the fluid element is moved to the higher pressure region it will become

compressed. The pressure has done work on the element, and the element's temperature will increase. This is shown mathematically using the first law of thermodynamics:

$$d\widetilde{E} = d\widetilde{Q} + d\tilde{w} \tag{2.20}$$

where $d\widetilde{E}$ is change in energy, $d\widetilde{Q}$ is change in internal heat, and $d\tilde{w}$ is work.

In order to determine static stability of a column of fluid a conserved quantity must be used. A conserved quantity remains the same when it undergoes an adiabatic process, i.e., a process by which $d\widetilde{Q} = 0$. To see if temperature is conserved, begin by noting that the work done is related to the change in volume:

$$d\tilde{w} = -\tilde{p} \cdot d\tilde{v}\,, \tag{2.21}$$

where $d\tilde{v}$ is the change in specific volume ($\tilde{v} = \frac{1}{\tilde{\rho}}$). Conservation of temperature is examined for the atmosphere, where is air is assumed to obey the ideal gas equation of state (and thus neglecting humidity). The same analysis can be performed for seawater, but with a much more complicated equation of state (see Appendix). For an ideal gas, internal energy is defined as

$$\widetilde{E} = \widetilde{C}_v \widetilde{T}. \tag{2.22}$$

Substituting (2.21) and (2.22) into (2.20) (with $d\widetilde{Q} = 0$) yields:

$$\begin{aligned}
\widetilde{C}_v d\widetilde{T} &= 0 - \tilde{p} \cdot d\tilde{v} \\
\widetilde{C}_v d\widetilde{T} &= -\tilde{p} d\left(\frac{\widetilde{R}\widetilde{T}}{\tilde{p}}\right) \\
\widetilde{C}_v d\widetilde{T} &= -\widetilde{R} d\widetilde{T} + \frac{\widetilde{R}\widetilde{T} d\tilde{p}}{\tilde{p}} \\
\widetilde{C}_p d\widetilde{T} &= \frac{\widetilde{R}\widetilde{T} d\tilde{p}}{\tilde{p}} \\
\frac{d\widetilde{T}}{\widetilde{T}} &= \tilde{\kappa} \frac{d\tilde{p}}{\tilde{p}}
\end{aligned} \tag{2.23}$$

where $\tilde{\kappa} = \widetilde{R}/\widetilde{C}_p$, and the relationship $\widetilde{C}_p = \widetilde{C}_v + \widetilde{R}$ has been utilized. Integrating (2.23) from a reference temperature and pressure (usually taken at sea level) $\widetilde{T}_o$, $\tilde{p}_o$ gives:

$$\frac{\widetilde{T}}{\widetilde{T}_o} = \left(\frac{\tilde{p}}{\tilde{p}_o}\right)^{\tilde{\kappa}}, \tag{2.24}$$

demonstrating that temperature is not conserved when an adiabatic process is applied.

Since temperature is not a conserved quantity, another quantity must be used to determine the stability of the atmosphere. Potential temperature $\widetilde{\Theta}$ is conserved, and is defined as the temperature a fluid particle would be if it were adiabatically compressed (or expanded) from its *in situ* pressure $\tilde{p}$ to the reference pressure $\tilde{p}_o$:

$$\widetilde{\Theta} = \widetilde{T}\left(\frac{\tilde{p}_o}{\tilde{p}}\right)^{\tilde{\kappa}}. \tag{2.25}$$

To see if $\widetilde{\Theta}$ is conserved under an adiabatic process, start by rearranging (2.25) and differentiating:

$$\begin{aligned} \widetilde{T} &= \widetilde{\Theta}\left(\frac{\tilde{p}}{\tilde{p}_o}\right)^{\tilde{\kappa}} \\ d\widetilde{T} &= d\widetilde{\Theta}\left(\frac{\tilde{p}}{\tilde{p}_o}\right)^{\tilde{\kappa}} + \tilde{\kappa}\widetilde{\Theta}\left(\frac{\tilde{p}}{\tilde{p}_o}\right)^{\tilde{\kappa}}\frac{d\tilde{p}}{\tilde{p}}\,. \end{aligned}$$

Substituting these into (2.23) shows that potential temperature is conserved under an adiabatic process:

$$\frac{d\widetilde{\Theta}}{\widetilde{\Theta}} = 0\,. \tag{2.26}$$

Thus, the gradient of potential energy $d\widetilde{\Theta}/d\tilde{z}$ is used to determine the stability of the atmosphere, with positive $d\widetilde{\Theta}/d\tilde{z}$ signifying a stable stratification.

Compressibility effects are important in the ocean, particularly the deep ocean where large hydrostatic pressures exist. Since

2.1.4 Incompressible Flow

The assumption of incompressibility does not necessarily mean constant density flow. Rather, the incompressible flow assumption is that changes in density of a fluid particle are negligible. To see when incompressibility can be applied, first assume that density is a function of pressure and temperature (neglecting salinity and humidity), which yields a general thermodynamic transport equation for density [Panton, 1996, p. 230].

$$\frac{1}{\tilde{\rho}}\frac{\widetilde{D}\tilde{\rho}}{\widetilde{D}\tilde{t}} = \tilde{\alpha}\frac{\widetilde{D}\tilde{p}}{\widetilde{D}\tilde{t}} - \tilde{\beta}\frac{\widetilde{D}\widetilde{T}}{\widetilde{D}\tilde{t}}\,, \tag{2.27}$$

where $\tilde{\alpha}$ is the isothermal compressibility coefficient defined as

$$\tilde{\alpha}(\tilde{p},\widetilde{T}) \equiv \frac{1}{\tilde{\rho}}\frac{\partial\tilde{\rho}}{\partial\tilde{p}}\bigg|_{\widetilde{T}} \tag{2.28}$$

and $\widetilde{\beta}$ is the bulk or thermal expansion coefficient defined in (2.13).

The next step is to nondimensionalize equations (2.27) and (2.16). Denoting $\tilde{L}$, $\widetilde{\mathcal{U}}$, $\tilde{\rho}_o$ as length, velocity, and density scales, the following nondimensional quantities are defined:

$$\begin{aligned} \mathbf{v} &= \frac{\tilde{\mathbf{v}}}{\widetilde{U}} & \mathbf{x} &= \frac{\tilde{\mathbf{x}}}{\tilde{L}} & t &= \frac{\tilde{t}}{\tilde{L}/\widetilde{U}} & \rho &= \frac{\tilde{\rho}}{\tilde{\rho}_o} \\ T &= \frac{\widetilde{T}}{\tilde{\mu}\widetilde{U}^2/\tilde{k}} & C_p &= \frac{\widetilde{C}_p}{\widetilde{C}_{p_o}} & \beta &= \frac{\widetilde{\beta}}{\widetilde{\beta}_o}\,. \end{aligned}$$

Substituting the above scales into (2.27) yields the following nondimensional density transport equation:

$$\frac{1}{\rho}\frac{D\rho}{Dt} = \gamma M^2\left[\alpha\frac{Dp}{Dt} - \frac{\mathrm{PrB}\beta}{\mathrm{A}}\frac{DT}{Dt}\right], \tag{2.29}$$

while substitution of the above scales into (2.16) yields the following nondimensional equations (where equation of state is omitted):

$$\frac{\partial\rho}{\partial t} + \nabla\cdot(\rho\mathbf{v}) = 0 \tag{2.30a}$$

$$\frac{\partial \rho \mathbf{v}}{\partial t} + \nabla \cdot (\rho \mathbf{v}\mathbf{v}) + \frac{1}{\mathrm{Ro}}(\boldsymbol{\Omega} \times \mathbf{v}) = -\nabla p + \frac{1}{\mathrm{Re}}\Big(2\nabla \cdot (\mu \mathbf{E}) + \nabla(\lambda \nabla \cdot \mathbf{v})\Big) + \rho \frac{1}{\mathrm{F}^2} \tag{2.30b}$$

$$\rho C_p \frac{DT}{Dt} = \frac{1}{\mathrm{RePr}} k \nabla^2 T + \beta \mathrm{B}\left[\frac{1}{\mathrm{Pr}} + \frac{\gamma M^2}{\mathrm{A}} T\right] \frac{Dp}{Dt}, . \tag{2.30c}$$

In the above equations, the the following non-dimensional quantities have been obtained:

$$\mathrm{Re} = \frac{\tilde{\rho}\tilde{L}\tilde{U}}{\tilde{\mu}} \qquad \mathrm{Pr} = \frac{\tilde{\mu}\tilde{C}_p}{\tilde{k}} \qquad \gamma = \frac{\tilde{C}_p}{\tilde{C}_v} \qquad \mathrm{Ro} = \frac{\tilde{U}}{\tilde{f}\tilde{L}}$$

$$\mathrm{F}^2 = \frac{\tilde{U}^2}{\tilde{\mathbf{g}}\tilde{L}} \qquad \mathrm{M} = \frac{\tilde{\mathcal{U}}}{\tilde{a}} \qquad \mathrm{A} = \tilde{\alpha}\tilde{\rho}\tilde{C}_p\tilde{T} \qquad \mathrm{B} = \tilde{\beta}\tilde{T}\,.$$

Here $\tilde{f} = 2\tilde{\Omega}\sin(\tilde{\theta})$ is the Coriolis frequency, and a is the speed of sound in the fluid medium, defined as

$$\tilde{a} = \left.\frac{\partial \tilde{\rho}}{\partial \tilde{p}}\right|_{\tilde{S}}.$$

From (2.29), it is evident that for change in density to be small, the square of the Mach number M^2 must be small. Also, if one considers a flow decelerating from some velocity v to 0, the pressure change will be $\Delta p = \frac{1}{2}\rho v$. Substitution into M^2 yields [Panton, 1996, p. 236]

$$\begin{aligned} M^2 &= \frac{\tilde{v}^2}{\tilde{a}^2} = \tilde{v}^2 \left.\frac{\partial \tilde{\rho}}{\partial \tilde{p}}\right|_{\tilde{S}} = \frac{\tilde{\rho}\tilde{v}^2}{\tilde{\rho}} \left.\frac{\partial \tilde{\rho}}{\partial \tilde{p}}\right|_{\tilde{S}} \\ &\approx \Delta\tilde{p}\frac{1}{\tilde{\rho}}\frac{\Delta\tilde{\rho}}{\Delta\tilde{p}} \\ &= \frac{\Delta\tilde{\rho}}{\tilde{\rho}} \end{aligned} \tag{2.31}$$

Hence, M^2 can be seen as the relative change of density of the fluid. For incompressibility (negligible density change), M^2 must be small, and terms containing M^2 can be neglected. In addition, nondimensionalizing thermodynamic properties (e.g., μ, C_p) shows that when the Mach number is small relative changes in these properties are also small, allowing the properties to be considered constant. When a low Mach number is assumed, terms with M^2 can be neglected in (2.29), resulting in the following density transport equation:

$$\frac{\tilde{D}\tilde{\rho}}{\tilde{D}\tilde{t}} = 0\,. \tag{2.32}$$

Substituting (2.33d) into (2.30) and neglecting terms with M^2 yields the following set of (dimensional) equations of motion:

$$\tilde{\nabla} \cdot \tilde{\mathbf{v}} = 0 \tag{2.33a}$$

$$\tilde{\rho}\left(\frac{\partial \tilde{\mathbf{v}}}{\partial \tilde{t}} + \tilde{\mathbf{v}} \cdot \tilde{\nabla}\tilde{\mathbf{v}}\right) + 2\tilde{\rho}(\tilde{\boldsymbol{\Omega}} \times \tilde{\mathbf{v}}) = -\tilde{\nabla}\tilde{p} + \tilde{\mu}\tilde{\nabla}^2\tilde{\mathbf{v}} + \tilde{\rho}\tilde{\mathbf{g}} \tag{2.33b}$$

$$\tilde{\rho}\tilde{C}_v\frac{\tilde{D}\tilde{T}}{\tilde{D}\tilde{t}} = \tilde{k}\tilde{\nabla}^2\tilde{T} \tag{2.33c}$$

$$\tilde{\rho} = \tilde{\rho}(C_1, C_2, C_3 \ldots)\,, \tag{2.33d}$$

where (2.33a) is obtained via substitution of (2.32) into the full continuity equation (2.16a), (2.33b) results from substitution of the simplified continuity equation (2.33a), and (2.33c) is obtained via use of (2.19) and substitution of continuity equation (2.33a). Also, with $\tilde{\mu}$ constant the viscous term simplifies to $\tilde{\mu}\widetilde{\nabla}^2\tilde{\mathbf{v}}$ by substituting of equation 2.4 (in indicial notation):

$$\begin{aligned} 2\tilde{\mu}\widetilde{\nabla}\cdot\widetilde{\mathbf{E}} &= 2\tilde{\mu}\frac{1}{2}\frac{\partial}{\partial\tilde{x}_i}\left(\frac{\partial\tilde{u}_i}{\partial\tilde{x}_j}+\frac{\partial\tilde{u}_j}{\partial\tilde{x}_i}\right) \\ &= \tilde{\mu}\left(\frac{\partial^2\tilde{u}_i}{\partial\tilde{x}_i\partial\tilde{x}_j}+\frac{\partial^2\tilde{u}_j}{\partial\tilde{x}_i\partial\tilde{x}_i}\right) \\ &= \tilde{\mu}\left[\widetilde{\nabla}(\widetilde{\nabla}\cdot\tilde{\mathbf{v}})+\widetilde{\nabla}^2\tilde{\mathbf{v}}\right] \\ &= \tilde{\mu}\widetilde{\nabla}^2\tilde{\mathbf{v}} \end{aligned} \tag{2.34}$$

where $\widetilde{\nabla}(\widetilde{\nabla}\cdot\tilde{\mathbf{v}})$ is zero from continuity.

The set of equations (2.33) are termed the incompressible flow equations and are typically considered valid for M < 0.3. A benefit of assuming incompressible flow (low Mach number) is that the energy equation (2.33c) is decoupled from the mass and momentum equations. This is important, as it allows for solution of four variables (pressure and three components of velocity) with four equations (continuity and three momentum equations) without solving for temperature or internal energy.

2.1.5 Boussinesq Approximation

The Boussinesq approximation is a widely applied approximation to the equations of motion first suggested by Boussinesq [1903]. In words, the Boussinesq approximation involves two assumptions:

1) Density fluctuations within fluid motion are the result of thermal effects only (i.e., no pressure effect, salinity, humidity).

2) Accelerations within the fluid are small compared to acceleration due to gravity. Thus, density fluctuations are unimportant in the flow unless multiplied by gravity.

Following the presentation by Spiegel and Veronis [1960], begin by representing density in the following form

$$\tilde{\rho}_t(x,y,z,t) = \tilde{\rho}_0 + \tilde{\bar{\rho}}(z) + \tilde{\rho}(x,y,z,t) \tag{2.35}$$

where $\tilde{\rho}_0$ is the constant spatial average density, $\tilde{\bar{\rho}}(z)$ is the variation of density in the absence of motion, and $\tilde{\rho}$ is the fluctuation of density resulting from fluid motion. The scale height of density is defined as

$$\widetilde{D}_\rho = \left|\frac{1}{\tilde{\rho}_0}\frac{d\tilde{\bar{\rho}}}{d\tilde{z}}\right|^{-1}. \tag{2.36}$$

In the Boussinesq approximation it is assumed that the fluid motion is limited to a layer of thickness $\tilde{d}$ that is much less than the scale height $\widetilde{D}_\rho$ [Spiegel and Veronis, 1960], i.e.,

$$\frac{\tilde{d}}{\widetilde{D}_\rho} \ll 1. \tag{2.37}$$

Integrating (2.37) from minimum to maximum density within $\tilde{d}$ yields

$$\frac{\Delta\tilde{\bar{\rho}}}{\tilde{\rho}_0} \equiv \epsilon \ll 1 \tag{2.38}$$

where $\Delta\tilde{\bar{\rho}}$ is the maximum density variation in the layer $\tilde{d}$. In addition to (2.38), the motion induced density fluctuations $\tilde{\rho}$ are restricted to not exceed the static variation. i.e.,

$$\left|\frac{\tilde{\rho}}{\tilde{\rho}_0}\right| \leq \mathcal{O}(\epsilon)\,. \tag{2.39}$$

Spiegel and Veronis [1960] note that while (2.39) must be verified after solutions have been obtained, there has been no experimental evidence that $\tilde{\rho}$ ever exceeds $\Delta\tilde{\rho}_v$. Using these criterion, substituting (2.35) into continuity equation yeilds:

$$\begin{aligned}
\widetilde{\nabla}\cdot\tilde{\mathbf{v}} &= -\frac{\widetilde{D}}{\widetilde{D}\tilde{t}}(\tilde{\rho}_0+\tilde{\bar{\rho}}+\tilde{\rho}) \\
&= -\frac{\widetilde{D}}{\widetilde{D}\tilde{t}}\left(1+\frac{\tilde{\bar{\rho}}}{\tilde{\rho}_0}+\frac{\tilde{\rho}}{\tilde{\rho}_0}\right) \\
&= -\frac{\widetilde{D}}{\widetilde{D}\tilde{t}}\left(\epsilon\frac{\tilde{\bar{\rho}}}{\Delta\tilde{\bar{\rho}}}+\epsilon\frac{\tilde{\rho}}{\Delta\tilde{\bar{\rho}}}\right)+\mathcal{O}(\epsilon^2)
\end{aligned} \tag{2.40}$$

To order ϵ, (2.40) can be written as

$$\widetilde{\nabla}\cdot\tilde{\mathbf{v}} = 0 \tag{2.41}$$

which is the same result as assuming incompressible flow.

Now consider the hydrostatic equation of motion. Expressing pressure in the same form as density in (2.35) and substituting into the vertical component of momentum gives the following hydrostatic equation

$$\frac{\partial\tilde{\bar{p}}}{\partial\tilde{z}} = -\tilde{\mathbf{g}}(\tilde{\rho}_0+\tilde{\bar{\rho}}) \tag{2.42}$$

where the fluctuating density $\tilde{\rho}$ is zero since there is no fluid motion. Subtracting (2.42) from the total momentum equation (2.16b) with the full expression of density and pressure gives

$$\frac{\partial\tilde{\rho}\tilde{\mathbf{v}}}{\partial\tilde{t}}+\widetilde{\nabla}\cdot(\tilde{\rho}\tilde{\mathbf{v}}\tilde{\mathbf{v}})+2\tilde{\rho}(\widetilde{\Omega}\times\tilde{\mathbf{v}}) = -\widetilde{\nabla}\tilde{p}+2\widetilde{\nabla}\cdot(\tilde{\mu}\widetilde{\mathbf{E}})+\widetilde{\nabla}(\tilde{\lambda}\widetilde{\nabla}\cdot\tilde{\mathbf{v}})\tilde{\mathbf{g}}\tilde{\rho}\,. \tag{2.43}$$

Using the simplification of (2.41), and dividing by $\tilde{\rho}$, (2.43) can be reduced to

$$\frac{\widetilde{D}\tilde{\mathbf{v}}}{\widetilde{D}\tilde{t}}+2\widetilde{\Omega}\times\tilde{\mathbf{v}} = -\frac{1}{\tilde{\bar{\rho}}}\widetilde{\nabla}\tilde{p}-\tilde{\mathbf{g}}\epsilon\frac{\tilde{\rho}}{\Delta\tilde{\bar{\rho}}}+\tilde{\nu}\widetilde{\nabla}^2\tilde{\mathbf{v}}\,, \tag{2.44}$$

where $\tilde{\mu}$ and $\tilde{\nu}=\tilde{\mu}/\tilde{\rho}$ have been taken to be a constant. Substituting (2.38) for ϵ, the Boussinesq equations of motion can be written in their usual form as:

$$\widetilde{\nabla}\cdot\tilde{\mathbf{v}} = 0 \tag{2.45a}$$

$$\frac{\widetilde{D}\tilde{\mathbf{v}}}{\widetilde{D}\tilde{t}}+2\widetilde{\Omega}\times\tilde{\mathbf{v}} = -\frac{1}{\tilde{\rho}_0}\widetilde{\nabla}\tilde{p}'-\tilde{\mathbf{g}}\frac{\tilde{\rho}'}{\tilde{\rho}_0}+\tilde{\nu}\widetilde{\nabla}^2\tilde{\mathbf{v}} \tag{2.45b}$$

$$\tilde{\rho}\widetilde{C}_v\frac{\widetilde{D}\widetilde{T}}{\widetilde{D}\tilde{t}} = \tilde{k}\widetilde{\nabla}^2\widetilde{T} \tag{2.45c}$$

$$\tilde{\rho} = \tilde{\rho}(C_1, C_2, C_3 \dots) \tag{2.45d}$$

Often it is necessary to have an evolution equation for the density of the fluid. This can be achieved through the internal energy equation 2.45c and the assumption that density fluctuations are not a result of pressure effects (i.e., the first assumption made at the beginning of this section), allowing the pressure dependence in the thermodynamic equation of state for density (2.27) to be eliminated. In addition, since density fluctuations are assumed to be small (cf. (2.38)), a linear relationship between the density and temperature fluctuation can be made. This allows substitution of $D\rho$ for DT in (2.45c), yielding the following Boussinesq equations:

$$\tilde{\nabla} \cdot \tilde{\mathbf{v}} = 0 \tag{2.46a}$$

$$\frac{\tilde{D}\tilde{\mathbf{v}}}{\tilde{D}\tilde{t}} + 2\tilde{\Omega} \times \tilde{\mathbf{v}} = -\frac{1}{\tilde{\rho}_0}\tilde{\nabla}\tilde{p}' - \tilde{\mathbf{g}}\frac{\tilde{\rho}'}{\tilde{\rho}_0} + \tilde{\nu}\tilde{\nabla}^2\tilde{\mathbf{v}} \tag{2.46b}$$

$$\frac{\tilde{D}\tilde{\rho}}{\tilde{D}\tilde{t}} = \tilde{\kappa}\tilde{\nabla}^2\tilde{\rho} \tag{2.46c}$$

where $\tilde{\kappa} = \tilde{k}/(\tilde{\rho}\tilde{C}_v)$ is the mass diffusivity. Equations (2.46) are those commonly solved in numerical experiments. As with the low Mach number approximation, the Boussinesq approximation allows mass and momentum to be decoupled from the energy (now density) equation, providing five variables (pressure, three velocities, density) with five equations (continuity, three momentum, density). However, the assumptions leading to the Boussinesq simplifications should not be overlooked, namely that internal accelerations are small compared to gravity and the fluid motion is in a layer much less than the scale height. If, for example, simulations were to be performed of the entire thermocline, fluid motions may exists in a layer $\tilde{d}$ which is not negligible compared to the thermocline scale height, in which case the Boussinesq approximation will not be valid.

2.1.6 Nondimensional Boussinesq equations

Nondimensionalization of the equations of motion (2.46) can provide insight to the relative importance of each term. In order to nondiminensionalize (2.46), the following nondimensional terms will be used:

$$\begin{aligned} \mathbf{v} &= \frac{\tilde{\mathbf{v}}}{\tilde{\mathcal{U}}} & \mathbf{x} &= \frac{\tilde{\mathbf{x}}}{\tilde{L}} & t &= \frac{\tilde{t}}{\tilde{L}/\tilde{\mathcal{U}}} \\ \rho &= \frac{\tilde{\rho}}{\tilde{L}\left|\frac{\Delta\tilde{\bar{\rho}}}{\Delta\tilde{z}}\right|} & \mathbf{\Omega} &= \frac{\tilde{\mathbf{\Omega}}}{\tilde{f}} & p &= \frac{\tilde{p}}{\tilde{\rho}_o\tilde{U}^2}. \end{aligned} \tag{2.47}$$

In 2.47 above, $\tilde{L}$ is a length scale, $\tilde{\mathcal{U}}$ is a velocity length scale, and $\tilde{f} = 2\tilde{\Omega}\sin(\theta)$ is the Coriolis parameter (where θ is the Earth's latitude). Note that in density stratified flows it is common to nondimensionalize $\tilde{\rho}$ by by the product of the length scale and the scale of the change in density $\Delta\tilde{\bar{\rho}}/\Delta\tilde{z}$. Also note that pressure is nondimensinalized by the dynamic pressure $\tilde{\rho}_0\tilde{\mathcal{U}}^2$. Substituting (2.47) into equations (2.46) yields the following nondimensional Boussinesq equations of motion:

$$\nabla \cdot \mathbf{v} = 0 \tag{2.48a}$$

$$\frac{D\mathbf{v}}{Dt} + \frac{1}{\mathrm{Ro}}(\mathbf{\Omega} \times \mathbf{v}) = -\nabla p - \left(\frac{2\pi}{\mathrm{F}}\right)^2 \rho\mathbf{e}_z + \frac{1}{\mathrm{Re}}\nabla^2\mathbf{v} \tag{2.48b}$$

$$\frac{D\rho}{Dt} = \frac{1}{\mathrm{ScRe}}\nabla^2\rho. \tag{2.48c}$$

The following nondimensional parameters are used to determine the significance of each terms in equatoins (2.48):

$$\mathrm{Ro} = \frac{\widetilde{U}}{\tilde{L}\tilde{f}} \qquad \mathrm{F} = \frac{\widetilde{U}}{\widetilde{\mathrm{N}}\tilde{L}} \qquad \mathrm{Re} = \frac{\widetilde{U}\tilde{L}}{\tilde{\nu}} \qquad \mathrm{Sc} = \frac{\tilde{\nu}}{\tilde{\kappa}}, \tag{2.49}$$

where Ro is the Rossby number, F is the Froude number, Re is the Reynolds number, Sc is the Schmidt number, and $\widetilde{\mathrm{N}}^2 = (\tilde{g}/\bar{\rho})\Delta\tilde{\rho}/\Delta\tilde{z}$ is the Brunt-Väisälä (or buoyancy) frequency. The significance of each nondimensional parameter is briefly described below.

The Rossby number (Ro) describes the ratio of inertial to Coriolis forces. When Ro is large, Coriolis forces due to planetary motion can be neglected. This will occur in low-latitude regions of the Earth (i.e., in the Tropics), when the length scale is small, or when the velocity is very large.

The Froude number (F) describes the ratio of inertia forces to gravity forces. In a stratified fluid, a buoyancy force arises due to the motion of fluid elements with differing density. For instance, a fluid element with a high density traveling upward to a lower density region would experience a buoyancy force trying to push it back to its lower, stable location. Decreasing F signifies increasing stratification strength. Note that buoyancy force can act as a stabilizing force that inhibits vertical motion.

The Reynolds number (Re) describes the ratio of inertia forces to viscous forces. When Re is large, the inertial terms of the equations of motion dominate and viscous terms can be neglected, such as flows far from boundaries or with very large length scale. Conversely, a small Re indicates a viscous dominated flow.

The Schmidt number (Sc) is used to describe the ratio of momentum diffusivity (i.e., viscosity) to mass diffusivity. A large Sc indicates that momentum is diffused faster than mass. Note the Sc ≈ 0.7 for air, while in sea water Sc is approximately 7 for temperature and 700 for salinity. Often numerical simulations are performed with Sc $= 1$, since a higher resolution simultation is required to capture effects of both viscosity and diffusivity when Sc is much different than 1.

2.1.7 Low Froude Number Equations

In density stratified flow, the buoyancy force of the stratification acts to suppress (positive) vertical motions. This leads one to believe that the horizontal and vertical scales will be different. As such, it is common in the literature to find equations (2.46) and (2.48) divided into horizontal and vertical components [Billant and Chomaz, 2000a, Gargett, 1988, Lilly, 1983, Riley and Lelong, 2000, Riley et al., 1981, e.g]. They are usually written as:

$$\widetilde{\nabla}_H \cdot \tilde{\mathbf{v}}_H + \frac{\partial\tilde{w}}{\partial\tilde{z}} = 0 \tag{2.50a}$$

$$\frac{\partial\tilde{\mathbf{v}}_H}{\partial\tilde{t}} + \tilde{\mathbf{v}}_H \cdot \widetilde{\nabla}\tilde{\mathbf{v}}_H + \tilde{w}\frac{\tilde{\mathbf{v}}_H}{\partial\tilde{z}} + \widetilde{\Omega} \times \tilde{\mathbf{v}}_H = -\widetilde{\nabla}_H\tilde{p} + \widetilde{\nabla}^2\tilde{\mathbf{v}}_H \tag{2.50b}$$

$$\frac{\partial\tilde{w}}{\partial\tilde{t}} + \tilde{\mathbf{v}}_H \cdot \widetilde{\nabla}\tilde{w} + \tilde{w}\frac{\partial\tilde{w}}{\partial\tilde{z}} = -\frac{\partial\tilde{p}}{\partial\tilde{z}} - \tilde{\rho}\tilde{g} + \widetilde{\nabla}^2\tilde{w} \tag{2.50c}$$

$$\frac{\partial\tilde{\rho}}{\partial\tilde{t}} + \tilde{\mathbf{v}}_H \cdot \widetilde{\nabla}\tilde{\rho} + \tilde{w}\frac{\partial\tilde{\rho}}{\partial\tilde{z}} - \tilde{w} = \widetilde{\nabla}^2\tilde{\rho} \tag{2.50d}$$

where subscript H indicates horizontal (e.g., $\tilde{\mathbf{v}}_H = (\tilde{u}, \tilde{v})$), $\tilde{w}$ is vertical velocity, all other term are as defined above.

Nondimensionalization of the equations of motion provides insight to the relative importance of each term. Nondimensional versions of equations (2.50) are presented by several authors, including Billant and Chomaz [2000a], Lilly [1983], Riley and Lelong [2000], Riley et al. [1981]. As mentioned above, stratification typically suppresses vertical motion, which leads to different vertical and horizontal scales. Following the scaling arguments of Riley et al. [1981], choose the following length, horizontal velocity, and time scales:

$$\tilde{x}_H \sim \widetilde{L}_H \qquad \tilde{z} \sim \widetilde{L}_V \qquad \tilde{\mathbf{v}}_H \sim \widetilde{\mathcal{U}} \qquad \tilde{t} \sim \widetilde{L}_H/\tilde{u}$$
$$\alpha = \frac{\widetilde{L}_V}{\widetilde{L}_H} \qquad \tilde{w} \sim \frac{\widetilde{\mathcal{U}}}{\alpha}\mathrm{F}^2 \qquad \tilde{p} \sim \tilde{\rho}_o\widetilde{\mathcal{U}}^2 \qquad \tilde{\rho} \sim \tilde{\rho}_o\frac{\widetilde{\mathcal{U}}^2}{\tilde{g}\widetilde{L}_V}$$

with Froude number $\mathrm{F} = \widetilde{\mathcal{U}}/(\widetilde{\mathrm{N}}\widetilde{L}_V)$. The resulting nondimensional continuity, horizontal momentum, vertical momentum, and density equations of motion then become [Riley and Lelong, 2000]:

$$\nabla_H \cdot \vec{u}_H + \mathrm{F}^2\frac{\partial w}{\partial z} = 0 \tag{2.51a}$$

$$\frac{\partial}{\partial t}\mathbf{v}_H + \mathbf{v}_H \cdot \nabla_H\mathbf{v}_H + \mathrm{F}^2 w\frac{\partial}{\partial z}\vec{u}_H + \frac{1}{\mathrm{Ro}}\mathbf{e}_z \times \mathbf{v}_H = -\nabla_H p + \frac{1}{\alpha^2}\frac{1}{\mathrm{Re}}\nabla^2\mathbf{v}_H \tag{2.51b}$$

$$\alpha^2\mathrm{F}^2\left(\frac{\partial w}{\partial t} + \mathbf{v}_H \cdot \nabla w + \mathrm{F}^2 w\frac{\partial w}{\partial z}\right) = -\frac{\partial p}{\partial z} - \rho + \frac{\mathrm{F}^2}{\mathrm{Re}}\nabla^2 w \tag{2.51c}$$

$$\frac{\partial \rho}{\partial t} + \mathbf{v}_H \cdot \nabla\rho + \mathrm{F}^2 w\frac{\partial \rho}{\partial z} - w = \frac{1}{\alpha^2}\frac{1}{\mathrm{ScRe}}\nabla^2\rho \tag{2.51d}$$

where $\mathrm{Re} = \widetilde{\mathcal{U}}\tilde{L}/\tilde{\nu}$ is a Reynolds number based on energy containing length $\tilde{L}$, $\mathrm{Sc} = \nu/\tilde{\kappa}$ is the Schmidt number, and $\mathrm{Ro} = \widetilde{\mathcal{U}}f\tilde{L}$ is the Rossby number. As stratification becomes important ($\mathrm{F} \leq \mathcal{O}(1)$), all the terms with vertical velocity w diminish in importance and can be neglected. Evidence of this diminished vertical scale of motion is seen in the formation of horizontal "pancake eddies" in numerous numerical and experimental studies (examples are given in the sections on turbulence in wakes and grid turbulence). Equations (2.51) are often referred to as the low Froude or stratified turbulence equations.

2.1.8 Length Scales in Stratified Flows

The smallest scale of turbulent motion is taken as the familiar Kolmogorov length scale

$$\widetilde{\mathrm{L}}_\mathrm{k} = \left(\frac{\tilde{\nu}^3}{\widetilde{\epsilon}}\right)^{\frac{1}{4}} \tag{2.52}$$

where $\tilde{\nu}$ is kinematic viscosity and $\widetilde{\epsilon}$ is kinetic energy dissipation rate. $\widetilde{\mathrm{L}}_\mathrm{k}$ is taken as the smallest size of turbulent motion before being dissipated into internal energy (heat). At this small scale the length is typically assumed to be isotropic regardless of density stratification, although isotropy is disputed by Smyth and Moum [2000b].

Buoyancy tends to affect the larger vertical scales of motion. The largest scale of turbulent motion before buoyancy inhibits vertical motion (or the largest scale at which turbulent overturning can occur) is the Ozmidov or overturning scale:

$$\widetilde{\mathrm{L}}_\mathrm{o} = \left(\frac{\widetilde{\epsilon}}{\widetilde{\mathrm{N}}^3}\right)^{\frac{1}{2}}, \tag{2.53}$$

where $\widetilde{\mathrm{N}}$ is the Brunt-Väisälä (buoyancy) frequency:

$$\widetilde{\mathrm{N}} = \sqrt{-\frac{\tilde{g}}{\tilde{\rho}_0}\frac{\partial\tilde{\rho}}{\partial\tilde{z}}}\,.$$

$\widetilde{\mathrm{L}}_\mathrm{o}$ is derived in [Ozmidov, 1965] by finding the length such that buoyancy and inertial scales are equal. $\widetilde{\mathrm{L}}_\mathrm{o}$ is typically applied to flows with no mean shear.

If a flow is subject to a mean shear, the Corrsin scale is the largest scale at which the flow is unaffected by the shear, defined as:

$$\tilde{\mathrm{L}}_\mathrm{c} = \left(\frac{\widetilde{\epsilon}}{\widetilde{S}^3}\right)^{\frac{1}{2}} \tag{2.54}$$

where $\widetilde{S}$ is a measure of the applied shear.

Another measure of the overturning length is the Thorpe scale, $\widetilde{\mathrm{L}}_\mathrm{t}$ (Thorpe, 1977). It is computed by reordering the fluid elements such that the vertical density profile is statically stable. $\widetilde{\mathrm{L}}_\mathrm{t}$ is then taken to be the rms of the distance $\tilde{d}$ each element was moved to make the density profile stable.

$$\widetilde{\mathrm{L}}_\mathrm{t} = \left(\bar{\tilde{d}}^2\right)^{\frac{1}{2}} = \tilde{d}_{rms} \tag{2.55}$$

A measure of the distance a fluid particle could be displaced if all its vertical kinetic energy were converted to potential energy is the buoyancy scale $\tilde{\mathrm{L}}_\mathrm{b}$:

$$\tilde{\mathrm{L}}_\mathrm{b} = \frac{\tilde{w}_{rms}}{\widetilde{\mathrm{N}}} \tag{2.56}$$

where $\tilde{w}_{rms}$ is the rms vertical velocity. $\tilde{\mathrm{L}}_\mathrm{b}$ is shown to be closely proportional by Smyth and Moum [2000a], and is said to be an upper limit of L_t [Moum, 1996].

2.1.9 Additional Nondimensional Parameters in Stratified Flows

The Richardson number is commonly defined in stratified flows. Two common Richardson number definitions exist. The bulk Richardson number is simply the inverse F^2, and is a description of the overall influence of gravity on the flow. The local Richardson number is more commonly used, and is defined as:

$$\mathrm{Ri}_\mathrm{l} = \frac{\widetilde{\mathrm{N}}^2}{(d\widetilde{\mathcal{U}}/d\tilde{z})}\,.$$

Ri_l is thus a ratio of buoyancy force to shear forces in the flow. As Ri_l decreases, the flow is subject to shear instabilities. A common criterion used is $\mathrm{Ri}_\mathrm{l} < \frac{1}{4}$ for Kelvin-Helmholtz instability.

The buoyancy Reynolds number is defined by taking the ratio of $\widetilde{\mathrm{L}}_\mathrm{o}$ to $\widetilde{\mathrm{L}}_\mathrm{k}$ [Gibson, 1980, Gregg, 1987, Smyth and Moum, 2000a]:

$$\mathrm{Re}_\mathrm{b} = \left(\frac{\widetilde{\mathrm{L}}_\mathrm{o}}{\widetilde{\mathrm{L}}_\mathrm{k}}\right)^{\frac{4}{3}} = \frac{\widetilde{\epsilon}}{\tilde{\nu}\widetilde{\mathrm{N}}^2} \tag{2.57}$$

$\widetilde{\mathrm{L}}_\mathrm{o}$ is the maximum length at which eddies can vertically overturn before being affected by buoyancy [Ozmidov, 1965, Smyth and Moum, 2000a], while $\widetilde{\mathrm{L}}_\mathrm{k}$ is the maximum length scale that occurs before energy is dissipated via viscous effects. Re_b can be seen as a measure of the "bandwidth of length scales available to turbulence" [Gregg, 1987]. When $\mathrm{Re}_\mathrm{b} \approx \mathcal{O}(1)$, $\widetilde{\mathrm{L}}_\mathrm{o} \approx \widetilde{\mathrm{L}}_\mathrm{k}$ and vertical overturning (3D turbulence) does not occur [Riley and Lelong, 2000].

Chapter 3

Taylor-Green Simulations

This chapter contains results of numerical simulations initialized with Taylor-Green vortices and a linear density profile (i.e., uniform vertical density gradient). An overview of the Taylor-Green vortices is first given, followed by descriptions of the equations of motion and numerical method. Results are then presented.

3.1 Overview

Direct numerical simulations (DNS's) of flows initialized with Taylor-Green vortices were analyzed. The stratification of the flow is constant in time, and there is no ambient shear (i.e., decaying turbulent flow). Taylor-Green vortices were chosen because they can be considered idealizations of flows resulting from laboratory experiments in which a rake is pulled through a continuously stratified tank [e.g., Fincham et al., 1996, Praud et al., 2005]. Note, however, that our simulations are conducted with Schmidt number = 1, vs. $\mathrm{Sc_T} = 7$ for water. Briefly, the initial condition consisted of Taylor-Green vortices plus broad-banded noise with a level approximately 10% of the Taylor-Green vortex energy. The Taylor-Green vortices satisfied the following mathematical form:

$$\tilde{\mathbf{v}}_{tg} = \widetilde{\mathcal{U}} \cos(\tilde{\kappa}\tilde{z}) \left[\cos(\tilde{\kappa}\tilde{x}) \sin(\tilde{\kappa}\tilde{y}), -\sin(\tilde{\kappa}\tilde{x}) \cos(\tilde{\kappa}\tilde{y}), 0\right]$$

where $\widetilde{\mathcal{U}}$ determines the initial velocity scale, and $\tilde{L} = 1/\tilde{\kappa}$ determines the length scale for this field. Thus, for all simulation results, velocities are nondimensionalized by $\widetilde{\mathcal{U}}$, lengths by $\tilde{L}$, and time by $\tilde{L}/\widetilde{\mathcal{U}}$. The Froude number and Reynolds number characterizing the simulations are defined respectively as

$$\mathrm{F_L} = \frac{2\pi\widetilde{\mathcal{U}}}{\widetilde{\mathrm{N}}\tilde{L}}, \quad \mathrm{Re_L} = \frac{\widetilde{\mathcal{U}}\tilde{L}}{\tilde{\nu}}. \tag{3.1}$$

Simulations were run with nominal Froude numbers ($\mathrm{F_L}$) of 2 and 4, and nominal Reynolds number ($\mathrm{Re_L}$) between 200 and 9600. A summary of the different cases is given in Table 3.1. As described in Riley and de Bruyn Kops [2003], the simulated flow exhibits many characteristics of stratified turbulence. The horizontal length scales grow, and the vertical length scales decrease in time. This, combined with decoupling of the horizontal motions in the vertical direction, leads to the formation of horizontal "pancake" vortices. This behavior is evident after a dimensionless time, t, of about 15. In this study the focus is on time $t = 20$, when the two-dimensional character of the flow is strong but the flow is

Notation	F_L	Re_L	Sc	N_x	N_y	N_z
F2R2	2	200	1	256	256	128
F2R4	2	400	1	256	256	128
F2R8	2	800	1	256	256	128
F2R16	2	1600	1	256	256	256
F2R32	2	3200	1	512	512	256
F2R64	2	6400	1	768	768	384
F2R96	2	9600	1	1024	1024	512
F4R2	4	200	1	256	256	128
F4R4	4	400	1	256	256	128
F4R8	4	800	1	256	256	256
F4R16	4	1600	1	256	256	256
F4R32	4	3200	1	512	512	256
F4R64	4	6400	1	768	768	384
F4R96	4	9600	1	1024	1024	512

Table 3.1: Conditions for simulations of quasi-horizontal vortices. N_x, N_y, and N_z are the number of grid points in each direction.

also still very energetic. In particular, the relationship between kinetic energy dissipation rate and vertical shear, the definition of horizontal length scale, and parameterization of turbulence are examined.

The Taylor-Green initial condition and the periodic boundary conditions result in either two or four planes (depending on the size of the numerical domain) of maximum shear and the same number of planes of minimum shear. This is different from laboratory experiments or in natural settings (e.g., atmosphere and ocean) in which the number and spacing of planes of high and low shear adjusts to the flow conditions. As a consequence of this prescribed spacing, volume averages of shear and dissipation rate are difficult to interpret. Here we consider only the planes of maximum shear (either two of four) and denote the average over these planes by an overbar.

3.2 Equations of Motion

The flow fields are assumed to satisfy the incompressible continuity and Navier-Stokes equations subject to the Boussinesq approximation. Also, for better understanding of the underlying physics, the simulations are performed in a non-rotating frame of reference (i.e., the Coriolis term has been neglected since the simulation length scale is small compared to the scales acted upon by Coriolis forces.) Thus, the governing equations are those of (2.46) with no Coriolis term. In nondimensional form these equations are written as: (c.f. (2.46)):

$$\nabla \cdot \mathbf{v} = 0 \tag{3.2a}$$

$$\frac{\partial \mathbf{v}}{\partial t} + \mathbf{v} \cdot \nabla \mathbf{v} = -\frac{\nabla p}{\rho_o} - \left(\frac{2\pi}{F_L}\right)^2 \rho \mathbf{e}_z + \frac{1}{Re_L} \nabla^2 \mathbf{v} \tag{3.2b}$$

$$\frac{\partial \rho}{\partial t} + \mathbf{v} \cdot \nabla \rho + w \frac{d\bar{\rho}}{dz} = \frac{1}{Sc Re_L} \nabla^2 \rho . \tag{3.2c}$$

Here $\mathbf{v} = (u, v, w)$ is the velocity vector, ρ and p are the density and pressure deviations from their ambient values, $\mathbf{e}_z$ is a unit vector in the vertical (z) direction, $\mathrm{Sc} = \tilde{\nu}/\widetilde{D}$ is the Schmidt number (where $\widetilde{D}$ is the mass diffusivity), and $\mathrm{F_L}$ and $\mathrm{Re_L}$ are Reynolds and Froude numbers as defined in (3.1).

3.3 Numerical Method

The equations of motion are solved using a pseudo-spectral technique. The boundaries are taken to be periodic, allowing trigonometric, evenly spaced interpolation points and easy calculation of spatial derivatives via Fast Fourier Transform (FFT) [Trefethen, 2000]. The equations were advanced in time using a third-order Adams-Bashforth scheme with pressure projection (fractional step) method. Briefly, the pressure projection method is a two step method to solve for the velocity field. First, the velocity fields are advanced in time without the pressure term. Then, with the condition of incompressibility, pressure is expressed as a Poisson equation in terms of the newly calculated velocity fields. The Poisson equation is then solved for pressure, then the value obtained for pressure is used to modify or "correct" the velocity fields. Further discussion of the pressure projection method can be found in Perot [1993] and Chang et al. [2002].

In order to eliminate the majority of aliasing errors, a spherical wave-number truncation of approximately 15/16 κ_{max}, with κ_{max} the maximum wave number in the discrete Fourier transforms, was used. The momentum equation was advanced in time with the nonlinear term expressed in vorticity form, while the alternating time-step scheme suggested by Kerr [1985] was employed for the density field to approximate the skew-symmetric form of the non-linear term and thereby minimize aliasing. A skew-symmetric matrix is one in which the eigenvalues are all pure imaginary. This implies the non-linear term advects without causing growth or decay, and will not cause the model to fail. [Boyd, 2001, pg.213]

3.4 Simulation Results

3.4.1 Relation between vertical shear rate and kinetic energy dissipation rate

The vertical velocity in case F2R32 at four different times is shown in Fig. 3.1. The white bar in each figure connects two material points that are tracked in time. At $t = 17.5$ the flow is fairly quiescent, but by $t = 20$ a turbulent patch has begun to form in the vicinity of the white line. This patch continues to develop through time 22.5.

By slicing the domain vertically through the white line, the dynamics of this particular instability can be studied. In Fig. 3.2, the horizontal velocity in the direction of the white line is plotted for each of the four times. The figures are colored so that black indicates flow to the left and white indicates flow to the right. The gray bars above each panel in Fig. 3.2 correspond to the white lines in Fig. 3.1. At $t = 17.5$ there is little shearing action in the region of the gray bar, but by $t = 20$ moderate shearing has developed. By $t = 21.5$ the shearing is strong, and Kelvin-Helmholtz roll-ups are apparent. The roll-ups are even more apparent in the corresponding slice through the total density field at $t = 21.5$, published in de Bruyn Kops et al. [2003]. This type of qualitative analysis was repeated for a number of the simulation cases. While it was not always possible to find a clean Kelvin-Helmholtz roll-up associated with each turbulent patch, high vertical shear accompanied the

turbulence in all cases observed. Although this analysis does not provide a definitive answer, it strongly suggests vertical shear as the dominant mechanism for triggering turbulence in these simulations.

When developing theories and models for turbulence subject to strong stable stratification, it is common to assume that vertical shear of the horizontal motions causes most of the dissipation rate of kinetic energy, i.e.,

$$\nu S^2 \approx \varepsilon \ . \tag{3.3}$$

Here $\varepsilon = 2\nu e_{ij} e_{ij}$ is the kinetic energy dissipation rate, e_{ij} is the symmetric part of the viscous stress tensor τ_{ij}, and $S^2 = (\partial u/\partial z)^2 + (\partial v/\partial z)^2$ is the square of vertical shear. For instance, Billant and Chomaz [2001] and Riley and de Bruyn Kops [2003] make assumption (3.3) in order to estimate a vertical length scale; Shih et al. [2005] make this assumption in order to relate the buoyancy Reynolds number $\mathrm{Re_b}$, to the ratio of Reynolds and Richardson numbers. Support for (3.3) comes from numerical simulations, [e.g., Herring and Métais, 1989], and laboratory experiments that span a wide range of Reynolds numbers. In particular, the experiments of Fincham et al. [1996] show that $\nu S^2/\varepsilon \approx 0.9$, a result that is verified experimentally by Praud et al. [2005].

Analysis will begin by considering $\nu \langle S^2 \rangle / \langle \varepsilon \rangle$ for each of the cases in Table 3.1, shown in Figure 3.3, and each component $\langle \varepsilon \rangle_{ij}$ as a fraction of ε, shown in Figures 3.4(a) and (b). Here $\langle \cdot \rangle$ denotes a volume averaged quantity. For $\mathrm{Re_L} = 800$ at both $\mathrm{F_L} = 2$ and 4, the results are entirely consistent with those of Fincham et al. [1996] and Praud et al. [2005], in that vertical shear accounts for about 90% of the dissipation rate. The horizontal shear terms are very small, as are the contributions to ε of the normal strain rates. There is some dissipation due to vertical motion, particularly in the $\mathrm{F_L} = 4$ case, but it is small.

For $\mathrm{Re_L} = 200$, the flow conditions are markedly different with $\nu \langle S^2 \rangle / \langle \varepsilon \rangle \approx 0.6$. The contributions of each component of $\langle \varepsilon \rangle$ suggest a two-dimensional Stokes-like flow in which vertical motion is almost completely inhibited by gravity for both Froude number cases and the isotropic character of the pressure force causes all of the horizontal contributions of $\langle \varepsilon \rangle$ to approach their isotropic values (i.e., the flow never becomes turbulent). Note that in isotropic turbulence, the contributions to $\langle \varepsilon \rangle$ of the diagonal terms in the strain rate tensor are 13.3%, while those of the off-diagonal terms are 10%.

For Reynolds numbers above 800, the relative contributions of each component of $\langle \varepsilon \rangle$ change rapidly with increasing $\mathrm{Re_L}$. Physical reasoning suggests that all components of $\langle \varepsilon \rangle$ that depend on vertical velocity will increase as the flow becomes more turbulent and the vertical velocity increases. Furthermore, such reasoning suggests that this phenomenon will occur at lower $\mathrm{Re_L}$ for the $\mathrm{F_L} = 4$ cases than for the $\mathrm{F_L} = 2$ cases since the vertical motions are more strongly suppressed by gravity at lower Froude numbers. The simulation data is consistent with this reasoning in that $\langle \varepsilon \rangle_{33} / \langle \varepsilon \rangle$ increases with Reynolds number for both $\mathrm{F_L} = 2$ and 4 and is higher for the $\mathrm{F_L} = 4$ cases except at the highest Reynolds numbers. Considering this result alone, we might conclude that the simulated flow is insufficiently stratified for (3.3) to hold for the higher Reynolds number cases. Note, however, the curves for the $\langle \varepsilon \rangle_{11}$ and $\langle \varepsilon \rangle_{22}$ in Figures 3.4(a) and (b). The significant rise of these two contributions to $\langle \varepsilon \rangle$ shows that it is not just increasing vertical motion that causes $\nu \overline{S^2} / \langle \varepsilon \rangle$ to decrease to about 0.4 at $\mathrm{Re_L} = 9600$. Dissipation due to normal strains contributes significantly to the total dissipation rate at higher Reynolds numbers.

While it would be convenient if $\nu \langle S^2 \rangle / \langle \varepsilon \rangle \approx 1$ for all cases of strongly stratified turbulence, for most modeling and theoretical applications introduction of an order one constant

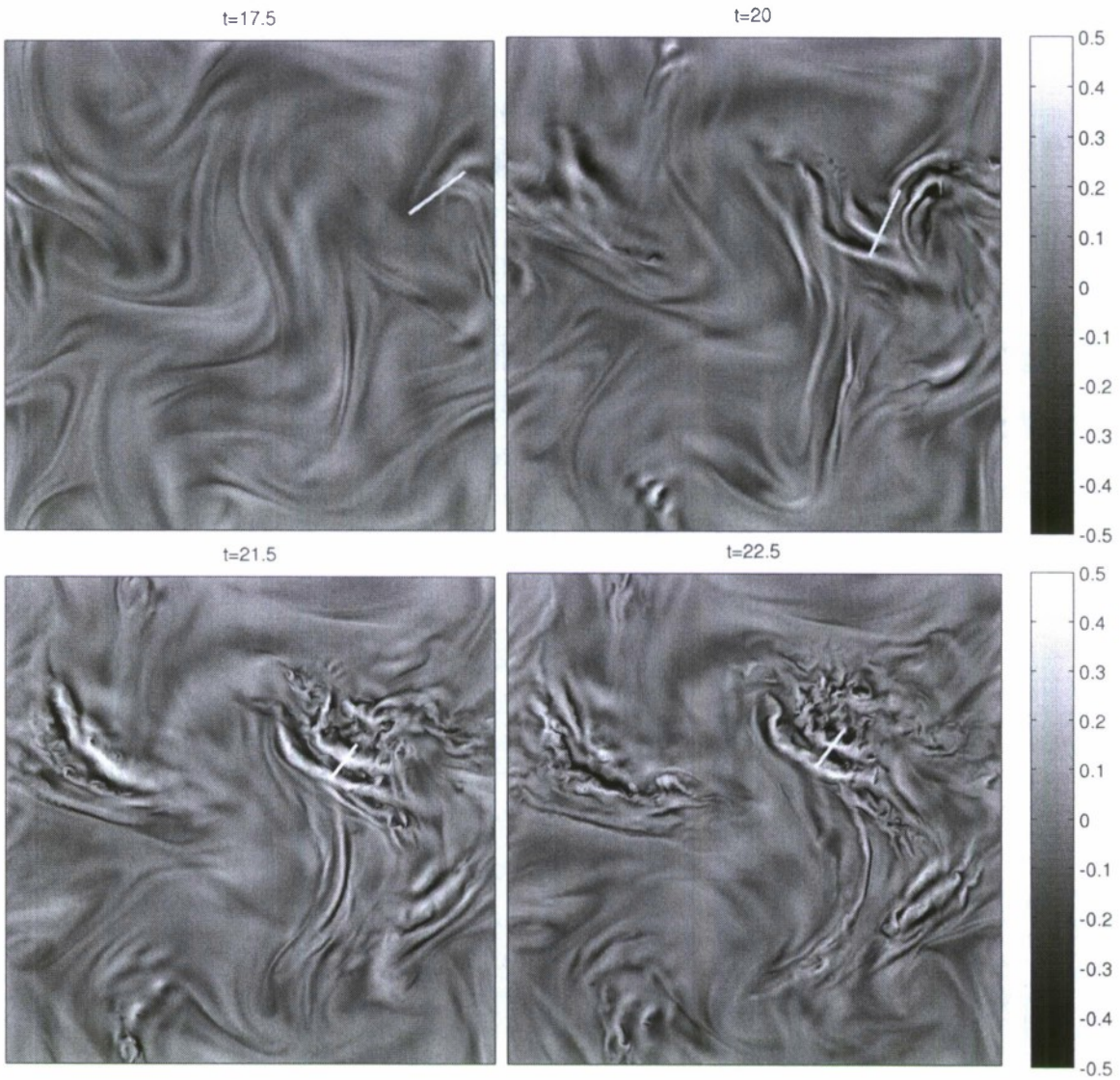

Figure 3.1: A horizontal slice through the vertical velocity field at the plane of maximum shear at four different times in a Taylor-Green simulation with Froude number 2 and Reynolds number 3200. The white bar connects two material points that move with time. The points start in a region of relative calm, experience an instability, and end up in a turbulent patch.

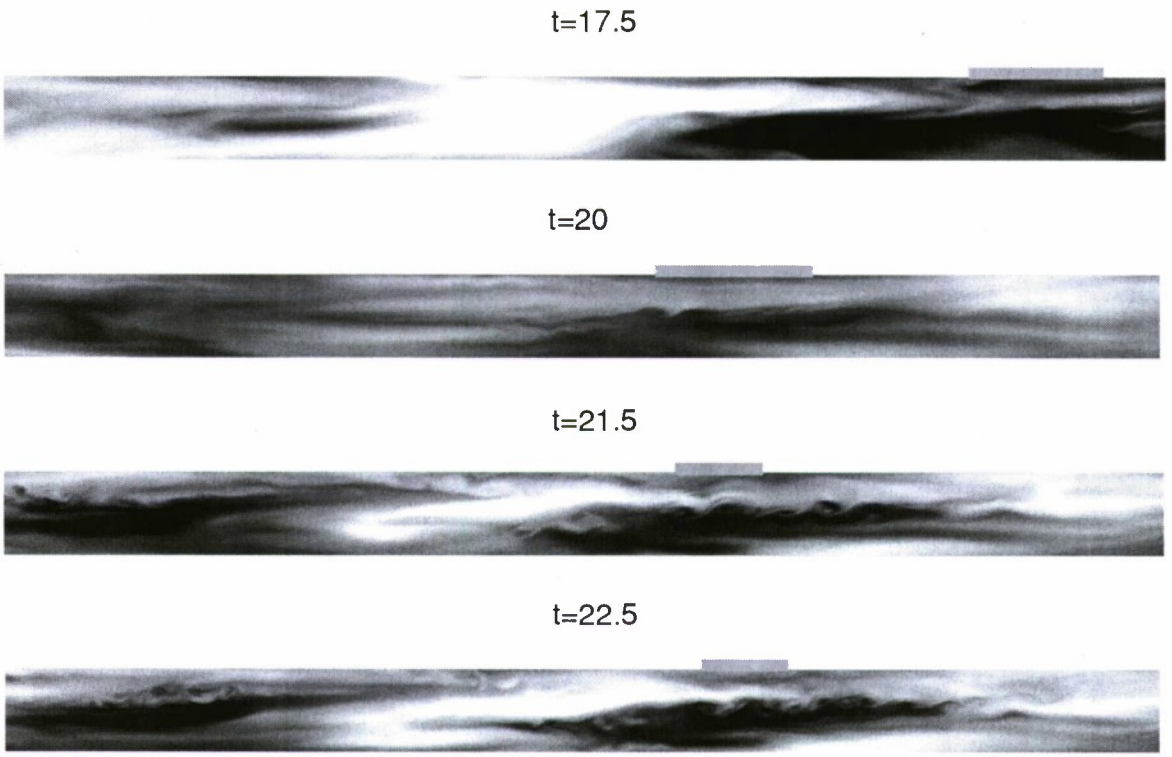

Figure 3.2: The horizontal speed on vertical planes aligned with the white bar in Fig. 3.1. Black indicates negative and white indicates positive. The gray bar above each panel corresponds to the white bar in Fig. 3.1.

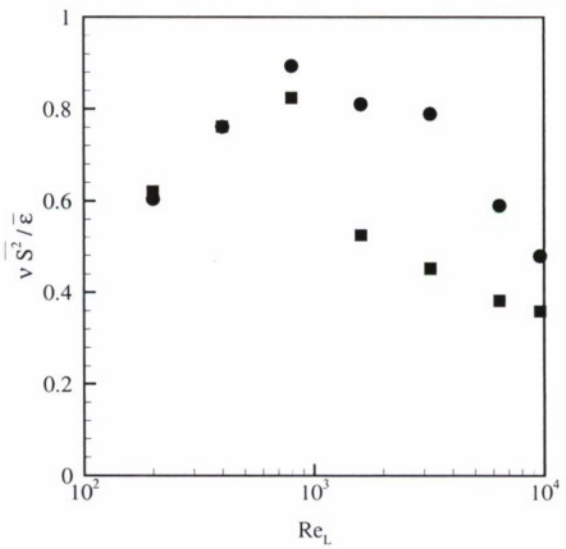

Figure 3.3: Ratio of $(\nu \langle S^2 \rangle)$ / $\langle \varepsilon \rangle$ vs. Re_L. $F_L = 2$ (•) : $F_L = 4$ (■)

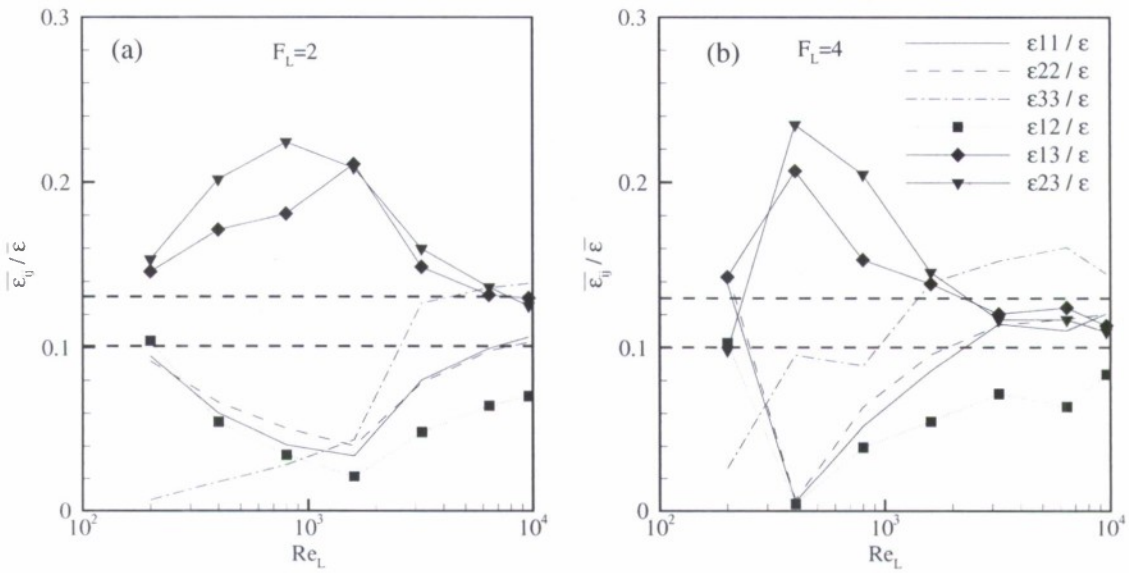

Figure 3.4: Contribution of the six independent terms of $\langle \varepsilon \rangle_{ij}$ normalized by total $\langle \varepsilon \rangle$ vs. $\mathrm{Re_L}$ for (a) $\mathrm{F_L}$=2 and (b) $\mathrm{F_L}$=4. The horizontal dashed lines mark the theoretical values for the normal and shear components in isotropic turbulence.

would be acceptable provided that S^2 and ε were well correlated. This correlation is considered in Figure 3.5 in which local values on the planes of high shear of νS^2 are plotted versus ε for two different simulation cases. In the top panel of the figure, it is apparent that for $\mathrm{Re_L} = 800$, not only are the square of the shear and the dissipation rate well correlated but there are very few points far from the diagonal. For this case, relation (3.3) is not only excellent on average, it is excellent locally in regions of high shear. In the bottom panel of the figure, the results for $\mathrm{Re_L} = 6400$ show that relation (3.3) is not very good even to within a multiplicative constant for this case.

3.4.2 Buoyancy Reynolds Number

In order to understand why the laboratory experiments conducted over a wide range of Reynolds numbers consistently show $\nu \langle S^2 \rangle / \bar{\varepsilon} \approx 0.9$ while our simulations support this relationship only for a fairly narrow range of Reynolds numbers, we consider now both laboratory and simulation data in terms of the buoyancy Reynolds number (2.57). This quantity has been used extensively in the parameterization of stratified turbulence, [e.g., Gibson, 1980, Gregg, 1987, Imberger and Boashash, 1986, Smyth and Moum, 2000a] and can be derived from the ratio of the Ozmidov scale (2.53) and the Kolmogorov scale (2.52).

For each of the simulation cases, the planar average buoyancy Reynolds number, $\langle \mathrm{Re_b} \rangle = \langle \varepsilon \rangle / \nu N^2$, is plotted versus $\mathrm{Re_L}$ in the top panel of Figure 3.6. Since, as shown by Riley and de Bruyn Kops [2003], the dissipation rates for all the cases are about the same, $\langle \mathrm{Re_b} \rangle$ is very nearly proportional to $\mathrm{Re_L}$. Note that $\langle \mathrm{Re_b} \rangle$ is computed at $t = 20$, whereas $\mathrm{Re_L}$ is a nominal value for the simulation. In the bottom panel of the same figure, $\nu \langle S^2 \rangle / \langle \varepsilon \rangle$ is plotted versus $\langle \mathrm{Re_b} \rangle$ for all the simulation cases. When $\langle \mathrm{Re_b} \rangle > 1$, the data for both $\mathrm{F_L}$ cases collapse very well onto a common curve that decreases rapidly with increasing $\langle \mathrm{Re_b} \rangle$. In the range $0.1 < \langle \mathrm{Re_b} \rangle < 1$, there is more scatter in the data but high values of $\nu \langle S^2 \rangle / \langle \varepsilon \rangle$

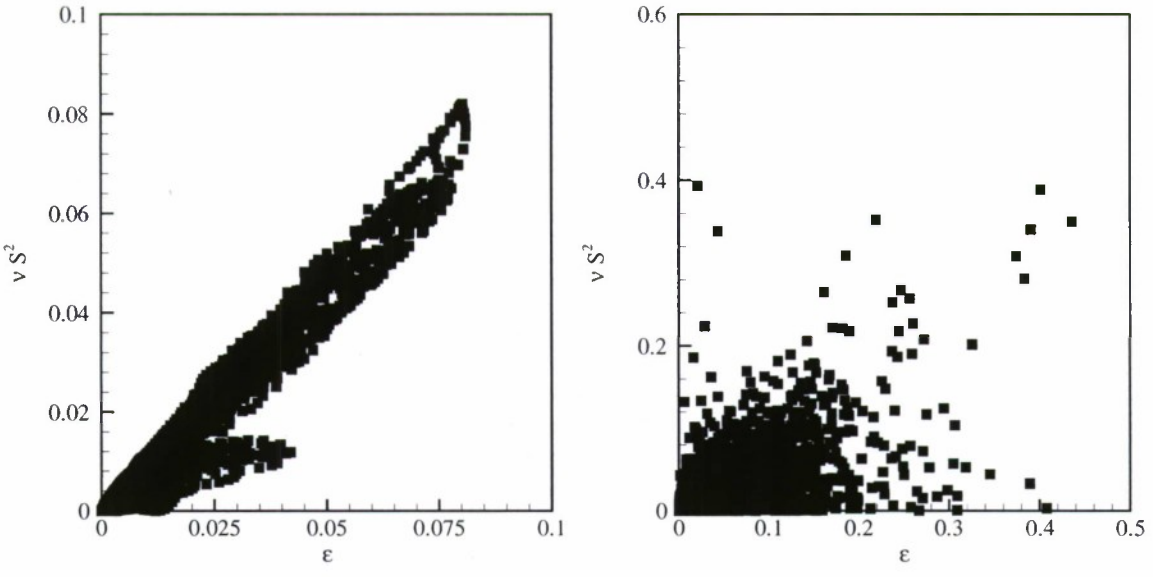

Figure 3.5: Scatter plot of νS^2 vs. ε for (a) $\mathrm{F_L} = 2$, $\mathrm{Re_L} = 800$ and (b) $\mathrm{F_L} = 2$, $\mathrm{Re_L} = 6400$.

are observed, consistent with results of other numerical simulations [e.g., Smyth and Moum, 2000b] as well as the laboratory results of Fincham et al. [1996] and Praud et al. [2005].

For the case of Fincham et al. [1996] with $\mathrm{Re_M} = 6100$ and $N = 2.3$ rad s^{-1} used in their Figure 8 to show the contribution of vertical shear to dissipation rate, the buoyancy Reynolds number is estimated to be about 0.2 at early time. For the case of Praud et al. [2005] with $\mathrm{Re_M} = 9000$ and $\mathrm{Fr_M} = 0.09$ used in their Figure 25, the buoyancy Reynolds number is estimated to be about 0.1 at early time. These values of $\mathrm{Re_b}$ correspond roughly to where $\nu \left\langle S^2 \right\rangle / \left\langle \varepsilon \right\rangle$ is maximum in Figures 3.6 (a) and (b).

In both laboratory experiments, however, ε decreases by several orders of magnitude over the duration of the experiment with a corresponding decrease in buoyancy Reynolds number. Neither Fincham et al. nor Praud et al. report a decrease in $\nu S^2/\varepsilon$ as the experiments evolved. This suggests that the behavior at low $\langle \mathrm{Re_b} \rangle$ observed in Figures 3.6 (a) and (b) is due to the simulated flows being laminar. Based on other statistics, we know this to be the case. It is likely, based on physical reasoning and the two sets of laboratory data, that vertical shear will account for 90% of the dissipation rate when $\langle \mathrm{Re_b} \rangle$ is order one or less provided that the flows are turbulent (of course, with $\langle \mathrm{Re_b} \rangle < 1$, turbulence is in the the quasi-2d sense).

3.4.3 Horizontal Length Scale

Riley and de Bruyn Kops [2003] postulate a length scale, L_h, for horizontal motions in order to define a horizontal Reynolds number, Re_h, and a horizontal Froude number, F_h, for their $\mathrm{F}_h^2\mathrm{Re}_h$ scaling. How L_h is to be computed for practical use is not discussed in that paper, but their derivation of the $\mathrm{F}_h^2\mathrm{Re}_h$ scaling implies that L_h can be defined in terms of u_h and ε (i.e., L_h is an advective length scale). Similarly, when $\mathrm{Re_b}$ is related to the square of a Froude number and a Reynolds number [e.g., Ivey and Imberger, 1991, Shih et al., 2005], an advective length scale, u_{rms}^3/ε, is assumed. Therefore, it is of interest whether the advective length scale is appropriate for the large scales of motion in the current simulations.

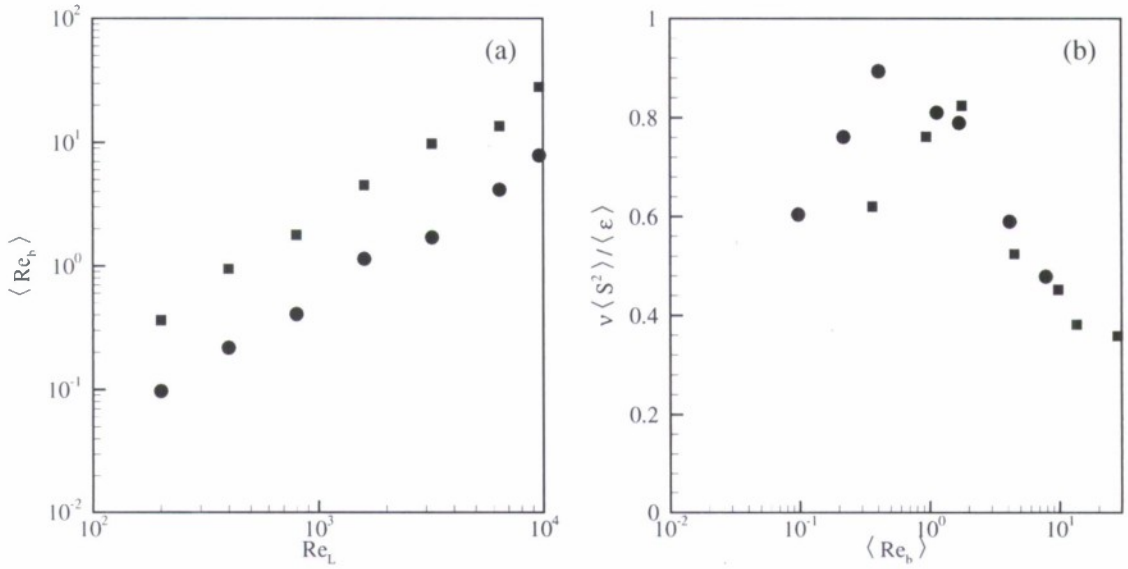

Figure 3.6: (a) $\langle \mathrm{Re_b} \rangle$ vs. $\mathrm{Re_L}$: (b) $\nu \langle S^2 \rangle / \langle \varepsilon \rangle$ (lower plot) for $\mathrm{F_L} = 2$ (•) : $\mathrm{F_L} = 4$ (■)

There is a strong theoretical argument that L_h should be related to u_h (or u_{rms}) and ε. With appropriate spatial and temporal averaging, advection can be expected to balance the viscous dissipation rate with an advective time scale $t_a \sim L_h/u_h$. If this is the case then

$$\frac{\partial}{\partial t}\frac{1}{2}u_h^2 \sim \varepsilon \sim \frac{u_h^3}{L_h} \tag{3.4}$$

or $L_h \sim u_h^3/\varepsilon$. While this analysis is generally accepted for theoretical estimates of the length scale, for practical application in simulations or laboratory experiments it may not be sufficient for several reasons. First, advection of horizontal kinetic energy only balances viscous dissipation when the horizontal and vertical kinetic energies and the potential energy are in equilibrium or when a carefully chosen interval in time is chosen for averaging. Second, horizontal kinetic energy is convected in the vertical direction and u_h^3/ε varies by several orders of magnitude between planes of high and low shear. As a consequence, L_h depends strongly on the definition of the spatial averages used in its computation.

To illustrate the difficulty in using u_h^3/ε for analyses of the current simulations, we consider an average advective length scale

$$\langle L_a \rangle_H = \frac{\langle u_h^3 \rangle_H}{\langle \varepsilon \rangle_H} \tag{3.5}$$

computed for the planes of maximum shear and plot it versus time in Fig. 3.7 for each of the simulation cases. Here $\langle \cdot \rangle_H$ denotes a planar averaged quantity. Averaging in this manner is justified by the fact that most of the kinetic energy and most of its dissipation rate is associated with the planes of maximum shear, and it is in the vicinity of those planes where turbulence occurs. If the spatial average is computed over the entire domain then the magnitude of $\langle L_a \rangle_H$ is smaller but the trend in time is similar. Note that with the the size of the numerical domain and the fact that the domain is periodic, the maximum permissible value for the horizontal length is 2π. $\langle L_a \rangle_H$ is therefore unphysically large for most of the

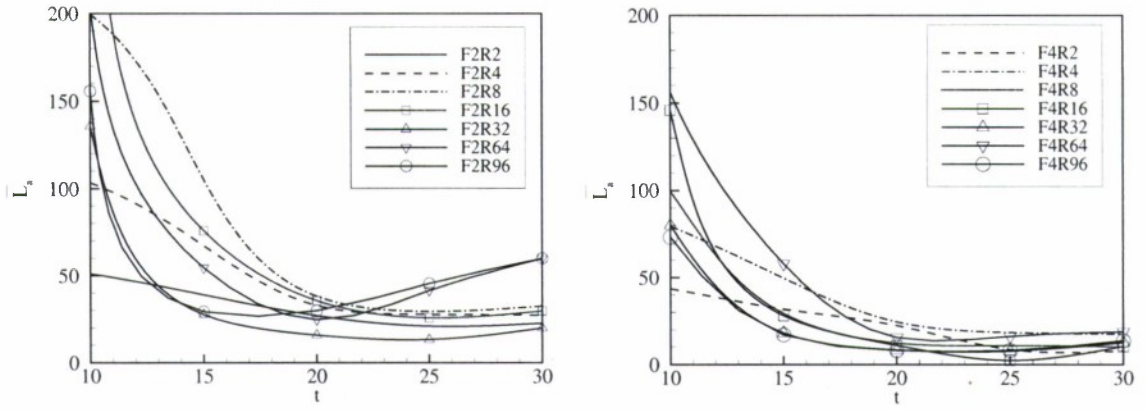

Figure 3.7: Advective length scale from (3.5).

simulation cases. Furthermore, $\langle L_a \rangle_H$ varies significantly between the simulations and does not grow continually in time, neither of which is consistent with information about the large scales of the flow gained from the stream function and energy spectra. It is concluded that $\langle L_a \rangle_H$ is not useful for estimating the size of the horizontal motions in the current simulations.

In order to arrive at an appropriate length scale for use with the $\mathrm{F}_h^2\mathrm{Re}_h$ scaling, we consider again the underlying physical justification for that scaling (i.e., that turbulence is triggered by vertical shearing between quasi-horizontal vortices). Based on this model, the appropriate length scale is the size of the horizontal vortices. From the horizontal stream function in Fig. 3.8, it is apparent that the size of these vortices increases from one quarter to one half the size of the computational domain between $t = 0$ and $t = 20$. A straightforward approach to computing L_h is to relate it to the average of the autocorrelations of u in the x-direction and of v in the y direction,

$$R(r) = \frac{1}{2}\frac{\langle u(x+r)u(x)\rangle_h}{\langle u\rangle_h} + \frac{1}{2}\frac{\langle v(y+r)v(y)\rangle_h}{\langle v\rangle_h} \,. \tag{3.6}$$

$R(r)$ is plotted in Fig. 3.8 for case F2R32 at two different times.

The horizontal length scale is defined in terms of the autocorrelation function as

$$\langle L_h \rangle_H = r \quad \text{where} \quad R(r) = 0 \,. \tag{3.7}$$

In Figure 3.9, $\langle L_h \rangle_H$ from (3.7) is plotted versus time for cases with high and low $\langle \mathrm{Re}_b \rangle_h$. The length scale increases with time as expected and never exceeds the limiting value of 2π. Unlike with $\langle L_a \rangle_H$, there is little difference between the cases, which is consistent with information gained from the streamfunction and from spectra that indicate little difference in the evolution of the large scales between the different cases. Furthermore, $\langle L_h \rangle_H$ grows monotonically in time as expected.

Also shown in Fig. 3.9 is the RMS horizontal velocity, the horizontal Froude number, and the horizontal Reynolds number. Since u_h decreases and $\langle L_h \rangle_H$ increases with time, F_h decreases in time. This data supports the theoretical argument by Riley and de Bruyn Kops [2003] that stably stratified flows with no energy input will eventually enter the strongly stratified regime even if the initial Froude number is much greater than unity. Note also from the figure that the Reynolds number increases as the flow evolves, reminiscent of two dimensional turbulence.

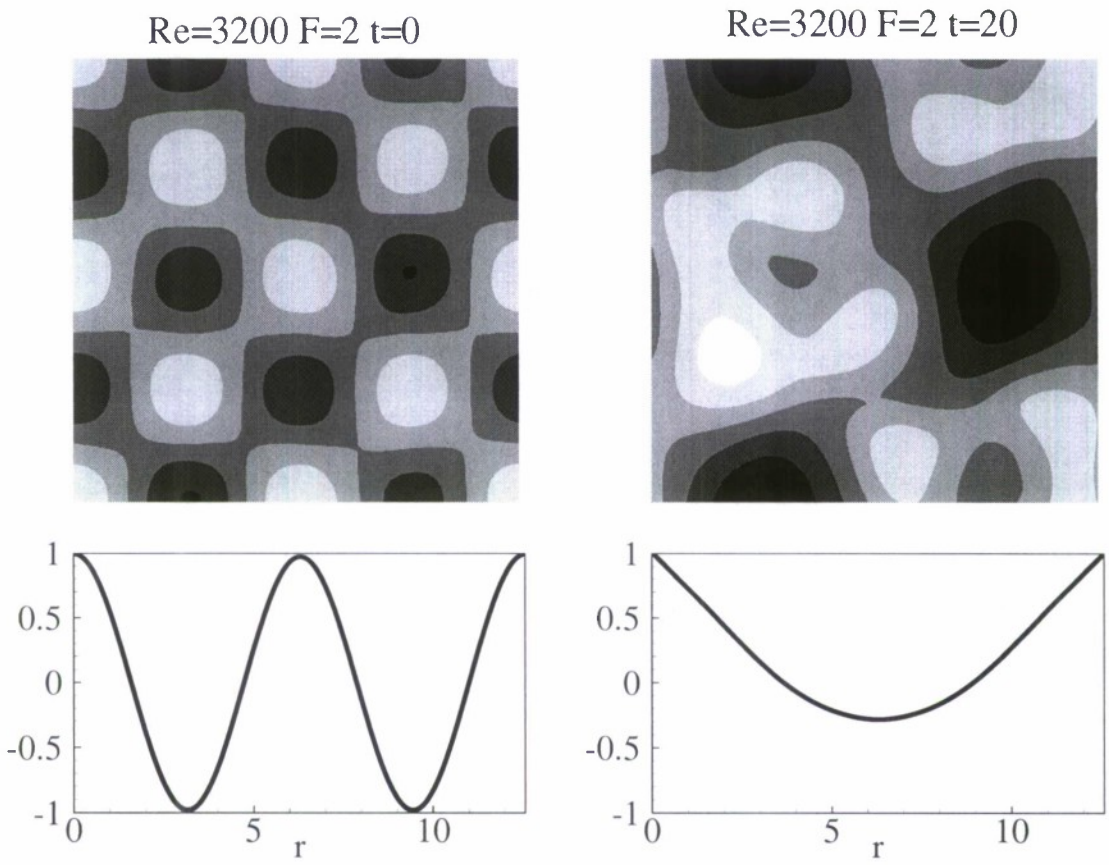

Figure 3.8: Horizontal stream function and corresponding autocorrelation function $R(r)$ for a plane of maximum shear at time $t = 0$ (left) and $t = 20$ (right). $R(r)$ is defined in (3.6)

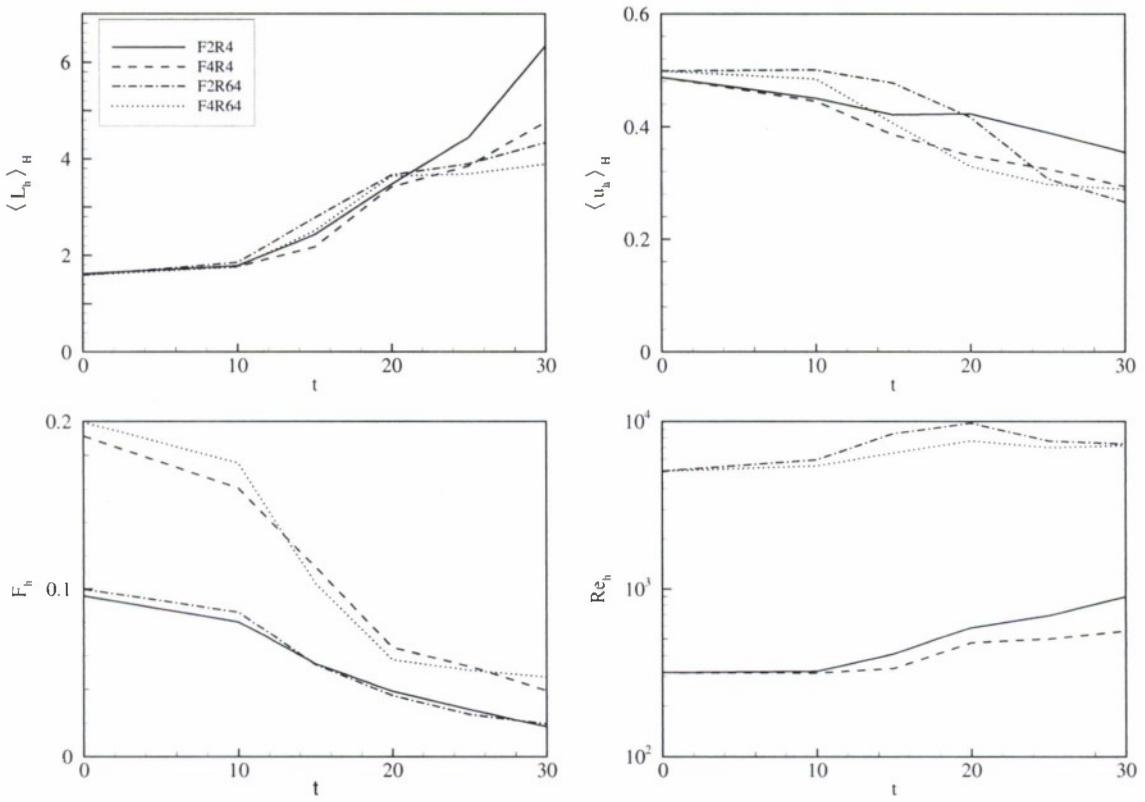

Figure 3.9: $\langle L_h \rangle_H$, $\langle u_h \rangle_H$, F_h, and Re_h versus time for two cases with low $\langle Re_b \rangle_H$ and two cases with high $\langle Re_b \rangle_H$.

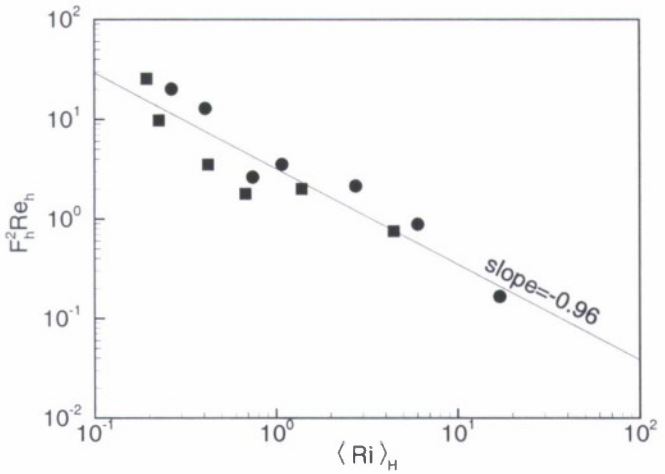

Figure 3.10: $F_h^2 Re_h$ versus $\langle Ri \rangle_H$. The solid line is the least-squares linear fit to the log of the quantities. The circles and squares represent the $F_L = 2$ and $F_L = 4$ cases, respectively.

3.4.4 Parameterization of Turbulence

Having determined a suitable length scale from which to compute F_h and Re_h in §3.4.3, we now consider the $F_h^2 Re_h$ scaling, its relationship to Re_b, and its utility for parameterizing turbulence in the simulated flows. Recall that the analysis in Riley and de Bruyn Kops [2003] relates the Richardson number, Ri, to $1/F_h^2 Re_h$ so that if $F_h^2 Re_h > \mathcal{O}(1)$ then Ri can be expected to be order one or less. Thus, a flow with $F_h^2 Re_h > \mathcal{O}(1)$ will be susceptible to Kelvin-Helmholtz instabilities and turbulence can be expected to develop. To investigate this argument, we examine the assumption that $Ri \sim 1/F_h^2 Re_h$ by plotting $F_h^2 Re_h$ versus $\langle Ri \rangle_H$ in Fig. 3.10 for all of the simulation cases. Here $\langle Ri \rangle_H$ is the planar averaged gradient Richardson number:

$$\langle Ri \rangle_H \equiv \frac{\frac{-g}{\rho_o}\left(\frac{\partial \rho}{\partial z} + \frac{d\bar{\rho}}{dz}\right)}{\left(\frac{\partial u}{\partial z}\right)^2 + \left(\frac{\partial v}{\partial z}\right)^2}, \tag{3.8}$$

The results are encouraging because the relationship $Ri \sim 1/F_h^2 Re_h$ holds over a two decade range of values. There is some scatter in the data, but there is no tendency to deviate from the relationship even at the extreme values of Ri. In fact, the stronger relationship $Ri \approx 1/F_h^2 Re_h$ is justified for the current simulations. The fact that $F_h^2 Re_h$ is a good estimate for the Richardson number combined with the conclusion from §3.4.1 that shear instabilities are the major cause of turbulence in the simulations leads us to conclude that $F_h^2 Re_h$ is a useful parameter for predicting if turbulence will occur in these flows.

As noted in the introduction of this paper, the buoyancy Reynolds number can be written in terms of a Reynolds number and the square of a Froude number. This leads to the question of whether $\langle Re_b \rangle_h$ and $F_h^2 Re_h$ are related quantities, and in Fig. 3.11 one is plotted versus the other for all the simulation cases. It is evident that the two parameterizations are equivalent to within the scatter of the data and an order one multiplicative constant, and that Riley and de Bruyn Kops [2003] arrived at a new physical justification for why Re_b has proven useful for parameterizing turbulence in stably stratified flows. This alternative justification may help in understanding the conditions under which Re_b can be used to

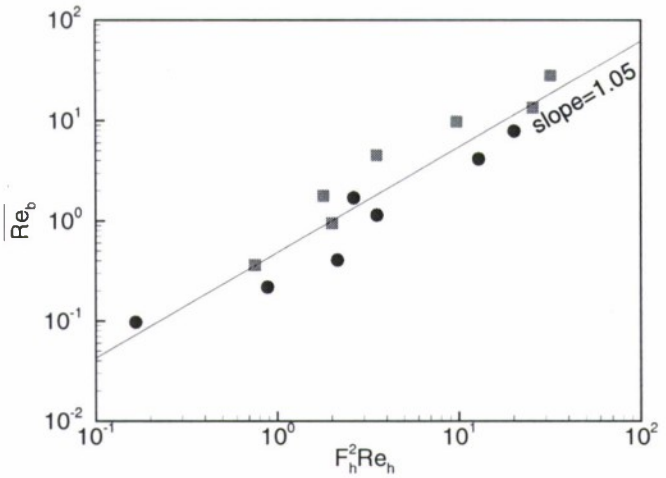

Figure 3.11: $\langle \mathrm{Re_b} \rangle_H$ versus $\mathrm{F}_h^2 \mathrm{Re}_h$. The solid line is the least-squares linear fit to the log of the quantities. The circles and squares represent the $\mathrm{F_L} = 2$ and $\mathrm{F_L} = 4$ cases, respectively.

parameterize turbulence, and how the parameterization might be improved.

In addition to providing an alternative physical explanation for the occurrence of turbulence under stable stratification, the $\mathrm{F}_h^2 \mathrm{Re}_h$ scaling has several attractive features compared with $\mathrm{Re_b}$. At the theoretical level, it involves two dimensionless groups, which is the number predicted for this problem by the Buckingham Pi theorem. This suggests that turbulence parameterization be considered in the two dimensional Froude-Reynolds number space rather than in the one dimensional domain of a modified Reynolds or modified Froude number. At the practical level for numerical and laboratory experimentalists, $\mathrm{F^2Re}$ can be used *a priori* to estimate if a flow can be expected to be sufficiently turbulent to be interesting for understanding oceanic and atmospheric flows.

Chapter 4

Vortex Street Simulations

This chapter contains results of numerical simulations initialized with a von Kármán vortex street and a hyperbolic tangent density profile. An overview of the simulations are given, followed by the kinetic and potential energy equations for non-uniform density stratification, numerical considerations, and simulation results. Emphasis is be placed on the effect of assuming a density gradient that is uniform in height when it may not be uniform, such as in a thermohaline staircase. Note that in keeping with the convention throughout this document, dimensional quantities are denoted with a tilde ($\tilde{\cdot}$), nondimensional quantities have no marking.

4.1 Overview

High resolution direct numerical simulations (DNS's) of a perturbed von Kármán vortex street were performed, simulating the resulting flow of an object's wake (Figure 4.1). The initial conditions consist of three vortex pairs and low-level noise. Each simulated flow was conducted with no ambient shear and density stratification that was held constant in time, to represent the persistent stratification naturally found in a thermohaline staircase (§1.2.5) or atmospheric layer transition (§1.1.1). The wake has zero mean velocity, which is similar to that generated by a self-propelled object (although Meunier and Spedding [2006] note that it is very difficult to obtain a truly momentumless wake in a stratified fluid). Each vortex was initialized with the following velocity profile [de Bruyn Kops et al., 2003]:

$$\tilde{\mathrm{V}}_\theta = \tilde{\mathcal{U}} \frac{\tilde{r}}{\tilde{r}_m} \exp\left[0.5\left(1 - \left(\frac{\tilde{r}}{\tilde{r}_m}\right)^2\right)\right] \mathrm{sech}^2\left(\frac{\tilde{z}}{\tilde{\delta}_\mathcal{U}}\right) \tag{4.1}$$

where $\tilde{\mathcal{U}}$ is the initial velocity scale, $\tilde{r}_m$ is a radial length scale, $\tilde{\delta}_\mathcal{U}$ is the vertical length scale, and $\tilde{r} = \sqrt{\tilde{x}^2 + \tilde{y}^2}$ and $\tilde{z}$ are the radial and vertical position. The separation distances between vortex centers in the $\tilde{x}$ and $\tilde{y}$ directions were $\tilde{s}_x = 2\tilde{r}_m$ and $\tilde{s}_y = 1.5\tilde{r}_m$.

In creating the initial flow condition, noise was applied to the vortex horizontal and vertical length scales $\tilde{r}_m$, $\tilde{\delta}_\mathcal{U}$, and vortex separation distances $\tilde{s}_x$, $\tilde{s}_y$; each was randomly perturbed up to 5% of its corresponding scale. For example, the vertical scale for each vortex was calculated as $\tilde{\delta}_\mathcal{U} + 0.05\lambda\tilde{\delta}_\mathcal{U}$, and the $\tilde{y}$ positions for the positive vortices were determined as $\tilde{L}_y/2 + \tilde{s}_y/2 + 0.05\lambda\tilde{s}_y$, where λ is a [-1 1] uniformly distributed random number and $\tilde{L}_y$ is the spanwise (y) domain width.

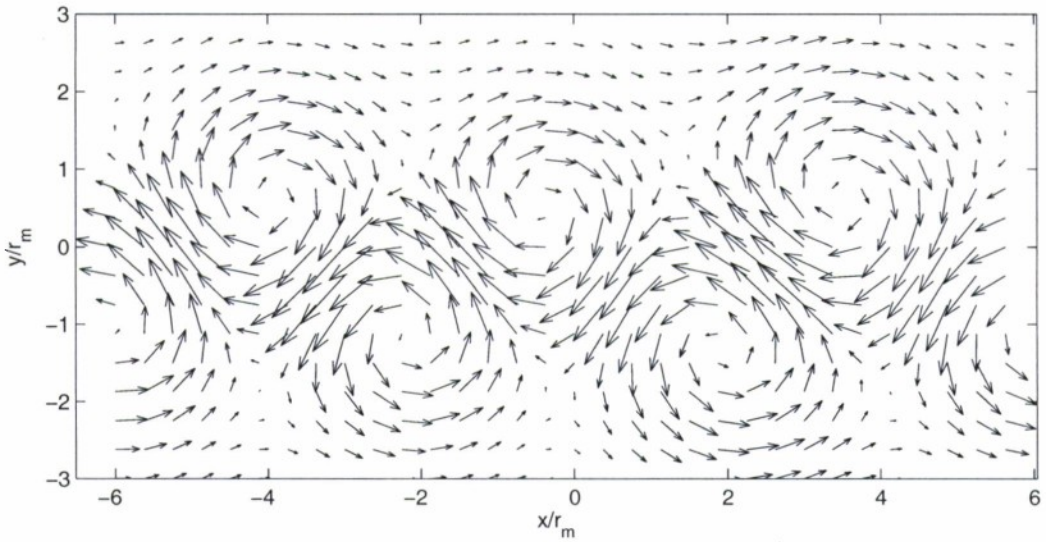

Figure 4.1: Center plane of vortex street initial condition. Arrow length represents fluid velocity.

The ambient density $\tilde{\bar{\rho}}(\tilde{z})$ was imposed with a hyperbolic tangent vertical profile:

$$\tilde{\bar{\rho}}(\tilde{z}) = \frac{\Delta\tilde{\bar{\rho}}}{2}\tanh\left(\frac{-\tilde{z}}{\tilde{\delta}_\rho}\right), \tag{4.2}$$

from which the density stratification $d\bar{\rho}(z)/dz$ is obtained:

$$\frac{d\tilde{\bar{\rho}}(\tilde{z})}{d\tilde{z}} = -\frac{1}{\tilde{\delta}_\rho}\frac{\Delta\tilde{\bar{\rho}}}{2}\mathrm{sech}^2\left(\frac{-\tilde{z}}{\tilde{\delta}_\rho}\right), \tag{4.3}$$

where $\Delta\tilde{\bar{\rho}} = \tilde{\bar{\rho}}_{top} - \tilde{\bar{\rho}}_{bottom}$ is the difference in density between the top and bottom of the numerical domain, $\tilde{z}$ is the vertical position and $\tilde{\delta}_\rho$ is a vertical length scale of the density profile. Since the stratification is a function of vertical height, the buoyancy frequency $\widetilde{\mathrm{N}}$ will also be a function of height. It will be convenient to define a global buoyancy frequency $\widetilde{\overline{\mathrm{N}}}$ to describe the average ambient density stratification $\Delta\tilde{\bar{\rho}}/\Delta\tilde{z} = (\tilde{\bar{\rho}}_{top} - \tilde{\bar{\rho}}_{bottom})/(\tilde{z}_{top} - \tilde{z}_{bottom})$, as well as a local buoyancy frequency $\widetilde{\mathrm{N}}(z)$:

$$\widetilde{\overline{\mathrm{N}}}^2 = -\frac{\tilde{g}}{\tilde{\rho}_0}\frac{\Delta\tilde{\bar{\rho}}}{\Delta\tilde{z}} \tag{4.4}$$

$$\widetilde{\mathrm{N}}^2(z) = -\frac{\tilde{g}}{\tilde{\rho}_0}\frac{d\tilde{\bar{\rho}}(\tilde{z})}{d\tilde{z}}. \tag{4.5}$$

4.2 Theoretical Considerations

4.2.1 Kinetic Energy

The kinetic energy equation is formed by taking the dot product of the velocity vector $\tilde{\mathbf{v}}$ and the momentum equation (2.46b) (in which the Boussinesq approximation is made and

gravity is the only body force). This yields (in indicial notation):

$$\frac{\partial \widetilde{E}_k}{\partial \tilde{t}} + \tilde{u}_j \frac{\partial \widetilde{E}_k}{\partial \tilde{x}_j} = -\tilde{u}_i \frac{\partial \tilde{p}}{\partial \tilde{x}_i} - \frac{\tilde{g}}{\tilde{\rho}_0} \tilde{\rho} \tilde{u}_3 + \frac{\partial (\tilde{u}_i \widetilde{\tau}_{ji})}{\partial \tilde{x}_j} - \widetilde{\tau}_{ji} \frac{\partial \tilde{u}_i}{\partial \tilde{x}_j} . \tag{4.6}$$

Here $\widetilde{E}_k = 1/2\ (\tilde{u}_i \tilde{u}_i)$ is the kinetic energy per unit mass, $\tilde{x}_i$ is the direction vector, and $\widetilde{\tau}_{ji}$ is the viscous stress tensor for a Newtonian fluid. Equation (4.6) can be broken into horizontal (i = 1,2) and vertical (i = 3) contributions (denoted with subscripts H and V respectively):

$$\frac{\partial \widetilde{E}_k}{\partial t} = \frac{\partial \widetilde{E}_H}{\partial t} + \frac{\partial \widetilde{E}_V}{\partial \tilde{t}} \tag{4.7}$$

$$\frac{\partial \widetilde{E}_H}{\partial \tilde{t}} = -\widetilde{T}_H - \widetilde{P}_H + \widetilde{W}_H - \widetilde{\varepsilon}_H - \widetilde{\phi} \tag{4.8}$$

$$\frac{\partial \widetilde{E}_V}{\partial \tilde{t}} = -\widetilde{T}_V - \widetilde{P}_V - \widetilde{B} + \widetilde{W}_V - \widetilde{\varepsilon}_V + \widetilde{\phi} , \tag{4.9}$$

where

$$\begin{array}{l|l} \widetilde{E}_h = \frac{\tilde{u}_H \tilde{u}_H}{2} & \widetilde{E}_v = \frac{\tilde{u}_V \tilde{u}_V}{2} \\ \widetilde{T}_H = \tilde{\mathbf{v}} \cdot \widetilde{\nabla} \widetilde{E}_h & \widetilde{T}_V = \tilde{\mathbf{v}} \cdot \widetilde{\nabla} \widetilde{E}_v \\ \widetilde{P}_H = \tilde{\mathbf{u}}_\mathbf{H} \cdot \widetilde{\nabla}_H \tilde{p} & \widetilde{P}_V = \tilde{u}_V \frac{\partial \tilde{p}}{\partial \tilde{z}} \\ \widetilde{W}_H = \frac{\partial (\tilde{\mathbf{u}}_\mathbf{H} \tilde{\tau}_{jH})}{\partial \tilde{x}_j} & \widetilde{W}_V = \frac{\partial (\tilde{u}_V \tilde{\tau}_{jV})}{\partial \tilde{x}_j} \\ \widetilde{\varepsilon}_H = 2\tilde{\nu} \tilde{e}_{Hj} \tilde{e}_{Hj} & \widetilde{\varepsilon}_V = 2\tilde{\nu} \tilde{e}_{Vj} \tilde{e}_{Vj} \\ \widetilde{\phi} = 2\tilde{\nu} (\tilde{e}_{13} \tilde{r}_{13} + \tilde{e}_{23} \tilde{r}_{23}) & \widetilde{B} = \frac{\tilde{g}}{\tilde{\rho}_0} \tilde{\rho} \tilde{u}_z \end{array}$$

In the above equations $\tilde{\mathbf{v}} = (\tilde{u}, \tilde{v}, \tilde{w})$ is the velocity vector, $\tilde{\mathbf{u}}_\mathbf{H} = (\tilde{u}, \tilde{v})$ is the horizontal component of the velocity vector, $\widetilde{\varepsilon} = 2\tilde{\nu} \tilde{e}_{ij} \tilde{e}_{ij}$ is the dissipation rate of kinetic energy, $\widetilde{\phi} = 2\tilde{\nu} (\tilde{e}_{13} \tilde{r}_{13} + \tilde{e}_{23} \tilde{r}_{23})$ is a coupling term between vertical and horizontal kinetic energy, $\tilde{e}_{ij}$ and $\tilde{r}_{ij}$ are the symmetric and anti-symmetric tensors of $\frac{\partial \tilde{u}_i}{\partial \tilde{x}_j}$:

$$\tilde{e}_{ij} = \frac{1}{2} \left(\frac{\partial \tilde{u}_i}{\partial \tilde{x}_j} + \frac{\partial \tilde{u}_j}{\partial \tilde{x}_i} \right) \tag{4.10}$$

$$\tilde{r}_{ij} = \frac{1}{2} \left(\frac{\partial \tilde{u}_i}{\partial \tilde{x}_j} - \frac{\partial \tilde{u}_j}{\partial \tilde{x}_i} \right) \tag{4.11}$$

Nondimensionalization

Using the scaling outlined in §4.4.1 below, equations (4.8) and (4.9) can be written in nondimensional form as:

$$\frac{\partial E_H}{\partial t} = -T_H - P_H + W_H - \varepsilon_H - \phi \tag{4.12}$$

$$\frac{\partial E_V}{\partial t} = -T_V - P_V - B + W_V - \varepsilon_V + \phi , \tag{4.13}$$

where

$$
\begin{array}{l|l}
E_H = \frac{u_H u_H}{2} & E_V = \frac{u_V u_V}{2} \\
T_H = \mathbf{v} \cdot \nabla E_H & T_V = \mathbf{v} \cdot \nabla E_V \\
P_H = \mathbf{u_H} \cdot \nabla_H p & P_V = u_V \frac{\partial p}{\partial z} \\
W_H = \frac{1}{\mathrm{Re_r}} \frac{\partial (\mathbf{u_H} \tau_{jH})}{\partial x_j} & W_V = \frac{1}{\mathrm{Re_r}} \frac{\partial (u_V \tau_{jV})}{\partial x_j} \\
\varepsilon_H = \frac{2}{\mathrm{Re_r}} e_{Hj} e_{Hj} & \varepsilon_V = \frac{2}{\mathrm{Re_r}} e_{Vj} e_{Vj} \\
\phi = \frac{2}{\mathrm{Re_r}} (e_{13} r_{13} + e_{23} r_{23}) & B = \left(\frac{2\pi}{\mathrm{F_r}} \right)^2 \rho u_z \ ,
\end{array}
$$

and $\mathrm{Re_r}$, $\mathrm{F_r}$, Sc are defined in (4.28). Further discussion of each term is given in the results section of this chapter.

4.2.2 Available Potential Energy for Non-uniform Density Stratification

Potential energy in a geophysical setting usually involves the concepts of available and background potential energy, first suggested by Lorenz [1955]. He noted that in order to convert the total potential energy in the Earth's atmosphere to kinetic energy, the temperature needed to reach absolute zero and all mass needed to be located at sea level. Such conditions cannot readily occur. (It is estimated that potential energy makes up 25% of the total energy (internal + potential + kinetic) in the Earth's atmosphere, while only 2% is kinetic energy [Gill, 1982, pg.81]). Instead, the potential energy $\widetilde{E}_p$ that is available for conversion to kinetic energy is said to be the result of any deviation from a background (or rest) potential energy $\widetilde{E}_b$. $\widetilde{E}_b$ is a state that would exist if the fluid was adiabatically redistributed (i.e., no heat transfer) to a minimum energy state. The available potential energy is the total potential energy, $\widetilde{\mathcal{P}}$, minus the background potential energy:

$$\widetilde{E}_p = \widetilde{\mathcal{P}} - \widetilde{E}_b \, . \tag{4.14}$$

Initially, this might seem like a straightforward method for obtaining the available potential energy in a system. However, while $\widetilde{\mathcal{P}}$ is typically defined as $\iiint \tilde{\rho}_t \tilde{g} \tilde{z} \, d\tilde{x} \, d\tilde{y} \, d\tilde{z}$, (where $\tilde{\rho}_t = \tilde{\rho}_0 + \bar{\tilde{\rho}}(z) + \tilde{\rho}$ is the total density, equal to the sum of reference, ambient and fluctuating components), several methods of obtaining $\widetilde{E}_p$ exist. Typically, adiabatic redistribution is performed by sorting the density field so that the highest density parcels are in the lowest vertical position. The redistributed density field, $\tilde{\rho}_t^*$, is then used to calculate background potential energy $\widetilde{E}_b = \iiint \tilde{\rho}_t^* \tilde{g} \tilde{z} \, d\tilde{x} \, d\tilde{y} \, d\tilde{z}$ [e.g., Staquet, 2000, Winters et al., 1995]. Another related method to calculate $\widetilde{E}_b$ is by "Thorpe reordering," [Thorpe, 1977], in which the density is also adiabatically redistributed via sorting, but in this case the distance (absolute or rms) each fluid element traversed, $\tilde{\eta}$, to obtain the minimum energy state is used to calculate the background potential energy $\iiint \tilde{\rho}_t \tilde{g} (\tilde{z} - \tilde{\eta}) \, d\tilde{x} \, d\tilde{y} \, d\tilde{z}$ [Smyth and Moum, 2000a, Smyth et al., 2001]. A third method of obtaining $\widetilde{E}_b$, suggested by Tseng and Ferziger [2001], involves taking the probability density function (PDF) of $\tilde{\rho}_t$, which can be thought of as a method of sorting the field into a minimum energy state. With the PDF of $\tilde{\rho}_t$, the vertical position of each parcel in a minimum energy state can be found, then integrated over the domain height to find $\widetilde{E}_b$.

While the above methods for obtaining $\widetilde{E}_b$ rely on sorting methods, thus avoiding the need for derivatives of density stratification, there are several drawbacks. First, as pointed out in Winters et al. [1995], sorting methods can only provide an estimate of background potential energy, since the vertical position is discretized by the numerics, where in a physical system no such discretization exists. Second, since simulations are now becoming large (it is not uncommon for simulations to be the order of 1 billion gridpoints), sorting or creating

a PDF of a large field can take too long to be practical if values are to be obtained while the simulation is running. Lastly, to gain insight into Eulerian energetics, it is desirable to calculate $\widetilde{E}_p$ on a local basis (i.e., at each grid point), whereas the above methods are only defined on a volume average basis. A method for computing $\widetilde{E}_p$ on a local basis is derived below.

Available potential energy for uniformly stratified flows is usually defined locally as [e.g., Gill, 1982, p.140]:

$$\widetilde{E}_p = -\frac{1}{2}\frac{\tilde{g}}{d\bar{\tilde{\rho}}/d\tilde{z}}\tilde{\rho}^2\,, \tag{4.15}$$

where $\tilde{\rho}(\tilde{x},\tilde{y},\tilde{z},\tilde{t})$ is the fluctuation from the undisturbed density $\bar{\tilde{\rho}}$, and $d\bar{\tilde{\rho}}/d\tilde{z}$ is constant in space and time. When density stratification is non-uniform, the definition of potential energy is more complicated than for uniform stratification, and (4.15) will not be accurate. This complication arises from the fact that the derivative of the stratification is non-zero (i.e., $d^2\bar{\tilde{\rho}}(\tilde{z})/d\tilde{z}^2 \neq 0$) [Holliday and McIntyre, 1981]. A method to obtain an accurate expression for potential energy in an incompressible fluid with a non-uniform density stratification was put forth by Holliday and McIntyre [1981], who begin by defining available potential energy as the integral of the displacement of a fluid particle from its undisturbed state ($\tilde{\zeta}$),

$$\widetilde{E}_p(\tilde{z},\tilde{\zeta}) = -\int_0^{\tilde{\zeta}} \tilde{g}\hat{\tilde{\zeta}}\frac{d}{d\tilde{z}}\bar{\tilde{\rho}}(\tilde{z}-\hat{\tilde{\zeta}})d\hat{\tilde{\zeta}}\,, \tag{4.16}$$

where $\hat{(\cdot)}$ denotes a dummy integration variable. Since the numerical simulations involve a field of density fluctuations $\tilde{\rho}(x,y,z,t)$, it is advantageous to write $\widetilde{E}_p$ in terms of $\bar{\tilde{\rho}}(z)$ and $\tilde{\rho}(\tilde{x},\tilde{y},\tilde{z},\tilde{t})$, rather than $\tilde{z}$ and $\tilde{\zeta}$. Conversion to $\bar{\tilde{\rho}}(z)$ and $\tilde{\rho}(\tilde{x},\tilde{y},\tilde{z},\tilde{t})$ is possible because $\tilde{\rho}(\tilde{x},\tilde{y},\tilde{z},\tilde{t})$ contains Lagrangian information required to compute (4.16). Converting to $\bar{\tilde{\rho}}(\tilde{z})$ and $\tilde{\rho}(\tilde{x},\tilde{y},\tilde{z},\tilde{t})$ can be achieved by first defining a potential function $\widetilde{\Phi}\{\}$ as

$$\widetilde{\Phi}\{\bar{\tilde{\rho}}(z)\} = \tilde{g}\tilde{z}. \tag{4.17}$$

Provided the undisturbed stratification $\bar{\tilde{\rho}}(z)$ is stable everywhere, (4.16) can be written in the following form [Holliday and McIntyre, 1981]:

$$\widetilde{E}_p = -\int_0^{\tilde{\rho}} \left[\widetilde{\phi}\{\bar{\tilde{\rho}}(z)+\hat{\tilde{\rho}}\} - \widetilde{\phi}\{\bar{\tilde{\rho}}(\tilde{z})\}\right] d\hat{\tilde{\rho}}\,, \tag{4.18}$$

where $\hat{\tilde{\rho}}$ is a dummy integration variable and the spatial dependence $(\tilde{x},\tilde{y},\tilde{z})$ of $\tilde{\rho}$ is implied. For the specific hyperbolic tangent $\bar{\tilde{\rho}}(\tilde{z})$ given in (4.2), (4.17) can be shown to be

$$\widetilde{\Phi}\{\bar{\tilde{\rho}}(\tilde{z})\} = -\tilde{g}\delta_{\tilde{\rho}}\,\mathrm{arctanh}\left(\frac{\bar{\tilde{\rho}}(\tilde{z})}{\tilde{\varrho}}\right), \tag{4.19}$$

where $\varrho = \Delta\tilde{\rho}/2$, obtained from (4.2), is introduced simply for notational purposes. Substituting (4.19) into (4.18) yields the following expression for $\widetilde{E}_p$ (where the spatial dependence of $\tilde{\rho}$, $\bar{\tilde{\rho}}$ is implied):

$$\widetilde{E}_p = \tilde{g}\tilde{\delta}_\rho\left[(\bar{\tilde{\rho}}+\tilde{\rho})\mathrm{arctanh}\left(\frac{\tilde{\varrho}\tilde{\rho}}{\tilde{\varrho}^2-\bar{\tilde{\rho}}\tilde{\rho}-\bar{\tilde{\rho}}^2}\right)+\frac{\tilde{\varrho}}{2}\ln\left(\frac{\tilde{\varrho}^2-(\bar{\tilde{\rho}}+\tilde{\rho})^2}{\tilde{\varrho}^2-\bar{\tilde{\rho}}^2}\right)\right] \tag{4.20}$$

The time derivative of $\widetilde{E}_p$ can be found by use of the chain rule:

$$\frac{\partial\widetilde{E}_p}{\partial\tilde{t}} = \frac{\partial\widetilde{E}_p}{\partial\tilde{\rho}}\frac{\partial\tilde{\rho}}{\partial\tilde{t}}. \tag{4.21}$$

Note the $\partial\widetilde{E}_p/\partial\tilde{\rho}$ is the opposite of the integral (4.18). Thus, for the hyperbolic tangent stratification studied here, $\partial\widetilde{E}_p/\partial\tilde{t}$ is

$$\frac{\partial\widetilde{E}_p}{\partial\tilde{t}} = \tilde{g}\tilde{\delta}_\rho \text{arctanh}\left(\frac{\tilde{\varrho}\tilde{\rho}}{\tilde{\varrho}^2 - \tilde{\bar{\rho}}\tilde{\rho} - \tilde{\bar{\rho}}^2}\right)\frac{\partial\tilde{\rho}}{\partial\tilde{t}}. \tag{4.22}$$

Substitution of the density trasoport equation (2.46c) into (4.22) yields:

$$\frac{\partial\widetilde{E}_p}{\partial\tilde{t}} = \tilde{g}\tilde{\delta}_\rho \text{arctanh}\left(\frac{\tilde{\varrho}\tilde{\rho}}{\tilde{\varrho}^2 - \tilde{\bar{\rho}}\tilde{\rho} - \tilde{\bar{\rho}}^2}\right)\left(-\tilde{\mathbf{v}}\cdot\widetilde{\nabla}\tilde{\rho} - \tilde{w}\frac{d\tilde{\bar{\rho}}(\tilde{z})}{d\tilde{z}} + \widetilde{D}\widetilde{\nabla}^2\tilde{\rho}\right), \tag{4.23}$$

where the material derivative in (2.46c) has been expanded, and the symbol $\widetilde{D}$ replaces $\tilde{\kappa}$ for the mass diffusivity.

Equation (4.23) can be written in shortened notation, similar to the kinetic energy equations (4.8) and (4.9):

$$\frac{\partial\widetilde{E}_p}{\partial\tilde{t}} = -\widetilde{T}_p + \widetilde{B} - \widetilde{\chi} \tag{4.24}$$

where

$$\begin{aligned}
\widetilde{T}_p &= -\tilde{g}\tilde{\delta}_\rho\left[\text{arctanh}\left(\frac{\tilde{\varrho}\tilde{\rho}}{\tilde{\varrho}^2 - \tilde{\bar{\rho}}\tilde{\rho} - \tilde{\bar{\rho}}^2}\right)\tilde{\mathbf{v}}\cdot\widetilde{\nabla}\tilde{\rho}\right] \\
\widetilde{B} &= -\tilde{g}\tilde{\delta}_\rho\left[\text{arctanh}\left(\frac{\tilde{\varrho}\tilde{\rho}}{\tilde{\varrho}^2 - \tilde{\bar{\rho}}\tilde{\rho} - \tilde{\bar{\rho}}^2}\right)\tilde{w}\frac{d\tilde{\bar{\rho}}(\tilde{z})}{d\tilde{z}}\right] \\
\widetilde{\chi} &= -\tilde{g}\tilde{\delta}_\rho\widetilde{D}\left[\text{arctanh}\left(\frac{\tilde{\varrho}\tilde{\rho}}{\tilde{\varrho}^2 - \tilde{\bar{\rho}}\tilde{\rho} - \tilde{\bar{\rho}}^2}\right)\widetilde{\nabla}^2\tilde{\rho}\right]
\end{aligned}$$

An interesting question that arises is how does (4.20) differ from the potential energy defined by (4.15). This can be seen by expanding (4.20) in a Taylor series of about $\tilde{\rho} = 0$. With some algebraic manipulation, the first 3 terms of the Taylor series can be shown to be:

$$\widetilde{E}_p = -\frac{1}{2}\frac{\tilde{g}}{\tilde{\rho}_0}\frac{1}{d\tilde{\bar{\rho}}(\tilde{z})/d\tilde{z}}\tilde{\rho}^2 - \frac{1}{3}\frac{\tilde{g}}{\tilde{\rho}_0}\frac{\tilde{\bar{\rho}}(\tilde{z})}{\tilde{\delta}_\rho\tilde{\varrho}(d\tilde{\bar{\rho}}(\tilde{z})/d\tilde{z})^2}\tilde{\rho}^3 - \frac{1}{12}\frac{\tilde{g}}{\tilde{\rho}_0}\frac{\tilde{\varrho} + 3\tilde{\bar{\rho}}(\tilde{z})}{\tilde{\varrho}\tilde{\delta}_\rho^2(d\tilde{\bar{\rho}}(\tilde{z})/d\tilde{z})^3}\tilde{\rho}^4 \tag{4.25}$$

In the limit of linearized motion (which is typically how (4.15) is derived), terms of order greater than $\tilde{\rho}^2$ are assumed small and neglected, reducing the above equation to (4.15).

Nondimensionalization Using the scaling outlined in §4.4.1 below, (4.24) can be written in nondimensional form as:

$$\frac{\partial E_P}{\partial t} = -T_P + B - \chi, \tag{4.26}$$

where

$$\begin{aligned}
E_P &= \left(\frac{2\pi}{\overline{\text{F}}_r}\right)^2\delta_\rho\left[(\bar{\rho}(z) + \rho)\text{arctanh}\left(\frac{\varrho\rho}{\varrho^2 - \bar{\rho}\rho - \bar{\rho}^2}\right) + \frac{\varrho}{2}\ln\left(\frac{\varrho^2 - (\bar{\rho}(z) - \rho)^2}{\varrho^2 - \bar{\rho}^2}\right)\right] \\
T_P &= \left(\frac{2\pi}{\overline{\text{F}}_r}\right)^2\delta_\rho\left[\text{arctanh}\left(\frac{\varrho\rho}{\varrho^2 - \bar{\rho}\rho - \bar{\rho}^2}\right)\mathbf{v}\cdot\nabla\rho\right] \\
B &= \left(\frac{2\pi}{\overline{\text{F}}_r}\right)^2\delta_\rho\left[\text{arctanh}\left(\frac{\varrho\rho}{\varrho^2 - \bar{\rho}\rho - \bar{\rho}^2}\right)w\frac{d\bar{\rho}(z)}{dz}\right] \\
\chi &= \left(\frac{2\pi}{\overline{\text{F}}_r}\right)^2\frac{1}{\text{Re}_\text{r}\text{Sc}}\left[\text{arctanh}\left(\frac{\varrho\rho}{\varrho^2 - \bar{\rho}\rho - \bar{\rho}^2}\right)\nabla^2\rho\right],
\end{aligned}$$

and Re_r, $\overline{\text{F}}_r$, Sc are defined in (4.28) below.

4.3 Numerical Considerations

Naturally, it is not sufficient to perform numerical simulations without first performing basic numerical checks for adequate spatial resolution, temporal resolution, and domain size. Spatial resolution includes both large and small scales. If the simulation is not spatially resolved, energy will not transfer to proper scales, usually resulting in an under-calculation of kinetic energy dissipation rate. Since the simulations use a spectral code, spatial resolution can be verified via an energy spectrum. If the simulation is not resolved temporally, each timestep will yield an inaccurate result, and this will affect the energy balance. As the simulations will be carried out with a variable timestepping technique, temporal resolution can be checked by integrating the left hand side of the kinetic and potential energy equations (4.8), (4.23). Finally, the vertical domain size may have an effect on the simulation. If the domain is too small, the boundaries may adversely affect the simulation. Each of these numerical considerations is examined below.

4.3.1 Small Scale Resolution

Small scale motions must be resolved in a DNS to properly simulate the dissipation rate of kinetic and potential energy. One method of verifying the resolution of the flow is by means of the kinetic energy dissipation rate (ε) spectrum. Since ε is a small scale process, a well resolved simulation will show the magnitude of the kinetic energy dissipation rate spectrum to increase with wavenumber (decreasing length scale), indicating ε is occurring at small scales. Since the flow is initialized with maximum energy on the center horizontal plane, this would be a good place to check the simulation resolution, as it is a likely place for the simulation to become under-resolved. Figure 4.2 contains a plot of the (nondimensional) kinetic energy dissipation rate spectrum of the center plane at $t = 10$, with $\overline{\mathrm{F}}_r = 2.75$, $\mathrm{Re_r} = 19200$, $\xi = 0.01$, which is representative of all vortex street simulations performed in this study. In Figure 4.2, ε increases with wavenumber up to $k_x = 112$, where the anti-aliasing filter causes a sudden drop in magnitude. This result suggests that the simulation is well-resolved. Several other horizontal planes (including planes of maximum shear seen in Figure 4.11) were examined with similar results.

4.3.2 Temporal Resolution

Within the Boussinesq approximation, the mechanical energy equation and momentum equations are not independent. Since the momentum equations are numerically integrated, the energy equations can provide a check of the temporal resolution. In order to verify temporal resolution, the left hand side of the volume averaged kinetic and and potential energy equations (eqs. (4.6), (4.23)) are integrated in time using the trapezoid rule and compared to the directly computed energy values. Figure 4.3 (a) contains plots of the integrated kinetic energy equation vs. calculated energy for simulation $\xi = 0.01$, $\overline{\mathrm{F}}_r = 2.75$, $\mathrm{Re_r} = 19200$, while Figure 4.3(b) contains a plot of the relative error between the two. The same quantities for potential energy are shown in Figures 4.4 (a), (b). In each plot, there is good agreement between the calculated and integrated energy values. Early in each simulation, the relative error is $\approx 10^{-3}$. The relative error is seen to increase in time, and can be explained by noting that as each term in integrated, the cumulative error will increase, which will gradually increase the relative error. In addition, data was available in ≈ 0.25 nondimensional time units, which is a large timestep to be integrating over.

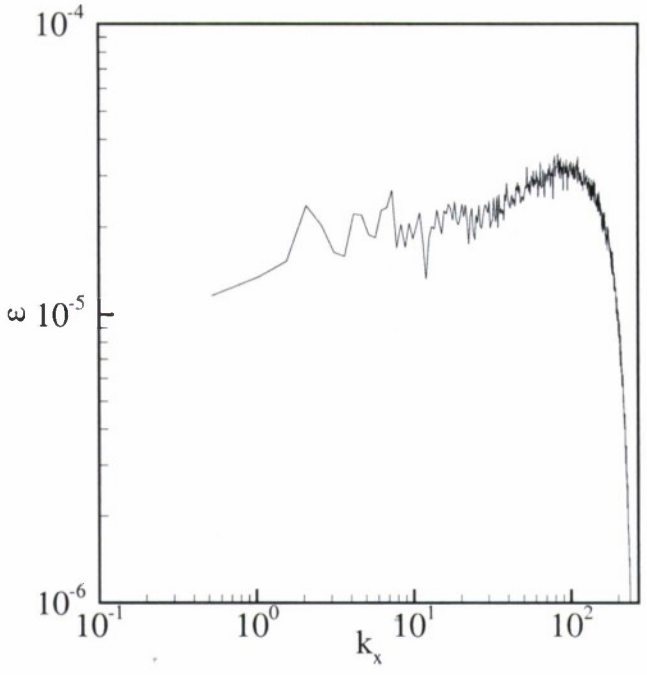

Figure 4.2: (nondimensional) x direction kinetic energy dissipation rate spectrum (ε_{11}) for the center plane of $\xi = 0.01$, $\mathrm{F_r} = 2.75, \mathrm{Re_r} = 19200$.

Also, the integration was performed with a first order trapezoid method for convenience, as opposed to a more accurate interation method like 3rd order Adams Bashforth. When the simulation was run for 7 consecutive timesteps, the relative error between the integrated and actual energy values is $\approx 10^{-5}$ (Figure 4.5). Again, the increase in error is due to the cumulative error added for each timestep integration. These results suggest that the simulation is temporally resolved.

4.3.3 Vertical Domain Size

When analyzing stratified flows, the behavior of vertical motions is a topic of interest. As such, it is important to consider the effect of the vertical domain size on the simulated flows. Since the simulations are run with periodic boundary conditions, it is similar to having an identical flow domain at each boundary. Thus, flows that occur at one edge of the domain can affect the flows at the opposite boundary. The effect of this interaction can be seen in Figure 4.6, which contains plots of the horizontal (xy) planar averaged horizontal and vertical kinetic energies (E_H, E_V) at $t = 10$ for simulations with nondimensional computational domain height $L_z = \tilde{L}_z/\tilde{r}_m = \pm 1.5$ and ± 3. Note that E_H is similar for each simulation except for the vertical boundaries, where the energy increases at the boundary for $L_z = \pm 1.5$ as opposed to when $L_z = \pm 3$. In the vertical kinetic energy plot, a large double peak exists above and below the centerline with $L_z = \pm 1.5$, but decreases significantly in magnitude with $L_z = \pm 3$. Also, an internal wave can be seen in E_V (and to a lesser extent in E_H) that extends to the boundary with $L_z = \pm 3$, but does not exist with the smaller domain height. Support for internal wave formation can be seen in Figure 4.18 which is consistent with the fact that internal waves can not exist when there is no stratification. The differences in L_z can be attributed to the periodic boundary condition, where for the

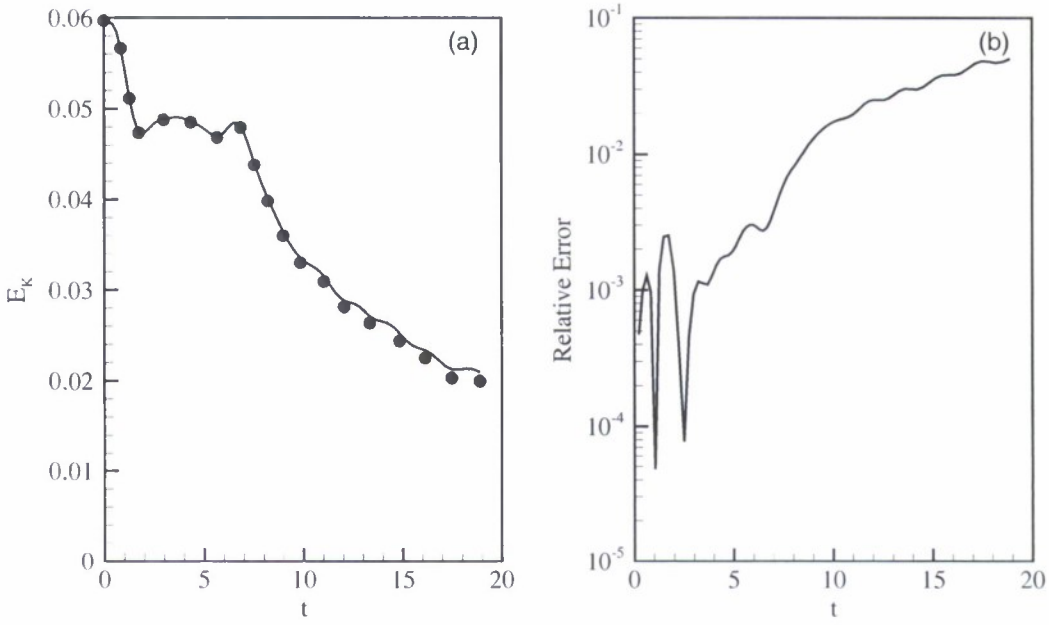

Figure 4.3: Kinetic energy equation balance (left) and relative error between integrated and directly computed kinetic energy (right). (•) represents the value of energy at a particular time, (-) is the time integration of the right hand side of (4.6). Here $F_r = 2.75$, $Re_r = 19200$, $\xi = 0.01$.

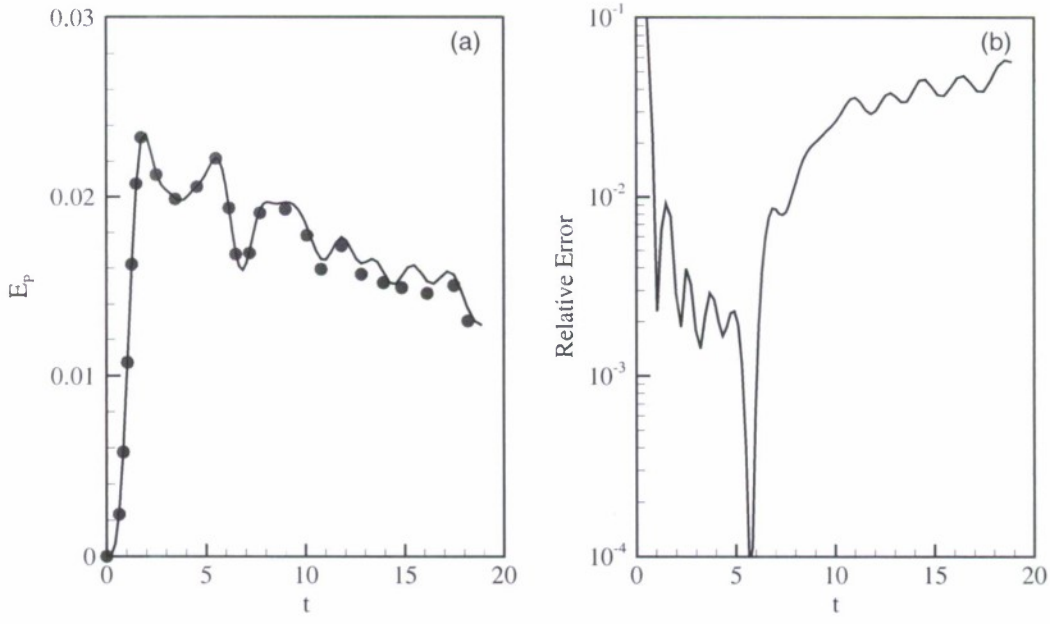

Figure 4.4: Potential energy equation balance (left) and relative error between integrated and directly computed potential energy (right). (•) represent the value of energy at a particular time, (-) is the time integration of the right hand side of (4.23). Here $F_r = 2.75$, $Re_r = 19200$, $\xi = 0.01$.

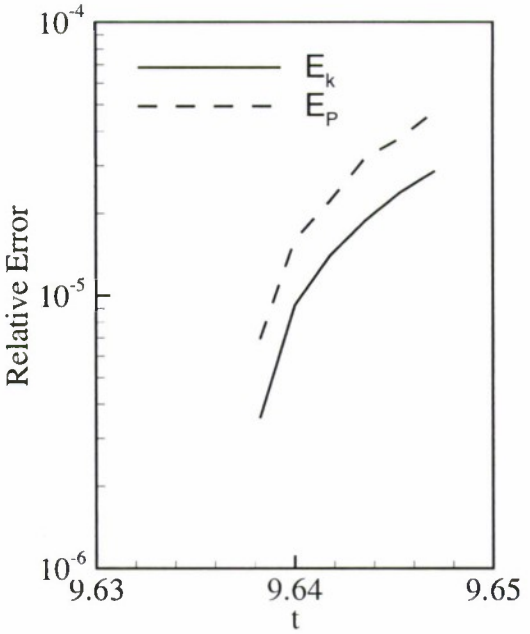

Figure 4.5: Relative error between integrated and computed kinetie and potential energies for 7 consecutive timesteps, simulation $\mathrm{F_r} = 2.75$, $\mathrm{Re_r} = 19200$, $\xi = 0.01$.

smaller L_z the wave interacts more strongly at the boundaries than the larger L_z. For all simulations L_z was chosen to be ± 3 to minimize the interaetion between boundaries.

4.4 Methodology

4.4.1 Equations of Motion

The numerieal method used in the vortex street simulations is the same as the Taylor-Green simulations in Chapter 3. Speeifieally, the fields are assumed to satisfy the Navier-Stokes equations subject to the Boussinesq approximation (§2.1.5), and are solved using a pseudo-speetral technique with periodic boundary conditions and the pressure-projeetion method. Taking $\tilde{\mathcal{U}}$ as the velocity scale, $\tilde{r}_m$ as a length scale, $\tilde{r}_m|\Delta\tilde{\bar{\rho}}/\Delta\tilde{z}|$ as a density scale (where $|\cdot|$ denotes absolute value), $\tilde{r}_m/\tilde{\mathcal{U}}$ as a time scale, and $\tilde{\rho}_0\tilde{\mathcal{U}}^2$ as a pressure scale (where $\tilde{\rho}_0$ is the referenee density value), the nondimensional governing equations in a non-rotating frame of referenee are:

$$\nabla \cdot \mathbf{v} = 0 \tag{4.27a}$$

$$\frac{\partial \mathbf{v}}{\partial t} + \mathbf{v} \cdot \nabla \mathbf{v} = -\left(\frac{2\pi}{\mathrm{F}_r}\right)^2 \rho \mathbf{e}_z - \nabla p + \frac{1}{\mathrm{Re_r}} \nabla^2 \mathbf{v} \tag{4.27b}$$

$$\frac{\partial \rho}{\partial t} + \mathbf{v} \cdot \nabla \rho - w \frac{d\bar{\rho}(z)}{dz} = \frac{1}{\mathrm{Re_r Sc}} \nabla^2 \rho \tag{4.27e}$$

where $\mathbf{v} = (u, v, w)$ is the velocity vector, and ρ and p are the (nondimensional) density and pressure deviations from their ambient values, and $\mathbf{e}_z$ is a unit veetor in the vertieal

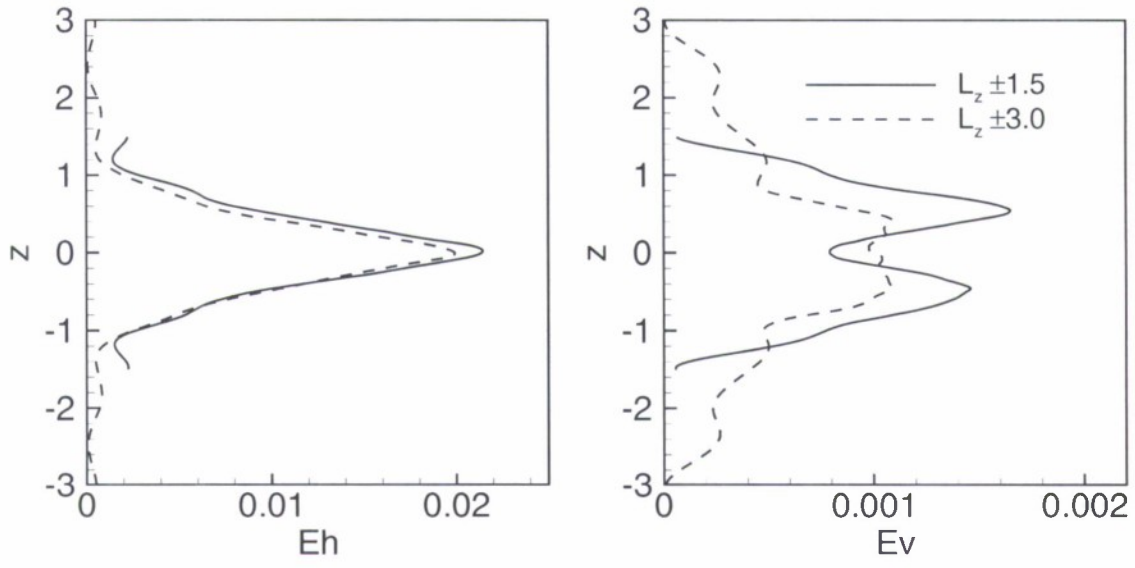

Figure 4.6: Comparison of horizonal planar averaged horizontal (left) and vertical (right) kinetic energy with $L_z = \pm 1.5$ and ± 3, $t = 10$. Here $\overline{\mathrm{F}}_r = 2.75$, $\mathrm{Re_r} = 19200$, $\xi = 0.01$.

direction. The Reynolds, Froude, and Schmidt numbers are defined as:

$$\mathrm{Re_r} = \frac{\widetilde{\mathcal{U}}\tilde{r}_m}{\tilde{\nu}} \qquad \overline{\mathrm{F}}_r = \frac{2\pi\widetilde{\mathcal{U}}}{\widetilde{\overline{\mathrm{N}}}\tilde{r}_m} \qquad \mathrm{Sc} = \frac{\tilde{\nu}}{\widetilde{\mathcal{D}}}. \tag{4.28}$$

where $\widetilde{\overline{\mathrm{N}}}^2 = -\tilde{g}/\tilde{\rho}_0(\Delta\tilde{\bar{\rho}}/\Delta\tilde{z})$ is the average buoyancy (or Brunt-Väisälä) frequency, and $\widetilde{\mathcal{D}}$ is an "effective" mass diffusivity, representing the combined effects of thermal diffusivity and either salt diffusivity (ocean) or water vapor diffusivity (atmosphere).

In all vortex street simulations, $\overline{\mathrm{F}}_r = 2.75$ and $\mathrm{Re_r} = 19200$. In addition, Sc was set to 1, close to the ratio of momentum to heat diffusivity in air ($\mathrm{Sc}_{air} = 0.7$), but far from the oceanic Schmidt numbers for temperature ($\mathrm{Sc_T} = 7$) and salinity ($\mathrm{Sc_S} = 700$). Also, note the only difference between (4.27) and (3.2) is the allowance of the density stratification $d\bar{\rho}(z)/dz$ to be a function of vertical height, rather than a constant.

4.4.2 Momentum vs. Density Vertical Scales

The vertical profile of both the velocity (4.1) and density stratification (4.3) are sech^2, with different vertical scales $\tilde{\delta}_{\mathcal{U}}$ and $\tilde{\delta}_\rho$. The parameter ξ is now defined which describes the ratio of the wake to density vertical length scales:

$$\xi = \frac{\tilde{\delta}_{\mathcal{U}}}{\tilde{\delta}_\rho}. \tag{4.29}$$

In each simulation, $\tilde{\delta}_{\mathcal{U}}$ remains fixed, while $\tilde{\delta}_\rho$ is altered. Simulations were performed with ξ ranging from 0.01 (nearly uniform density stratification) to 4 (sharp density step). The vertical density stratification profiles with several ξ's are shown in Figure 4.7. Note that while locally $d\bar{\rho}(z)/dz$ differs for each ξ, the average (nondimensional) change in density with height $\Delta\bar{\rho}/\Delta z = -1$ is the same.

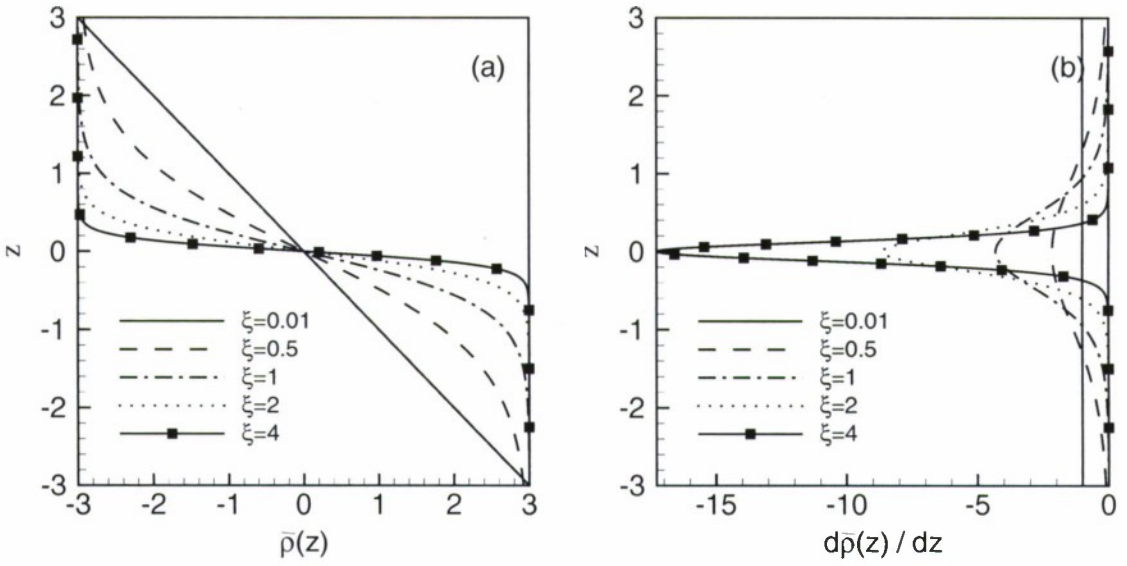

Figure 4.7: (a) Ambient (nondimensional) density profile and (b) stratification profile for each ξ. Note $\Delta\bar{\rho}/\Delta z = -1$ for each ξ, but locally $d\bar{\rho}(z)/dz$ is different.

Notation	ξ	δ_ρ	$\delta_\mathcal{U}$	F_r	$\mathrm{Re_r}$	L_x	L_y	L_z	N_x	N_y	N_z
F2.75R24	0.01	69.4	0.694	2.75	2400	12	6	6	512	256	256
F2.75R48	0.01	69.4	0.694	2.75	4800	12	6	6	512	256	256
F2.75R192	0.01	69.4	0.694	2.75	19200	12	6	6	1024	512	512
$\xi = 0.01$	Same as F2.75R192										
$\xi = 0.5$	0.5	1.39	0.694	2.75	19200	12	6	6	1024	512	512
$\xi = 1$	1	0.694	0.694	2.75	19200	12	6	6	1024	512	512
$\xi = 2$	2	0.347	0.694	2.75	19200	12	6	6	1024	512	512
$\xi = 4$	4	0.174	0.694	2.75	19200	12	6	6	1024	512	512
No Strat	N/A	N/A	0.694	∞	19200	12	6	6	1024	512	512

Table 4.1: List of vortex street simulations

4.5 Simulation Results

In this section results are presented for vortex street simulations. Comparisons will be made with different $\mathrm{Re_r}$ for $\xi = 0.01$ (yielding a near uniform density stratification, see 4.7) as well as for all ξ simulations, with $\mathrm{F}_r = 2.75$ and $\mathrm{Re_r} = 19200$. Table 4.1 contains a list of the vortex simulations performed, including Froude and Reynolds number as defined in (4.28), domain size, and number of grid points N_x, N_y, N_z in the x, y, and z directions. General flow characteristics are first presented followed by flow energetics and finally quantities of interest such as buoyancy Reynolds number and mixing efficiency.

4.5.1 General Flow Characteristics

In order to gain insight into the general flow dynamics, a time-series plot of the center plane streamfunction ψ as defined in Riley and de Bruyn Kops [2003] is shown in Figure 4.8 for

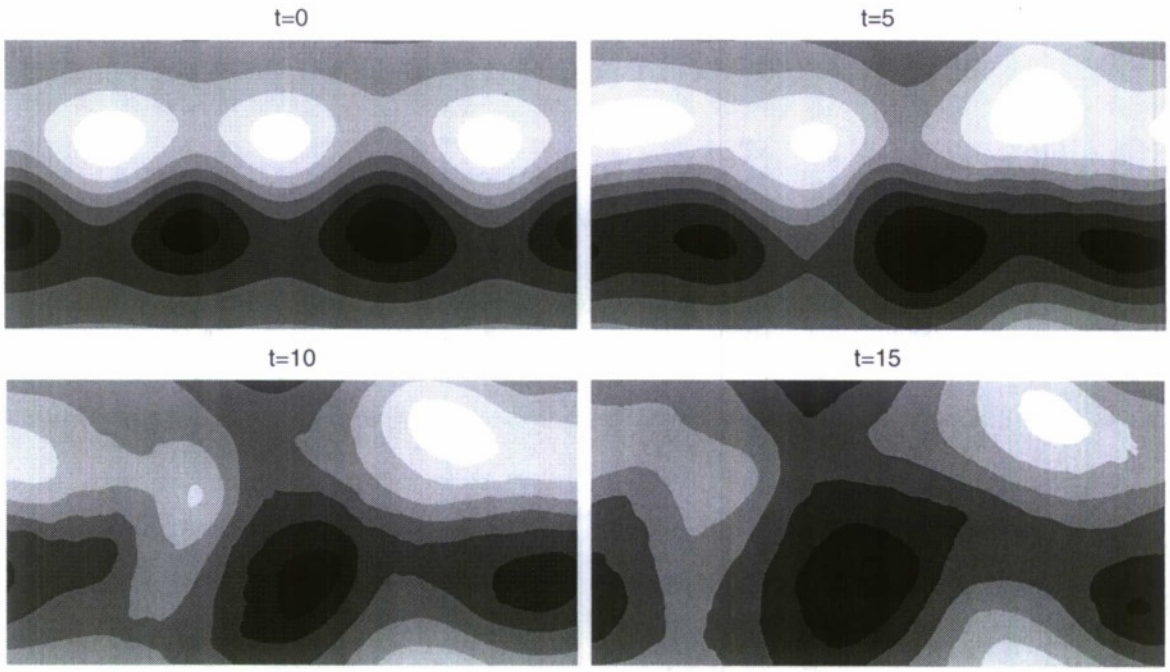

Figure 4.8: Contour plot of center plane stream function ψ for F2.75R192, ξ=0.01. Light colors represent positive values of ψ, dark colors represent negative values.

the simulation $\xi = 0.01$, where light colors represent positive vortices, dark colors represent negative vortices. Cases having other ξ values demonstrate qualitatively similar results. The von Kármán vortex street is clear at $t = 0$. As the simulated flow evolves, the vortices interact with each other, and vortex pairing occurs by $t = 15$.

As the flow evolves, vertical velocity (w) is generated due to internal waves and turbulence formation. Since the flow was initialized with no vertical velocity, w can be used as an indicator of turbulence generation. Figure 4.9 contains plots of the center plane ($z = 0$) vertical velocity at several different times for simulation F2.75R192. At $t = 5$ a "herring bone" pattern of vertical velocity forms where there is large shear between vortices. The vertical velocity increases in time, reaching a at maximum approximately $t = 10$ before decaying.

In density stratified flows it is well known that turbulence forms in intermittent, localized patches. Figure 4.10 contains plots of center plane vertical velocity at $t = 10$ for simulations $\xi = 0.01$ (left plot) and No Strat (right plot). Simulation $\xi = 0.01$ is representative of all stratified simulations, where intermittent turbulent patches form, which is consistent with prior studies regarding density stratified flows. In contrast, vertical velocity is shown to be distributed throughout the plane for the No Strat simulation. This results suggests the stratified simulations are representative of flows observed in laboratory and natural settings.

Shear and Richardson Number

In stratified flows dominated by vortical modes (such as those simulated in this study), it is postulated that horizontal layer decoupling occurs, and the flow will be susceptible to Kelvin-Helmholtz shear instabilities [Lilly, 1983]. The square of the vertical shear of

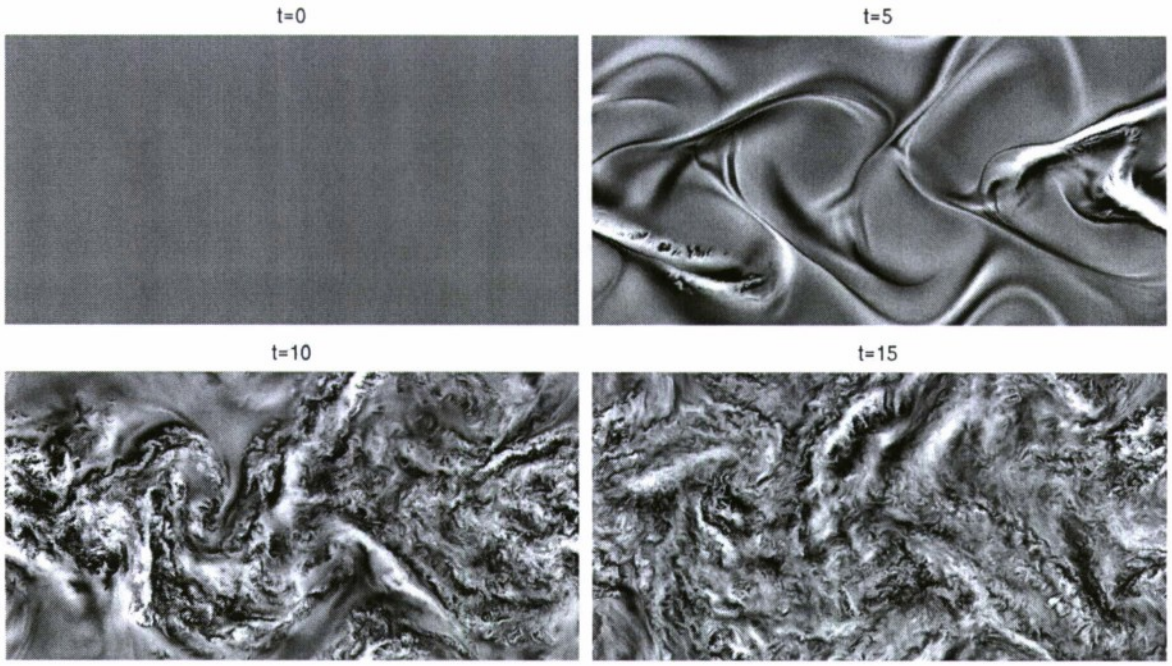

Figure 4.9: Center plane ($z = 0$) vertical velocity for the same times as in Figure 4.8. All figures have the same colormap scaling. Dark colors represent negative (downward) velocity, light colors represents positive velocity.

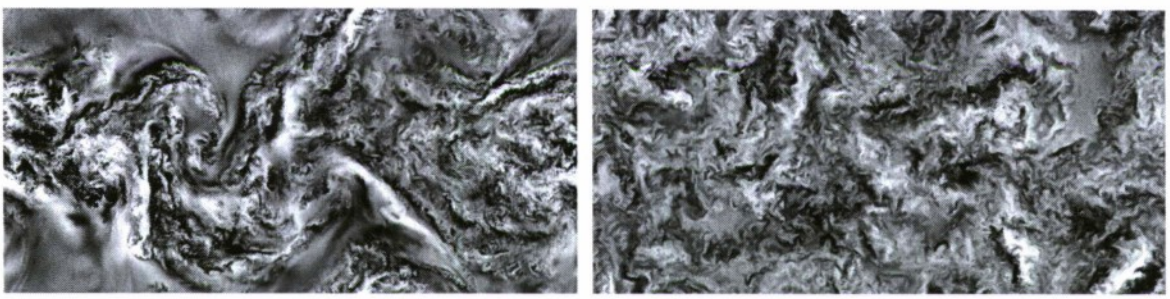

Figure 4.10: Center plane ($z = 0$) vertical velocity for $\xi = 0.01$ (left plot) and no stratification (right plot). Dark colors represent negative (downward) velocity, light colors represent positive velocity.

horizontal motions is defined as:

$$S^2 = \left(\frac{\partial u}{\partial z}\right)^2 + \left(\frac{\partial v}{\partial z}\right)^2 \tag{4.30}$$

Figure 4.11 contains time evolution plots of the horizontally averaged square of vertical shear $\langle S^2 \rangle_H$ vs. vertical position for several ξ and non-stratified simulations, where $\langle \cdot \rangle_H$ denotes horizontal (xy) planar averaging. Initially, the shear profile demonstrates a "bimodal" pattern with maximum values at $z \pm 0.5$, a result of the initial $\mathrm{sech}^2(z)$ velocity profile (note that the initial vertical shear magnitude is very small). The bimodal shear pattern persists in time for all the stratified cases, which can be attributed to decoupling of horizontal layers in stratified flows suggested by Lilly [1983]. In contrast, the bimodal pattern disappears by $t = 5$ for the non-stratified case, where decoupling does not occur. It is interesting to note that the magnitude of $\langle S^2 \rangle_H$ increases as ξ is increased. This is due to the increase in local density stratification with ξ (Figure 4.7), which in turn causes stronger horizontal layer decoupling and an increase in the vertical shear between layers. Also, when $\xi = 4$ the maximum $\langle S^2 \rangle_H$ occurs much earlier in time than for other values of ξ. This is caused by a rapid increase in shear at the intersection of the unstratified flow regime outside the density stratification layer with the strongly stratified regime. That is, for $\xi = 4$ a significant amount of $\langle S^2 \rangle_H$ occurs where there is no density stratification ($|z| > 0.75$), resulting in the creation of vertical overturning in this area, seen in the planar averaged vertical kinetic energy $\langle E_V \rangle_H$ (Figure 4.18(e) below). The density stratification then acts as a boundary between the overturning flow outside the stratification and the horizontal flow inside, resulting in a larger amount of shear to be generated.

A quantity related to vertical shear of horizontal motions is the gradient Richardson number Ri, defined as the ratio of buoyancy to shear forces. The volume and planar averaged Ri are defined here as:

$$\langle \mathrm{Ri} \rangle = \left(\frac{2\pi}{\overline{\mathrm{F}}_r}\right)^2 \frac{1}{\langle S^2 \rangle} \tag{4.31}$$

$$\langle \mathrm{Ri} \rangle_H = \left(\frac{2\pi}{\overline{\mathrm{F}}_r}\right)^2 \frac{d\bar{\rho}(z)/dz}{\langle S^2 \rangle_H} \tag{4.32}$$

where $\langle \cdot \rangle$ denotes volume averaged quantity. $\langle \mathrm{Ri} \rangle$ is shown in Figure 4.12(a). Initially $\langle \mathrm{Ri} \rangle$ is large, indicating that there is insufficient shear to cause instabilities and turbulence. Then, as the flow progresses in time, $\langle \mathrm{Ri} \rangle$ rapidly decreases due to vertical decoupling of the horizontal motions. $\langle \mathrm{Ri} \rangle$ decreases to about 0.25, supporting the notion that Kelvin-Helmholtz instabilities are a mechanism by which turbulence occurs. Further examination of the planar averaged Richardson number $\langle \mathrm{Ri} \rangle_H$ (Figure 4.12(b)) shows that for all values of ξ, $\langle \mathrm{Ri} \rangle_H$ is significantly less than 0.25 for planes near the center of the wake, suggesting it is here where Kelvin-Helmholtz instabilities are begin generated.

From Figure 4.12, it is apparent that the evolution of $\langle \mathrm{Ri} \rangle$ and the profiles of $\langle \mathrm{Ri} \rangle_H$ depend strongly on ξ. When $\xi \leq 1$, all but the tails of the wake are strongly stratified and the stratification in the center of the wake is stronger for higher values of ξ. The flows with $\xi \leq 1$ behave as expected based on similar simulations in uniformly stratified turbulence Riley and de Bruyn Kops [2003]. In particular, the development of the flow is qualitatively independent of the strength of the stratification in the core of the wake, but the time for decoupling of the horizontal motions to occur and $\langle \mathrm{Ri} \rangle$ to reach its minimum value increases slightly with increased stratification. When $\xi > 1$, however, the wake profile is wider than

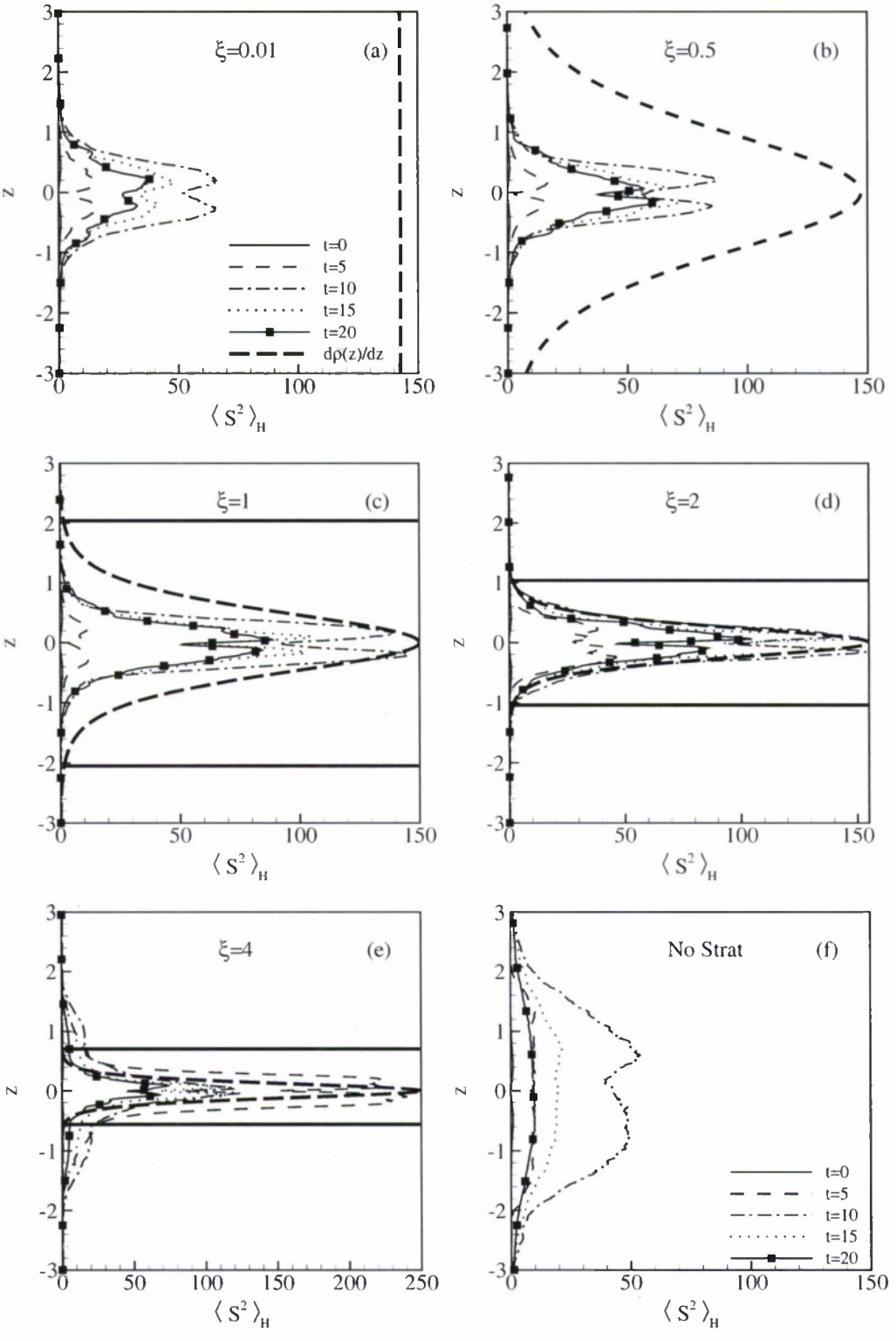

Figure 4.11: Time evolution of vertical shear of horizontal motion $\langle S^2 \rangle_H$ for all ξ and no stratification. Note the difference in horizontal scale for plot (e). $d\bar{\rho}(z)/dz$ is shown as bold dashed line, and is scaled differently in each figure for comparison to $\langle S^2 \rangle_H$. Bold horizontal lines mark where $d\bar{\rho}(z)/dz = -0.01$. Since the entire vertical domain satisfies this criterion for plots (a)-(b), no bold horizontal lines are shown.

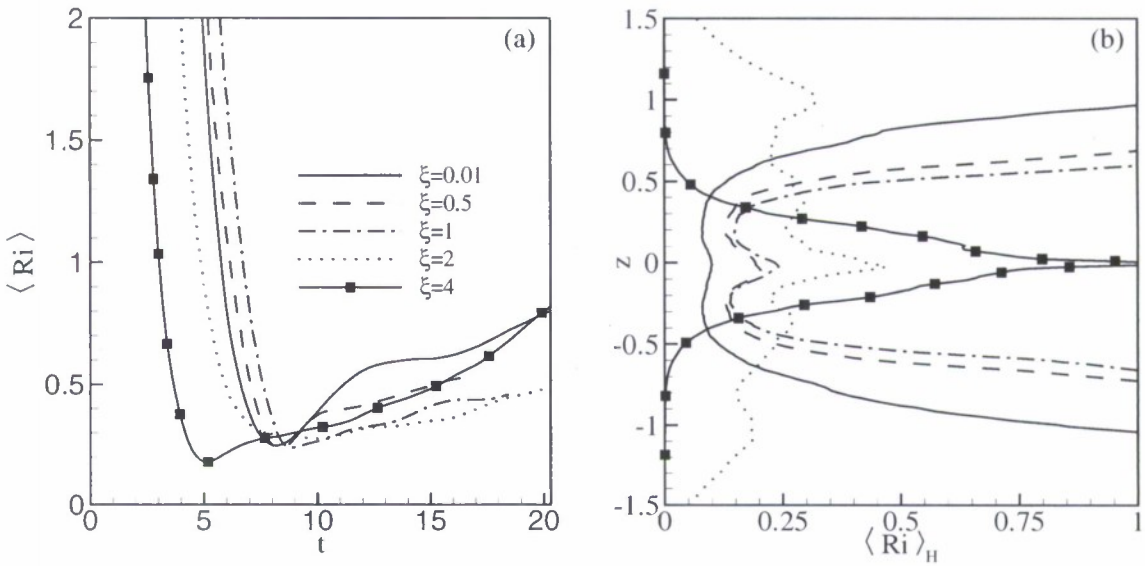

Figure 4.12: (a) $\langle \mathrm{Ri} \rangle$ vs. time, (b) Vertical profile of $\langle \mathrm{Ri} \rangle_H$ vs. height at $t = 10$. Note that all simulations begin with $\langle \mathrm{Ri} \rangle = 25$. Also note the profiles of Ri with $\xi \geq 2$ are fundamentally different from those with $\xi < 2$.

the stratification profile and the regions initialized with the highest shear are not strongly constrained in the vertical direction by gravity, resulting in earlier less inhibited formation of shear.

For the simulations with $\xi \leq 1$, the minimum $\langle \mathrm{Ri} \rangle_H$ is located near $z = 0$, as all the wake is inside the density stratification layer. In contrast, when $\xi > 1$, some of the wake is now outside the stratification layer, and minimum $\langle \mathrm{Ri} \rangle_H$ occurs at $|z| > 1.5$. This behavior of Ri helps explain the large vertical kinetic energy shown in Figure 4.18 below, particularly for $\xi = 4$.

Horizontal Length Scale

Flows subject to stable density stratification often demonstrate an increasing horizontal length scale. This quality is evident in the evolution of the center plane streamfunction (ψ), shown in Figure 4.8. Theoretical arguments suggest that a horizontal length based on an advective time scale $\ell_H \sim u_H^3/\varepsilon$ can be calculated. However, in flows that demonstrate intermittent turbulence, use of such an advective length scale can result in unrealistic values of ℓ_H (see §3.4.3). Instead, a horizontal length scale is defined here based on the cross-correlation of velocity:

$$R_{yx}(r) = \frac{\langle v(x+r)v(x) \rangle_H}{\langle v^2 \rangle_H} \tag{4.33}$$

where the R_{yx} denotes the correlation of y direction velocity (v) in the x direction. The horizontal length scale is then defined as the distance r when $R_{yx} = 0$:

$$\ell_H = r, \quad \text{where } R_{yx}(r) = 0 \tag{4.34}$$

Figure 4.13 contains a plot of ℓ_H for all ξ after $t = 5$, when the response to the flow initial condition has minimized. Although somewhat noisy, ℓ_H increases in time and is

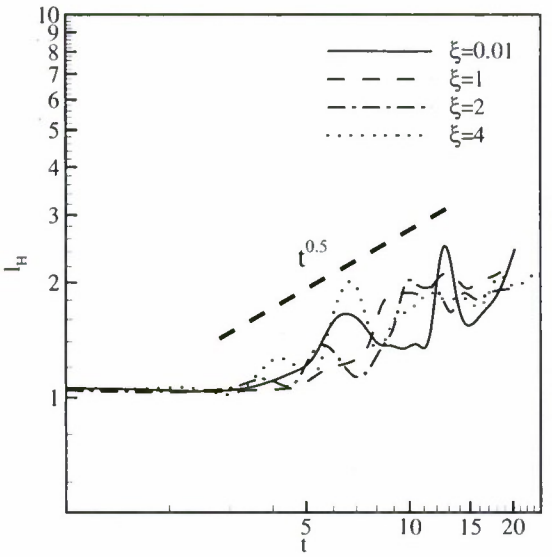

Figure 4.13: ℓ_H evolution for several ξ. Note the horizontal axis begins at $t = 5$, when the response to the initial condition has diminished.

proportional to $t^{0.5}$. This value is in agreement with the integral length scale results of Praud et al. [2005] and the experimental dipole results of Voropayev and Afanasyev [1992].

4.5.2 Energetics

Kinetic Energy

A general idea of the flow energetics can be seen by examination of the x direction spectrum of horizontal energy $\widehat{E}_h(k_x)$, defined as:

$$\widehat{E}_H(k_x) = \frac{1}{2}\left(\widehat{u}(k_x)\widehat{u}(k_x)^* + \widehat{v}(k_x)\widehat{v}(k_x)^*\right) .$$

Here $\widehat{(\cdot)}$ signifies x-direction Fourier space, $(\cdot)^*$ denotes complex conjugate, and k_x denotes x-direction wavenumber. The left plot of Figure 4.14(a) contains a plot of $\hat{E}_H(k_x)$ for several different $\mathrm{Re_r}$ at $t = 20$. The initial peak at $k_x \approx \pi/2$ corresponds to the separation distance between vortices. The large scale spectra is identical for all $\mathrm{Re_r}$, which is typical of nearly inviscid large scale motions. In contrast, the small-scale motions (large k_x) are shown to increase monotonically with $\mathrm{Re_r}$, consistent with the ability of the flow to generate small-scale instabilities with increasing $\mathrm{Re_r}$.

A time evolution of $\hat{E}_H(k_x)$ for $\mathrm{F_r} = 2.75, \mathrm{Re_r} = 19200$ is shown in the right plot of Figure 4.14(b). As the flow evolves, small scale motions are generated causing the magnitude of $\hat{E}_H(k_x)$ at high wavenumbers to increase between $t = 0$ and $t = 10$. This is consistent with the increase in $\langle S^2 \rangle_H$ shown in Figure 4.11. In addition, once the flow has become turbulent (after $t = 10$), it displays a near $k_x^{-5/3}$ spectrum. This $k_x^{-5/3}$ dependence is seen for all ξ (Figure 4.15), and is in agreement with the energy spectra results of Lindborg [2006], who also found a $k^{-5/3}$ slope for horizontal spectra of horizontal energy. After $t = 10$ the energy at all wavenumbers decreases as the flow decays.

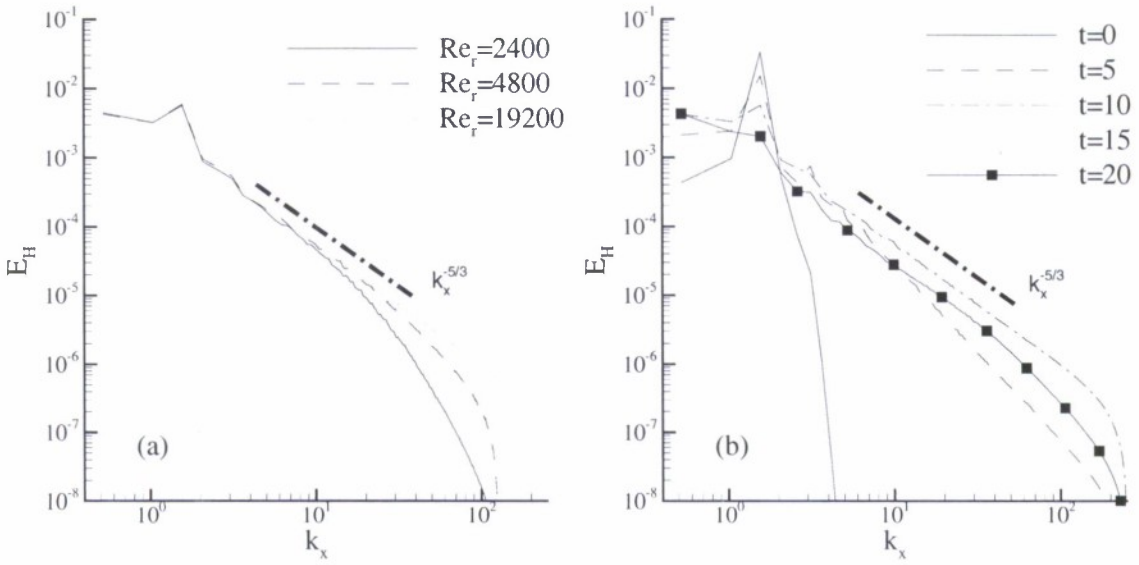

Figure 4.14: (a) E_H x spectra for several $\mathrm{Re_r}$ at $t = 10$; (b) Time evolution of E_H x spectra for $\mathrm{F_r} = 2.75$, $\mathrm{Re_r} = 19200$. Note $\xi = 0.01$ for both plots. The bold dashed-dotted line represents $k_x^{-5/3}$.

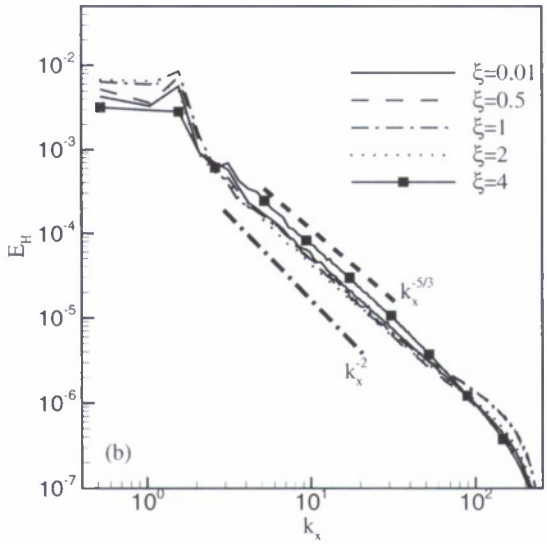

Figure 4.15: E_H x spectrum for all ξ, $t = 10$. The bold dashed line represents $k^{-5/3}$. The bold dashed-dotted line represents k_x^{-2}.

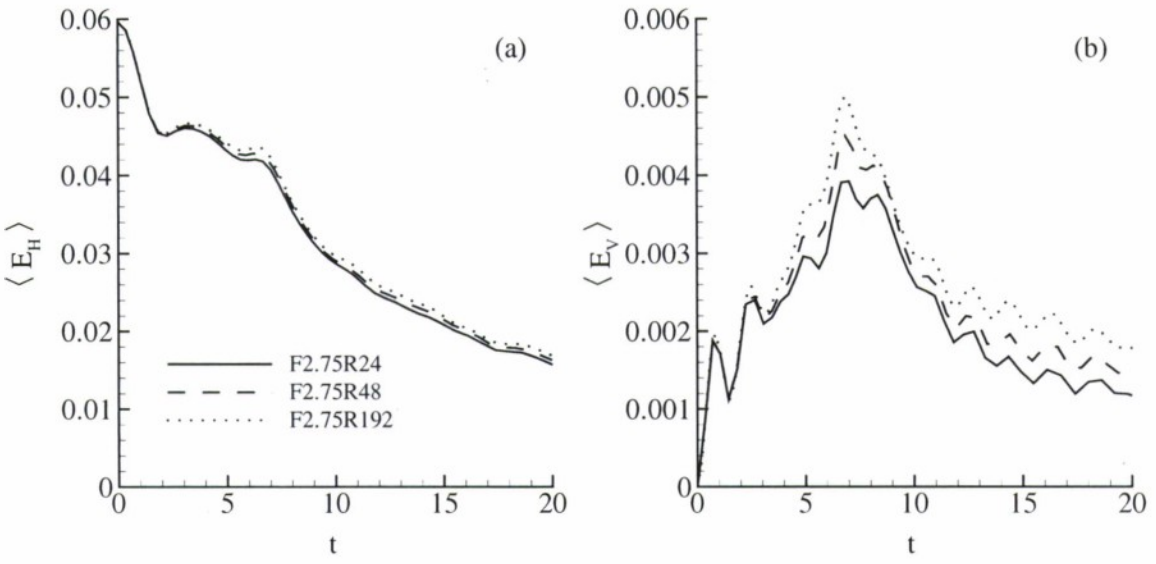

Figure 4.16: Time evolution of (a) $\langle E_H \rangle$ and (b) $\langle E_V \rangle$ for several $\mathrm{Re_r}$, $\overline{\mathrm{F}}_r = 2.75$, $\xi = 0.01$.

Figures 4.16 (a) and (b) contain plots of the time evolution of $\langle E_H \rangle$ and $\langle E_V \rangle$ for several $\mathrm{Re_r}$ and $\xi = 0.01$. $\langle E_H \rangle$ is shown to be relatively independent of $\mathrm{Re_r}$. In contrast, the maximum $\langle E_V \rangle$ is directly related to $\mathrm{Re_r}$, a likely result of the increased ability for vertical motion to overcome the stratification as $\mathrm{Re_r}$ is increased. Since the initial vertical velocity (w) and fluctuating density (ρ) are set to zero, the flow is not in cyclostrophic balance. As a result, a large internal wave immediately forms, which results in an oscillation in both $\langle E_H \rangle$ and $\langle E_V \rangle$.

The time evolution of $\langle E_H \rangle$ and $\langle E_V \rangle$ for each ξ is shown in Figures 4.17(a), (b). As ξ is increased from 0.01 to 2, the trend is for $\langle E_H \rangle$ to persist longer in time and the magnitude of $\langle E_V \rangle$ to decrease, compared with the unstratified flow. These trends are expected, since more work is required to overcome the stronger vertical stratification in the vortex "core." However, these trends are reversed when $\xi > 2$, and the flow begins to demonstrate traits similar to non-stratified flow. This is because the characteristic height of the wake is much smaller than the density stratification height, and a significant portion of the wake flow occurs in regions that have very weak density stratification. It is interesting that the transition occurs when $\xi > 2$, rather than $\xi > 1$, suggesting that it is the energy profile, rather than the velocity profile, that determines when the effect of stratification is minimized. Thus, for the simulations with $\xi \leq 2$, the stratification acts as a boundary to confine $\langle E_V \rangle_H$. In contrast, when $\xi = 4$ a significant amount of $\langle E_V \rangle_H$ forms in regions outside the density stratification layer where there is no buoyancy force and overturning can readily occur. This can be seen in Figure 4.18, where $\langle E_V \rangle_H$ is plotted vs. z for each ξ and no stratification.

T_H and T_V are the advection (or transport) terms that describe how E_H and E_V are advected throughout the flow. By definition, a simulated flow with periodic boundary conditions will have zero advection on average, since any transport out of one boundary will be transported into the opposite boundary. Hence $\langle T_H \rangle$ and $\langle T_V \rangle$ are zero, and are not shown here.

The time evolution of $\langle T_H \rangle_H$ for $\xi = 0.01$ and $\xi = 4$ are shown in Figures 4.19(a),

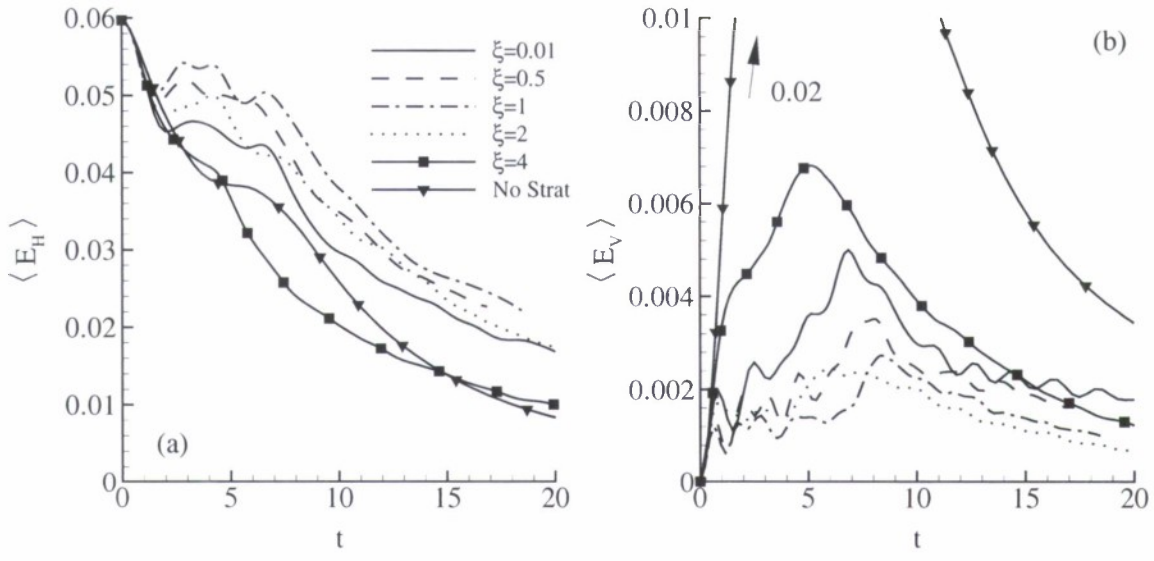

Figure 4.17: Time evolution of (a) $\langle E_H \rangle$ and (b) $\langle E_V \rangle$ for all ξ.

(b). For $\xi = 0.01$, early in the simulation when turbulence is forming (at $t = 5$) there is significant advection of E_H into the center planes from the adjoining ones (recall that it is negative $\langle T_H \rangle_H$ in (4.12)). Advection of energy into the center planes is counter-intuitive, as one would expect energy to be advected from the maximum energy planes to minimum energy planes. This can be explained by noting that the planes of positive $\langle T_H \rangle_H$ ($z \pm 0.5$) are also planes of $\langle S^2 \rangle_H$. Since planes of maximum $\langle S^2 \rangle_H$ will generate a large amount of vertical motion (through shear instabilities), energy will be advected out of the planes of high shear into the lower shear center plane. $\langle T_H \rangle_H$ most diminishes by $t = 10$.

The time evolution of $\langle T_V \rangle_H$ for $\xi = 0.01$ and $\xi = 4$ are shown in Figures 4.20(a), (b). Similar to $\langle T_H \rangle_H$, there is a large amount of $\langle T_V \rangle_H$ early in the flow. However, E_V is advected out of the center planes into the adjoining planes, in contrast to the inward advection of E_H. The reason for this early transport out of the center of E_V is unclear. Perhaps since vertical overturning is originating at the planes of maximum shear, eddies will cause a net advection of $\langle E_V \rangle_H$ out of the center planes.

P_H and P_V are pressure work terms that describe how pressure gradients affect the flow energetics. When the dot product of velocity and the pressure gradient taken, the result is a pressure work term that affects the evolution of energy. For example, a pressure gradient in the direction of the flow increases energy, while flow opposite a pressure gradient expends energy. Volume averaged $\langle P_H \rangle$ and $\langle P_V \rangle$ for several $\mathrm{Re_r}$ and $\xi = 0.01$ are shown in Figures 4.21(a), (b). Initially large pressure work is induced as a result of internal wave generation from the initial cyclostrophic imbalance. This early pressure work results in an initial loss of E_H and gain in E_V. Since $\langle P_V \rangle$ is initially negative, when substituted into (4.13), it will cause an increase in E_V. The opposite is true for $\langle P_H \rangle$ and $\langle E_H \rangle$. Note that for a closed system the pressure can do no net work, so that the total pressure work term $\langle P \rangle = \langle P_H \rangle + \langle P_V \rangle$ is zero. It is interesting that the magnitudes of $\langle P_H \rangle$ and $\langle P_V \rangle$ are nearly identical for each $\mathrm{Re_r}$, suggesting internal wave motion is controlled by large scale dynamics.

Figure 4.22(a) contains a plot of $\langle P_H \rangle$ vs. time for each ξ. Figure 4.22(b) contains the

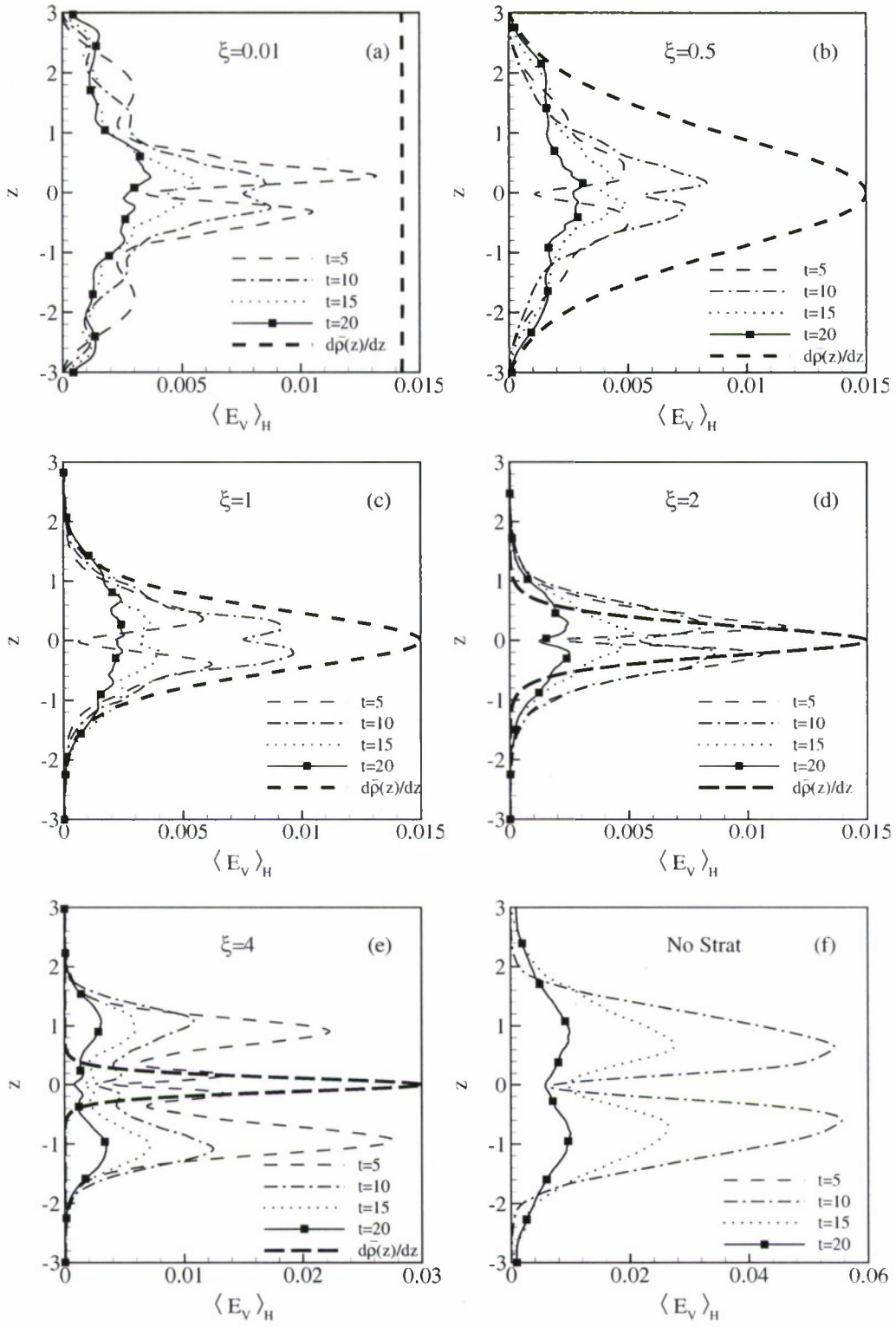

Figure 4.18: $\langle E_V \rangle_H$ for several ξ and no stratification. Note the difference in horizontal scale for plots (e), (f). $d\bar{\rho}(z)/dz$ is shown as bold dashed line, and is scaled differently in each figure for comparison to $\langle E_V \rangle_H$. Bold horizontal lines mark where $d\bar{\rho}(z)/dz = -0.01$. Since the entire vertical domain satisfies this criterion for plots (a)-(b), no bold horizontal lines are shown.

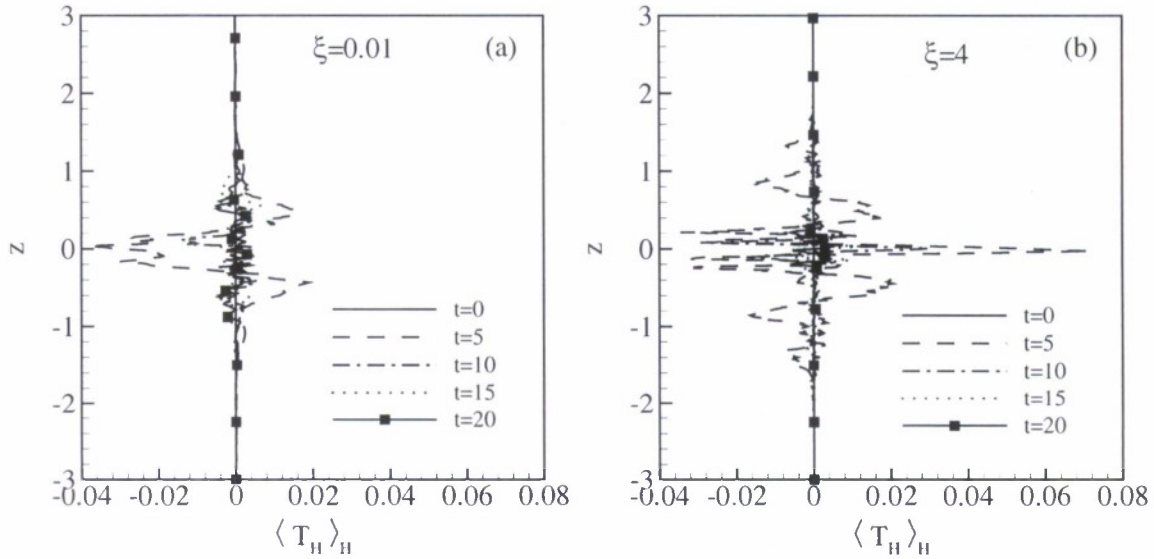

Figure 4.19: Evolution of $\langle T_H \rangle_H$ for (a) $\xi = 0.01$; (b) $\xi = 4$. Note other stratified simulations are qualitatively similar

.

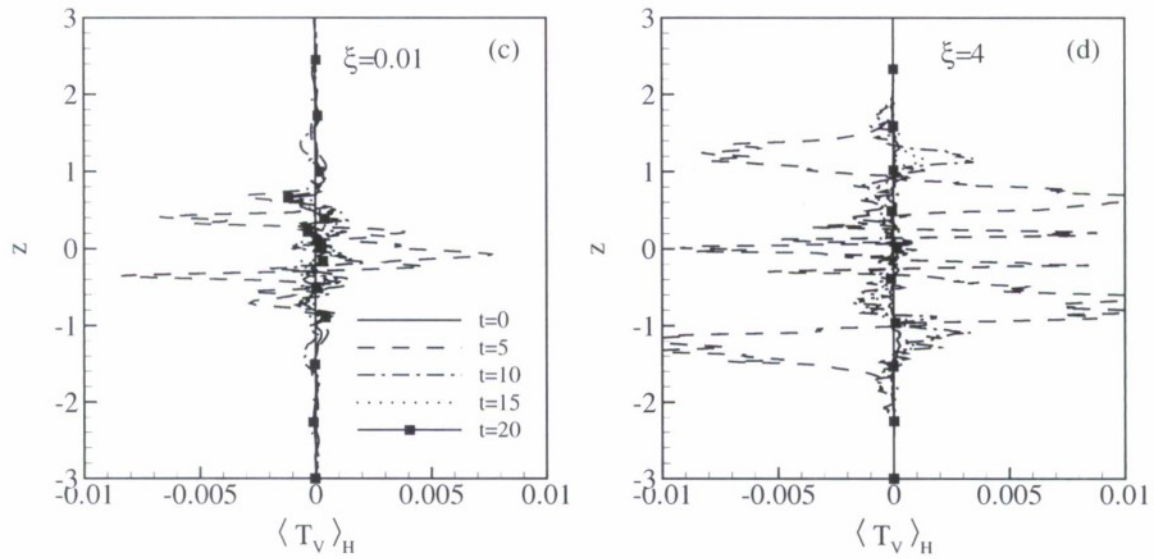

Figure 4.20: Evolution of $\langle T_V \rangle_H$ for (a) $\xi = 0.01$; (b) $\xi = 4$. Note other stratified simulations are qualitatively similar

.

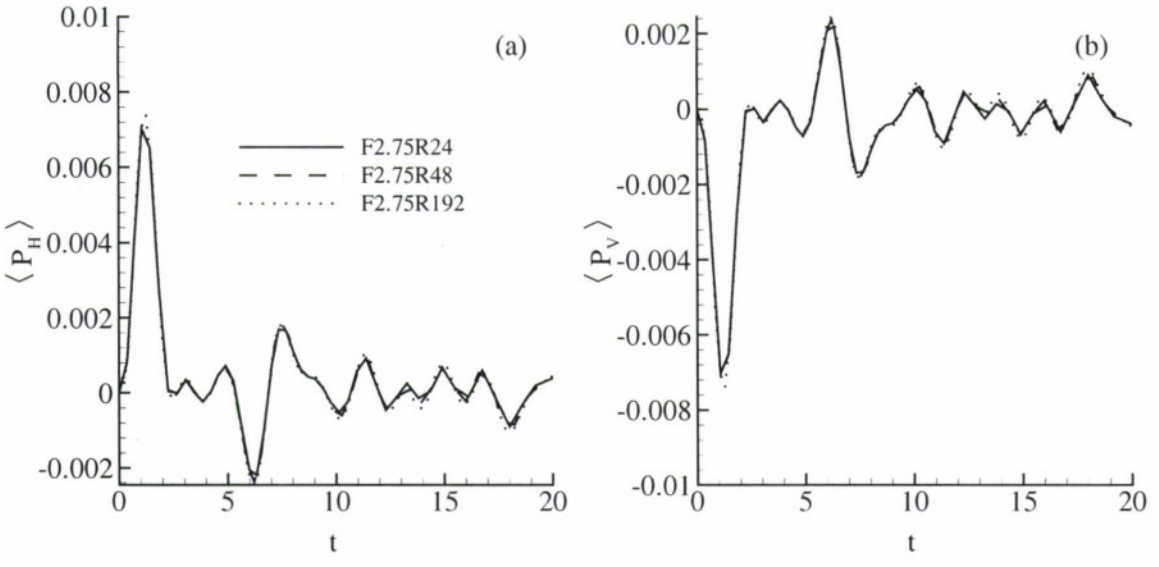

Figure 4.21: (a) $\langle P_H \rangle$; (b) $\langle P_V \rangle$ for several $\mathrm{Re_r}$ and $\xi = 0.01$

same data as Figure 4.22(a), but with the horizontal axis zoomed in to t=0-5. Since pressure work must sum to zero for a periodic simulation, $\langle P_V \rangle$ will be the opposite of $\langle P_H \rangle$ (as seen in Figure 4.21 above) and is not shown here. Early in time, there is a significant amount of pressure work created as internal waves are generated in response to the initial cyclostrophic imbalance. It is interesting to see that the magnitude of $\langle P_H \rangle$ for $\xi = 4$ is nearly half the magnitude of $\langle P_H \rangle$ for the other ξ. The reduction in magnitude for $\xi = 4$ can be explained by noting that internal waves cannot exist when there is no density stratification, and when $\xi = 4$ a significant portion of the simulation domain has minimal density stratification (Figure 4.7). Thus, internal waves (and hence and pressure work) do not occur in much of the simulation area for $\xi = 4$, and a drop in the volume averaged $\langle P_H \rangle$ is seen. This can be seen in a plot of the horizontally averaged $\langle P_H \rangle_H$, shown in Figure 4.23.

The kinetic energy dissipation rates ε_H and ε_V are the amount of E_H and E_V that are dissipated into internal energy via viscous effects. The time evolution of $\langle \varepsilon_H \rangle$ and $\langle \varepsilon_V \rangle$ with $\xi = 0.01$ and several different $\mathrm{Re_r}$ are shown in Figures 4.24(a), (b). Since the initial conditions are the same for each simulation, and only Reynolds number is changed, the initial dissipation rates $\langle \varepsilon_H \rangle$ and $\langle \varepsilon_V \rangle$ are inversely proportional to $\mathrm{Re_r}$. This relationship changes as the flow develops; $\langle \varepsilon_H \rangle$ increases with $\mathrm{Re_r}$ as the flow has more ability to generate small-scale instabilities, consistent with the increase in small-scale spectra shown in Figure 4.14(a). It is interesting to note that while $\langle \varepsilon_H \rangle$ and $\langle \varepsilon_V \rangle$ increase faster with $\mathrm{Re_r}$, their final magnitudes are nearly the same for all $\mathrm{Re_r}$. This suggests that a "high Reynolds number limit" has been reached, where the flow cannot further dissipate kinetic energy.

Copmarisons of $\langle \varepsilon_H \rangle$ and $\langle \varepsilon_V \rangle$ for each ξ simulation are found in Figures 4.25(a), (b). As the flows evolve, small scale turbulence forms and both $\langle \varepsilon_H \rangle$ and $\langle \varepsilon_V \rangle$ increase in time before decaying. There is a clear transition in the behavior of $\langle \varepsilon_H \rangle$ and $\langle \varepsilon_V \rangle$ between $\xi = 2$ and $\xi = 4$. The reason for this transition can be explained by the behavior of $\langle S^2 \rangle_H$, the terms of which are components of $\langle \varepsilon_H \rangle$ and $\langle \varepsilon_V \rangle$. When $\xi = 4$, a large amount of overturning occurs outside the density stratification layer, which causes a significant amount of shear and kinetic energy dissipation rate to form early in the simulation (Figures 4.26, 4.27. Figure

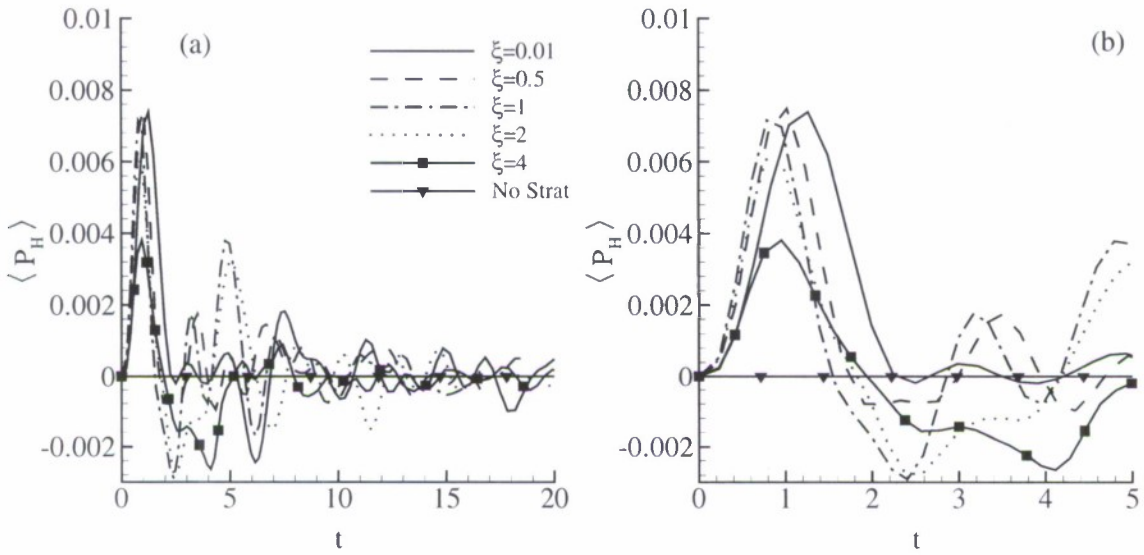

Figure 4.22: (a) Time evolution of $\langle P_H \rangle$ for several ξ, $\overline{\mathrm{F}}_r = 2.75$, $\mathrm{Re_r} = 19200$. (b) Same as (a), but zoomed horizontal axis.

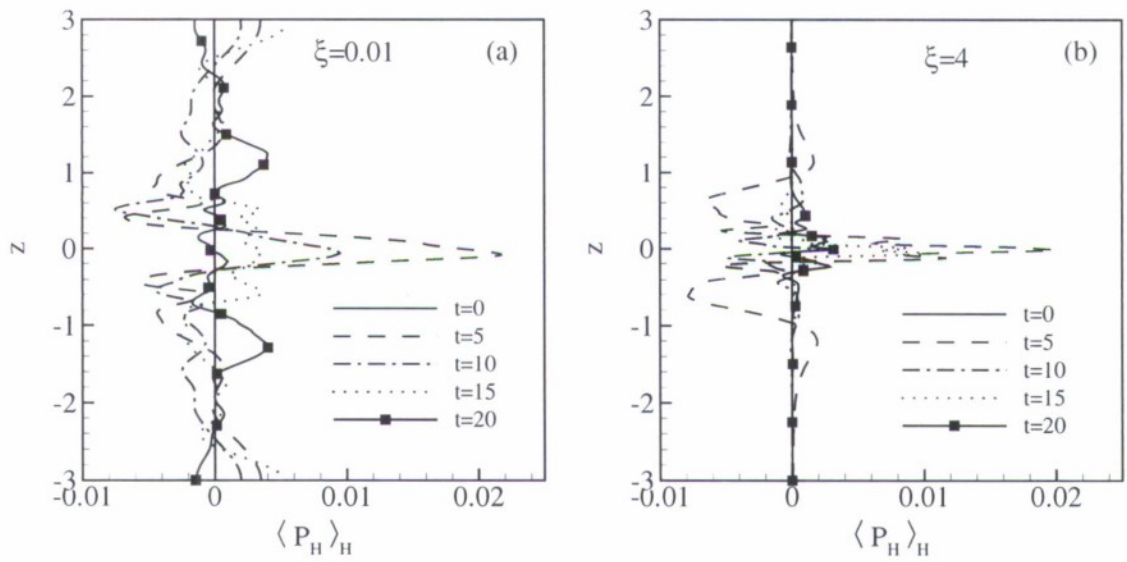

Figure 4.23: Evolution of $\langle P_H \rangle_H$ for (a) $\xi = 0.01$; (b) $\xi = 4$.

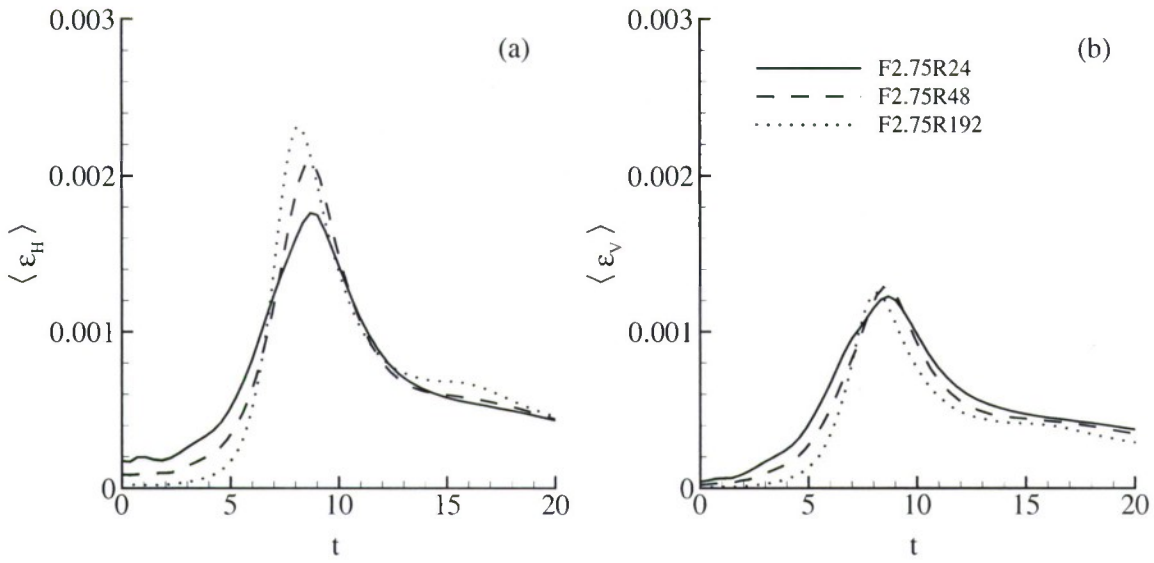

Figure 4.24: Evolution of (a) $\langle \varepsilon_H \rangle$, (b) $\langle \varepsilon_V \rangle$ for all $\xi = 0.01$ simulations.

4.28 contains plots of $\langle \varepsilon_H \rangle_H$ and $\langle \varepsilon_V \rangle_H$ for $\xi = 4$ with zoomed vertical axis).

ϕ is the quantity that remains when separating the last term in the total kinetic energy equation (4.6) into horizontal and vertical components. It is a term that couples horizontal and vertical kinetic energy through a process of viscous and rotational strain. The time evolution of $\langle \phi \rangle$ for all $\xi = 0.01$ simulations is shown in Figure 4.29(a). Similar to $\langle \varepsilon_H \rangle$, $\langle \phi \rangle$ increases with turbulence formation up to approx. $t = 8$. However, in contrast with $\langle \varepsilon_H \rangle$ and $\langle \varepsilon_V \rangle$, there is a clear inverse relation between $\langle \phi \rangle$ and Re throughout the simulation. This is likely due to the decrease in ν with $\mathrm{Re_r}$, causing a decrease in viscous coupling (and hence ϕ) between $\langle E_H \rangle$ and $\langle E_V \rangle$. Note the magnitude of ϕ is much smaller than ε, indicating a very small role in the transport of energy.

Figure 4.29(b) contains a plot of $\langle \phi \rangle$ for each ξ, where the overall trend is for $\langle \phi \rangle$ to increase with ξ up to $\xi = 4$. The increase in magnitude of $\langle \phi \rangle$ with ξ can be explained by noting that as ξ is increased the local stratification is increased. The increase in local stratification causes "stronger" decoupling of horizontal layers, and an increase in shear that results in stronger coupling between vertical and horizontal motions. When $\xi = 4$ $\langle \phi \rangle$ reaches a maximum much earlier than the other simulations. This behavior is similiar to that seen for $\langle \varepsilon_H \rangle$ and $\langle \varepsilon_V \rangle$ (Figure 4.25), where strong horizontal decoupling causes a large amount of $\langle \phi \rangle$ to form early in the simulation.

It is interesting that in Figure 4.29 $\langle \phi \rangle$ is nearly zero for the non-stratified case. This seems counter-intuitive, since when there is no stratification there is no buoyancy force and overturning can readily occur. However, when there is no stratification there is very little horizontal layer decoupling compared to stratified flow. With no buoyancy force, rotational shear is minimized, and ϕ will be much smaller compared to when the flow is stratified. This is seen in plots of the planar averaged $\langle \phi \rangle_H$ shown Figure 4.30, where $\langle \phi \rangle_H$ is barely visible for the No Strat simulation. Also, when $\xi = 4$ $\langle \phi \rangle_H$ is near zero outside the stratification layer, whereas significant $\langle \varepsilon \rangle_H$ occurs when the stratification is minimal (Figures 4.26 and 4.27).

The buoyancy flux term B is a coupling term between E_V and E_P. As mass is advected

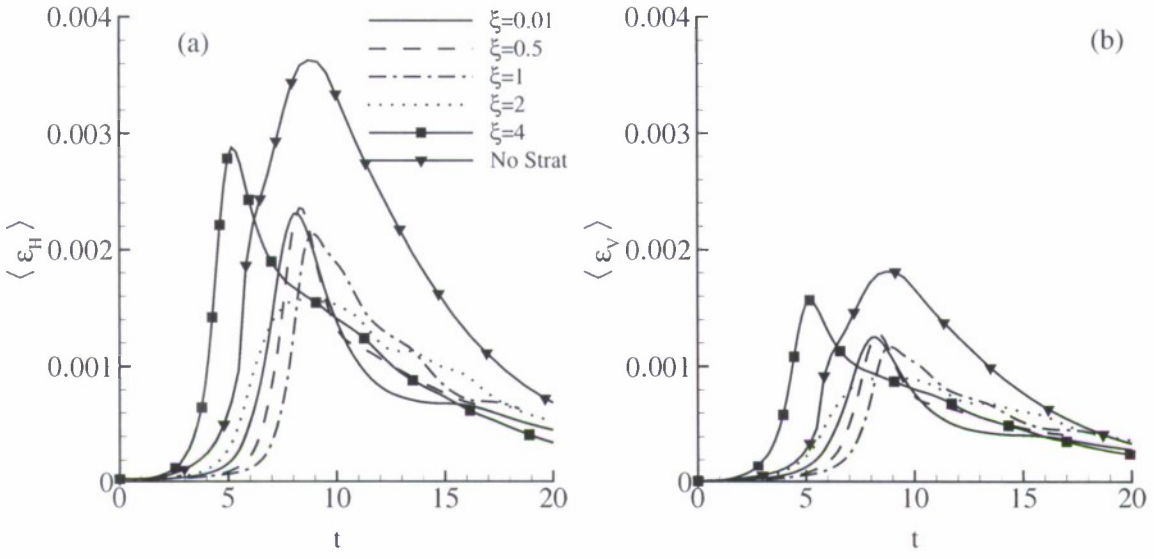

Figure 4.25: Evolution of (a) $\langle \varepsilon_H \rangle$, (b) $\langle \varepsilon_V \rangle$ for each ξ simulation.

vertically it must do work against gravity, and energy is transferred from E_V to E_P. Figure 4.31(a) contains the time evolution of $\langle B \rangle$ for several $\mathrm{Re_r}$, $\xi = 0.01$. Interpretation of $\langle B \rangle$ on a time basis is difficult because E_V converted to E_P at one time can be released back to E_V at another. However, from Figure 4.31(a) one can conclude that there is a large initial buoyancy flux $\langle B \rangle$ as the flow adjusts to the initial cyclostrophic imbalance, supported by the fact that the oscillation in $\langle B \rangle$ is exactly 180° out of phase with $\langle P_V \rangle$. After this initial adjustment, the remaining oscillations in $\langle B \rangle$ are likely caused by the propagation of internal gravity waves.

Potential Energy

Figure 4.32(a) contains a plot of the volume averaged available potential energy $\langle E_P \rangle$ for several $\mathrm{Re_r}$, $\overline{\mathrm{F}}_r = 2.75$, $\xi = 0.01$, where a rapid initial increase in $\langle E_P \rangle$ is caused by the formation of an internal wave from initial cyclostrophic adjustment. Following this initial rise, $\langle E_P \rangle$ decays to an undisturbed state. The oscillations in $\langle E_P \rangle$ after $t \approx 5$ are transfer between E_P and E_V via buoyancy flux $\langle B \rangle$. This is supported by the the fact that the oscillations in $\langle E_P \rangle$ and $\langle B \rangle$ (Figure 4.31(a)) are in phase with each other. The increase in $\langle E_P \rangle$ with $\mathrm{Re_r}$ is due to the flow's increased ability to overcome stratification.

The time evolution of $\langle E_P \rangle$ for each ξ is show in in Figure 4.32(b). After the initial flow response to the initial contitions by $t \approx 5$, the general trend is for $\langle E_P \rangle$ to be relatively independent of ξ until $\xi = 2$, after which there is a drop in $\langle E_P \rangle$ with ξ. This drop in $\langle E_P \rangle$ can be explained by noting that, by definition, E_P is zero outside the stratification layer (since in the limit where $d\bar{\rho}(z)/dz = 0$, $N = 0$, and $\mathrm{F_r} = \infty$). Recalling that $w\rho$ is a source term of E_P (equation 4.26), when $\xi = 2$, the vertical span of E_P has narrowed beyond the vertical span of w. $\langle E_P \rangle$ will thus incorporate areas where E_P is zero, even though vertical motion occurs. This can be seen in Figure 4.33, where the peak planar averaged $\langle E_P \rangle_H$ is nearly the same for all ξ, even though there a sharp increase in the volume averaged $\langle E_P \rangle$.

T_P is a term that describes the advection of potential energy, and is similar to T_H and T_V. Since the boundary conditions are periodic, the volume averaged $\langle T_P \rangle$ will be zero, and

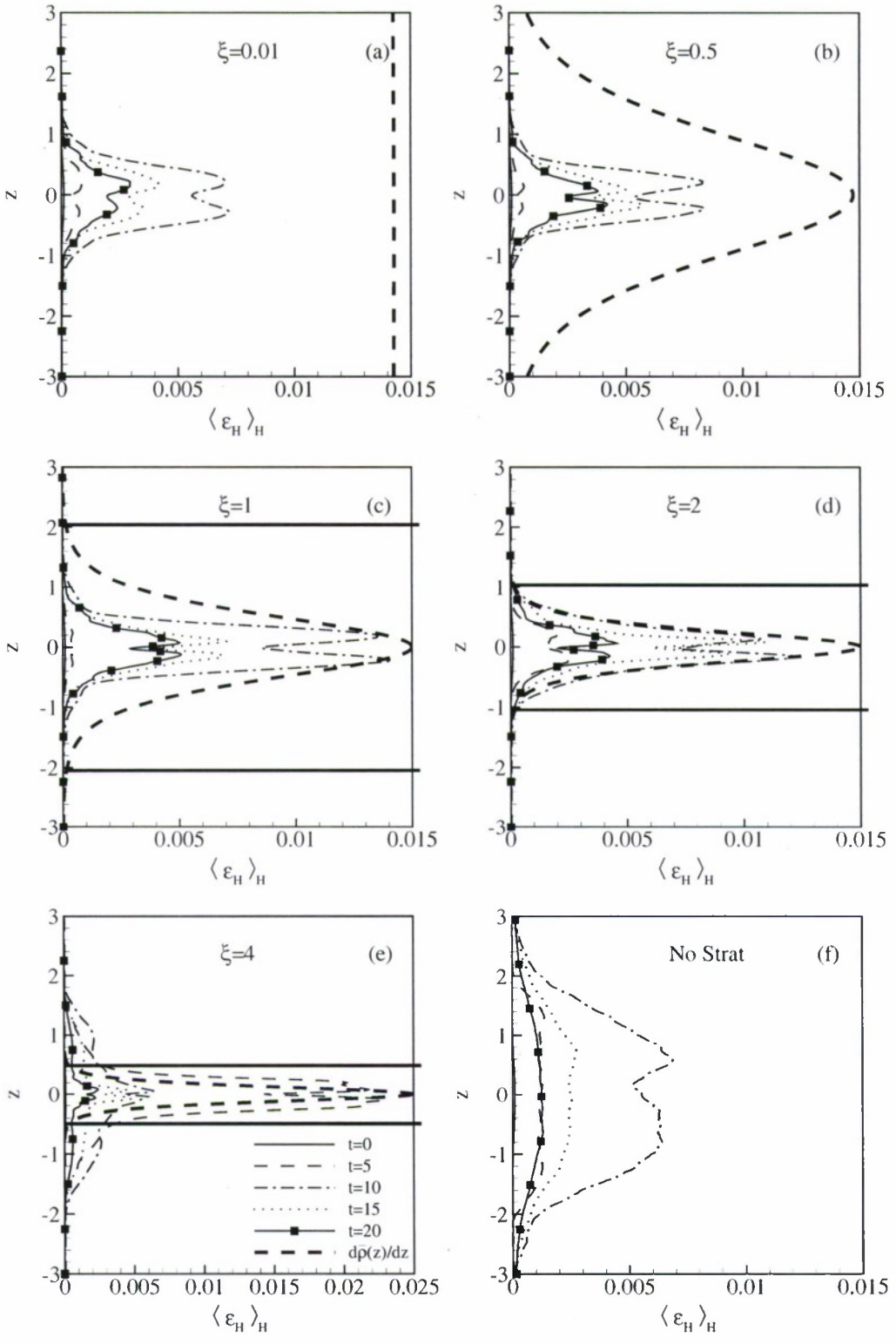

Figure 4.26: Evolution of $\langle \varepsilon_H \rangle_H$ for all ξ. The dashed line represents the density stratification $d\bar{\rho}(z)/dz$. The bold solid lines identify where $d\bar{\rho}(z)/dz = -0.01$. Since the entire vertical domain satisfies this criterion for plots (a)-(b), no bold horizontal lines are shown. When $\xi = 4$, much of the $\langle \varepsilon_H \rangle_H$ is formed earlier in time outside the stratification layer

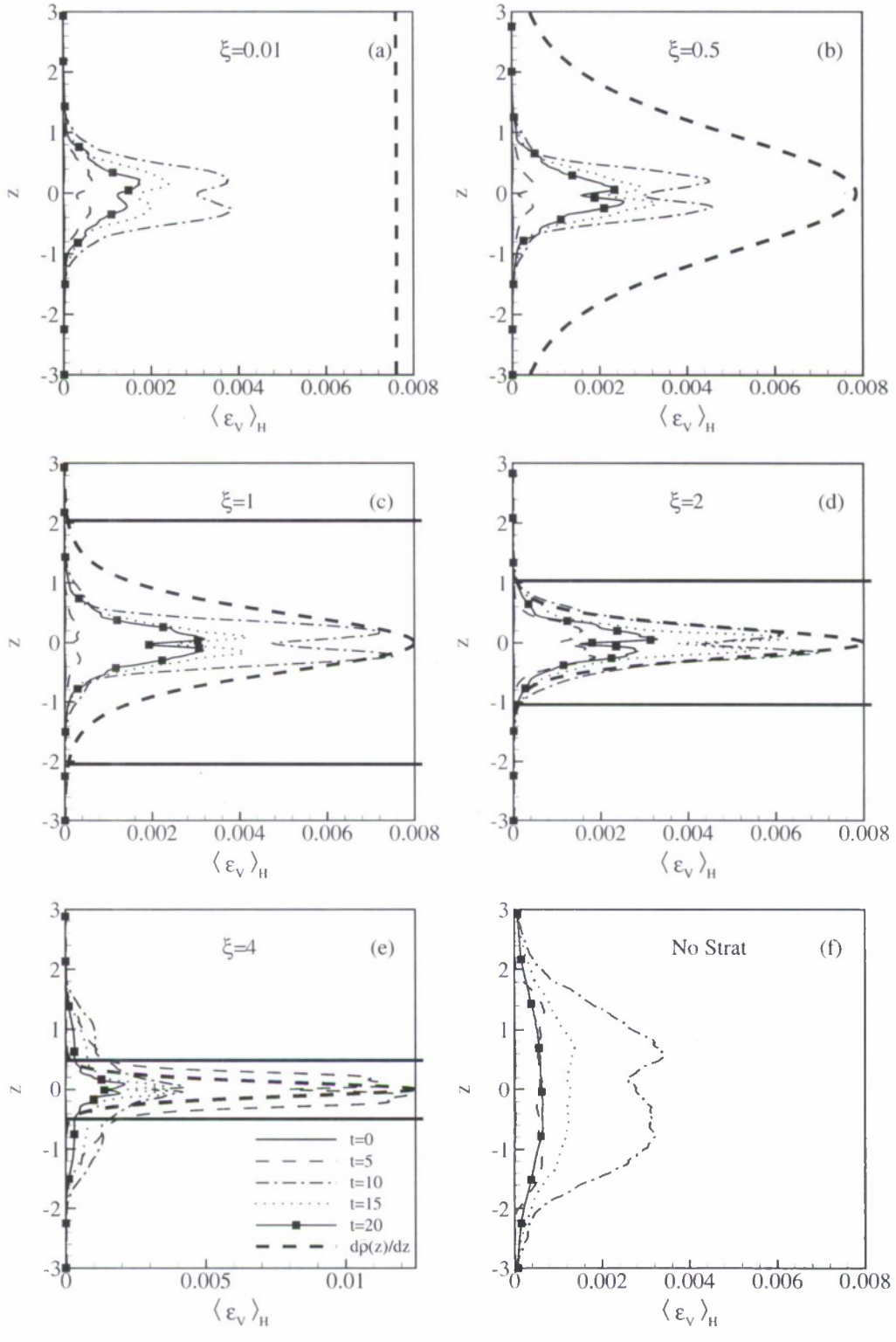

Figure 4.27: Evolution of $\langle \varepsilon_V \rangle_H$ for all ξ. The dashed line represents the density stratification $d\bar{\rho}(z)/dz$. The bold solid lines identify where $d\bar{\rho}(z)/dz = -0.01$. Since the entire vertical domain satisfies this criterion for plots (a)-(b), no bold horizontal lines are shown. When $\xi = 4$, much of the $\langle \varepsilon_V \rangle_H$ is formed earlier in time outside the stratification layer

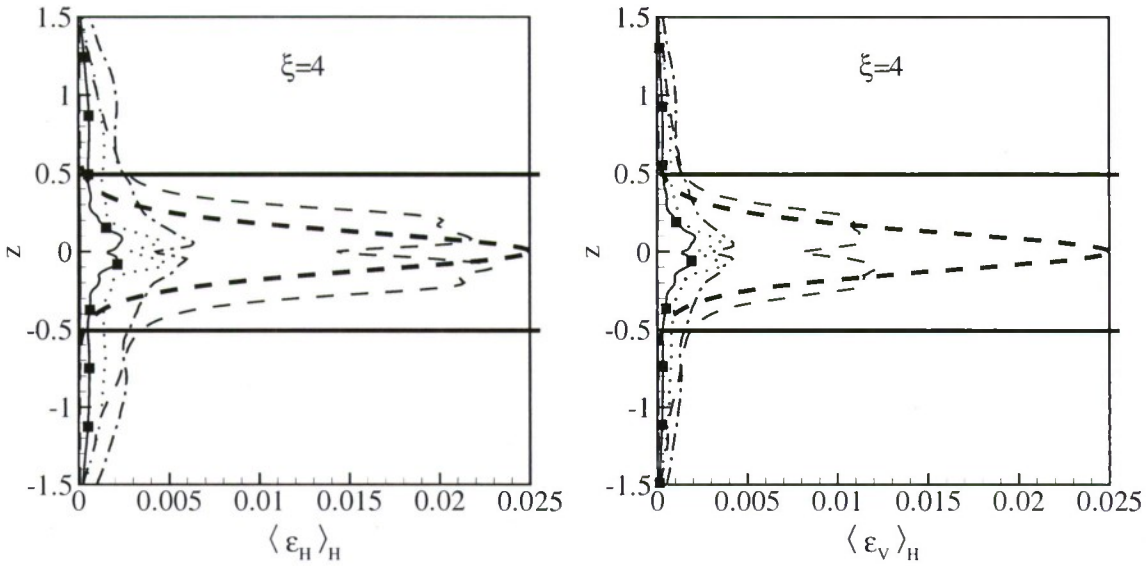

Figure 4.28: $\langle \varepsilon_H \rangle_H$ (left) and $\langle \varepsilon_V \rangle_H$ (right) for $\xi = 4$. The plots are the same as in Figures 4.27(e) and 4.27(e), but with zoomed vertical axis.

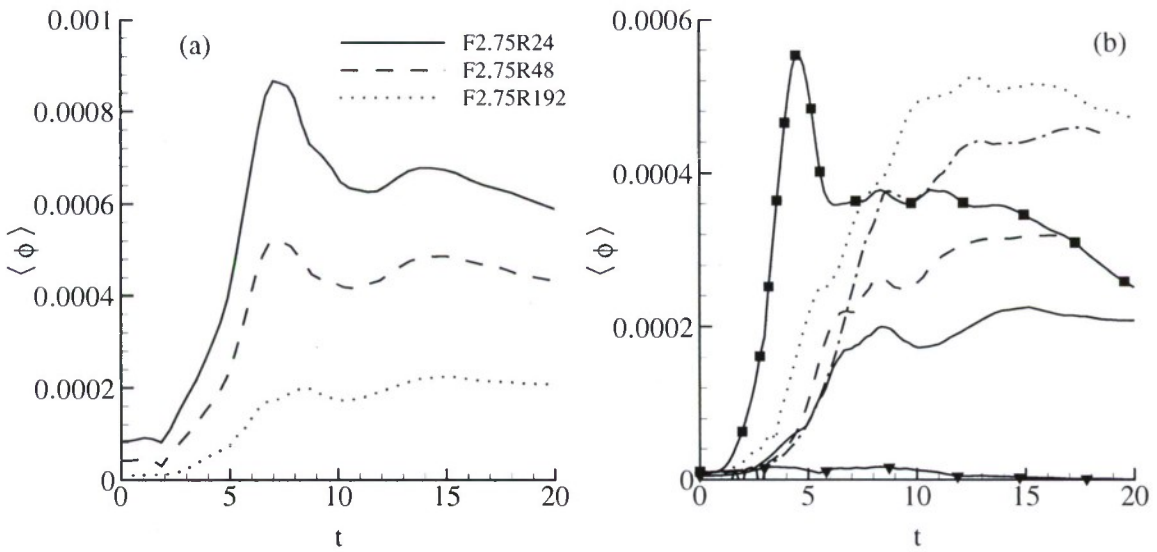

Figure 4.29: Evolution of $\langle \phi \rangle$ for (a) several $\mathrm{Re_r}$, $\xi = 0.01$, (b) Several ξ, $\overline{\mathrm{F}}_r = 2.75$, $\mathrm{Re_r} = 19200$. The lines in (b) correspond to those shown in Figure 4.25

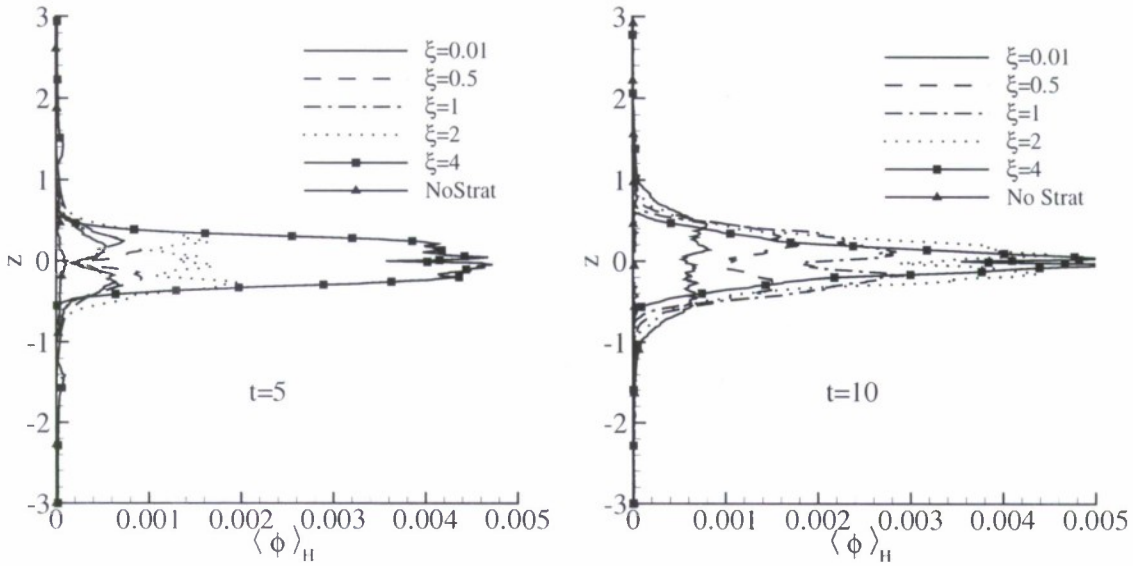

Figure 4.30: $\langle\phi\rangle_H$ at for all ξ at t =5 (left) and t =10 (right). Note that when the stratification is small for $\xi = 4$ and the No Strat simulation $\langle\phi\rangle_H$ is small.

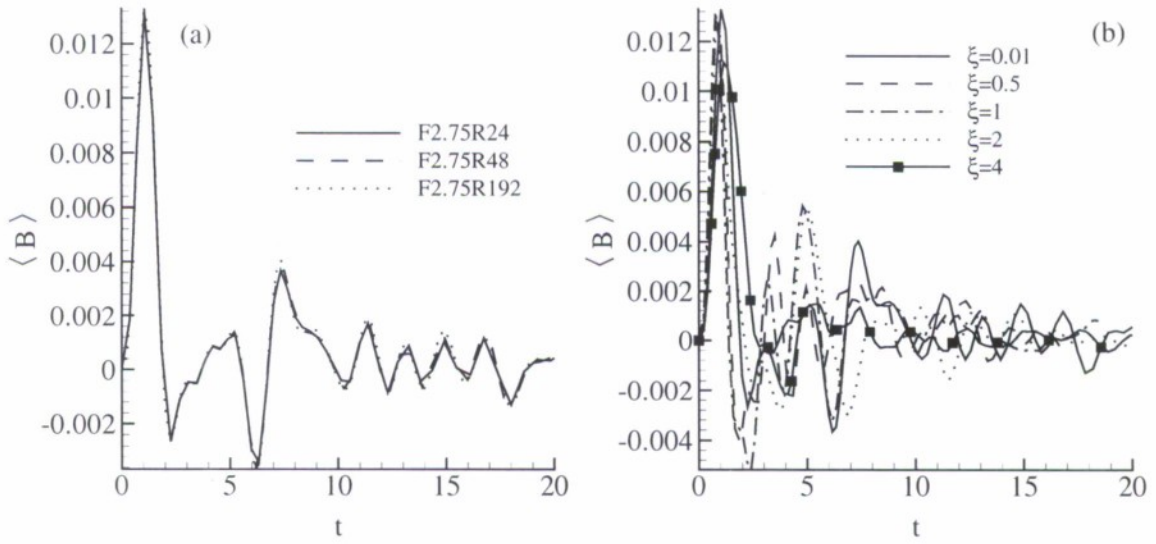

Figure 4.31: Evolution of $\langle B\rangle$ for (a) several $\mathrm{Re_r}$, $\xi = 0.01$, (b) Several ξ, $\overline{\mathrm{F}}_r = 2.75$, $\mathrm{Re_r} = 19200$.

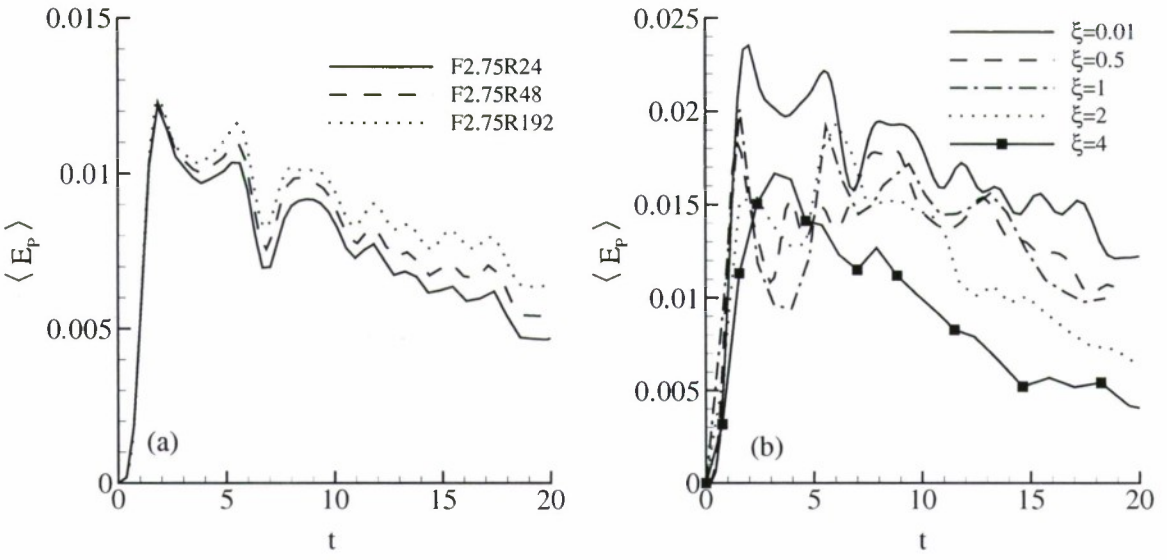

Figure 4.32: Time evolution of $\langle E_P \rangle$ for (a) several $\mathrm{Re_r}$, $\overline{\mathrm{F}}_r = 2.75$, $\xi = 0.01$, (b) Several ξ, $\overline{\mathrm{F}}_r = 2.75$, $\mathrm{Re_r} = 19200$.

is not shown here.

Planar averaged $\langle T_P \rangle_H$ for F2.75R192 is shown in Figure 4.34. $\langle T_P \rangle_H$ is qualitatively similar for all simulations. Early in the simulation at $t \approx 5$, E_P is seen to be advected into the center planes from the adjoining planes, where the initial high vertical shear is formed. Advection then diminishes, as the majority of transport of E_P occurs due to B and χ.

χ is the potential energy dissipation rate, which can be described as the irreversible conversion from available to background potential energy, similar to ε (see §4.2.2 for further discussion on background potential energy). The time evolution of the volume averaged $\langle \chi \rangle$ for several $\mathrm{Re_r}$ and $\xi = 0.01$ is shown in Figure 4.35(a). Since the flow is initialized with no density fluctuation, $\langle \chi \rangle$ is also initially zero. Early in the simulation ($t < 7$) $\langle \chi \rangle$ is inversely proportional to $\mathrm{Re_r}$, a result of the fact that the initial condition for each simulation is the same, and only the mass diffusivity $\mathcal{D}$ is changed (recall that $\mathrm{Sc} = 1$ for all simulations). Then, as the flow evolves further and turbulent small-scale motions form, $\langle \chi \rangle$ demonstrates an increase with $\mathrm{Re_r}$, similar to $\langle \varepsilon \rangle$.

The time evolution of $\langle \chi \rangle$ for each ξ is shown in Figure 4.35(b), where the magnitude of $\langle \chi \rangle$ increases in time as small scale turbulence forms. The time to reach peak $\langle \chi \rangle$ increases as ξ is increased from 0.01 to 2. When $\xi = 4$, in contrast, the peak $\langle \chi \rangle$ occurs earlier, indicating turbulent motions occur earlier in time. This behavior is in agreement with that seen for the kinetic energy dissipation rates (Figure 4.25). However, unlike $\langle \varepsilon_H \rangle$ and $\langle \varepsilon_V \rangle$, the magnitude of $\langle \chi \rangle$ decreases when $\xi \geq 2$. This is because χ is zero when there is no stratification for the same reason E_P is zero. Thus, when $\xi > 2$, a significant portion of the volume has $\chi = 0$, (Figure 4.36), which causes $\langle \chi \rangle$ to be small.

4.5.3 Mixing and Mixing Efficiency

The behavior of $\langle \varepsilon \rangle$ and $\langle \chi \rangle$ with respect to ξ has implication in modeling the Earth's energy budget. Current Earth general circulation models (gcm's), assuming linear density stratification, show an imbalance in vertical heat fluxes by as much as 20% [Howard et al.,

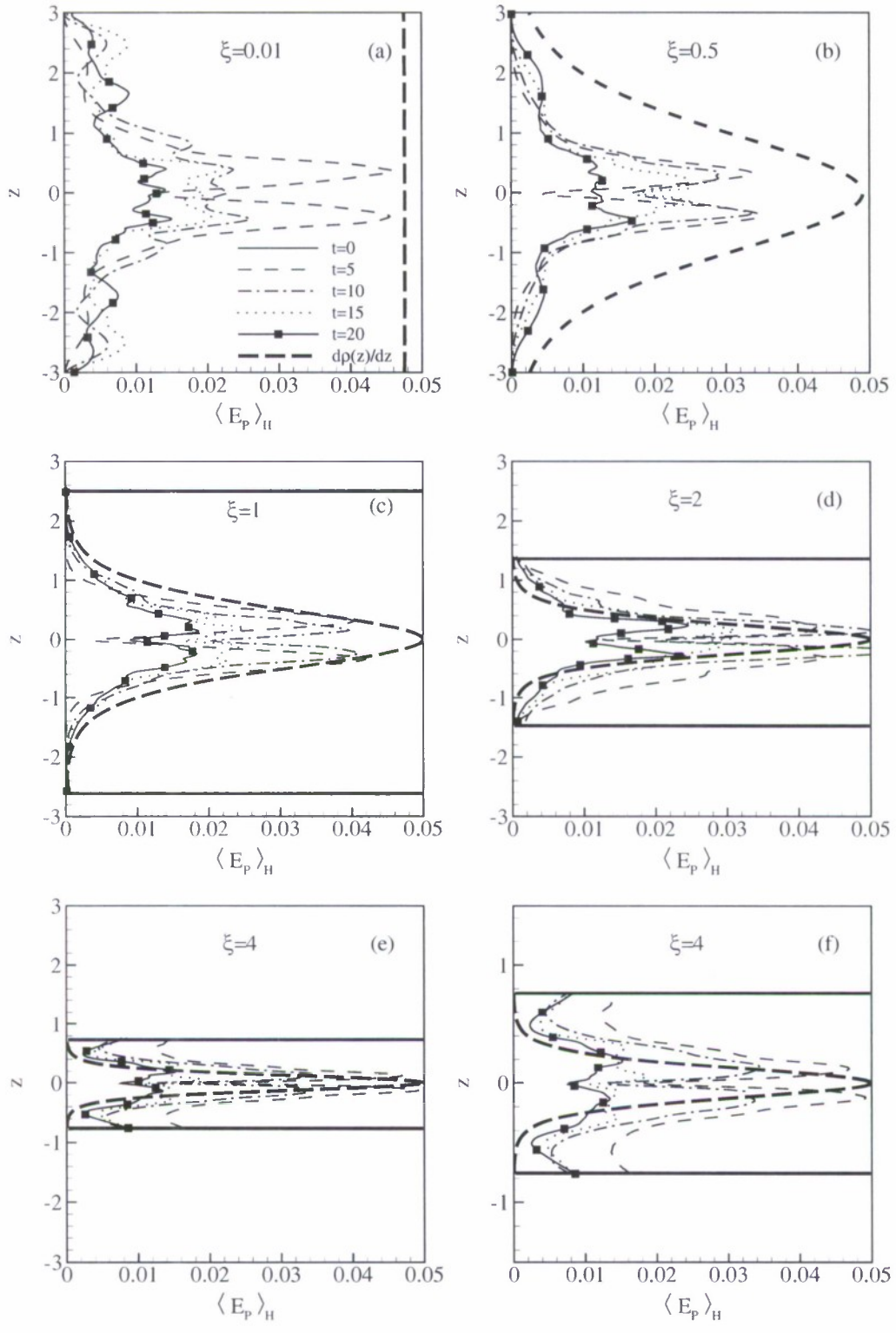

Figure 4.33: Evolution of $\langle E_P \rangle_H$ for each ξ. $d\bar{\rho}(z)/dz$ is shown as bold dashed line, and is scaled differently in each figure for comparison. Bold horizontal lines mark where $d\bar{\rho}(z)/dz = -0.01$. Since the entire vertical domain satisfies this criterion for plots (a)-(b), no bold horizontal lines are shown.

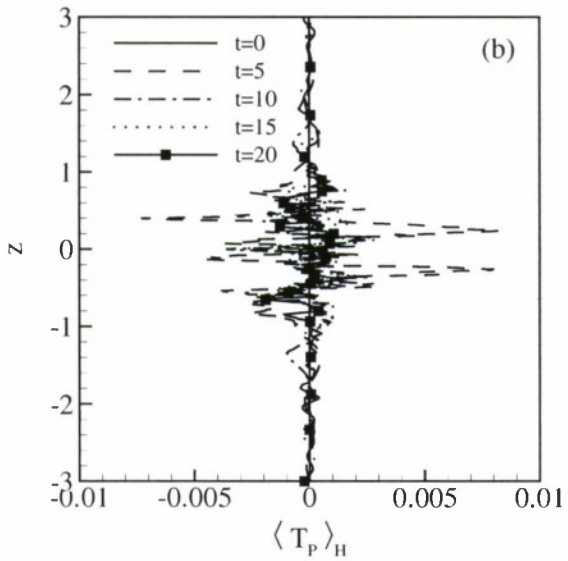

Figure 4.34: Evolution of $\langle T_P \rangle_H$ for simulation F2.75R192

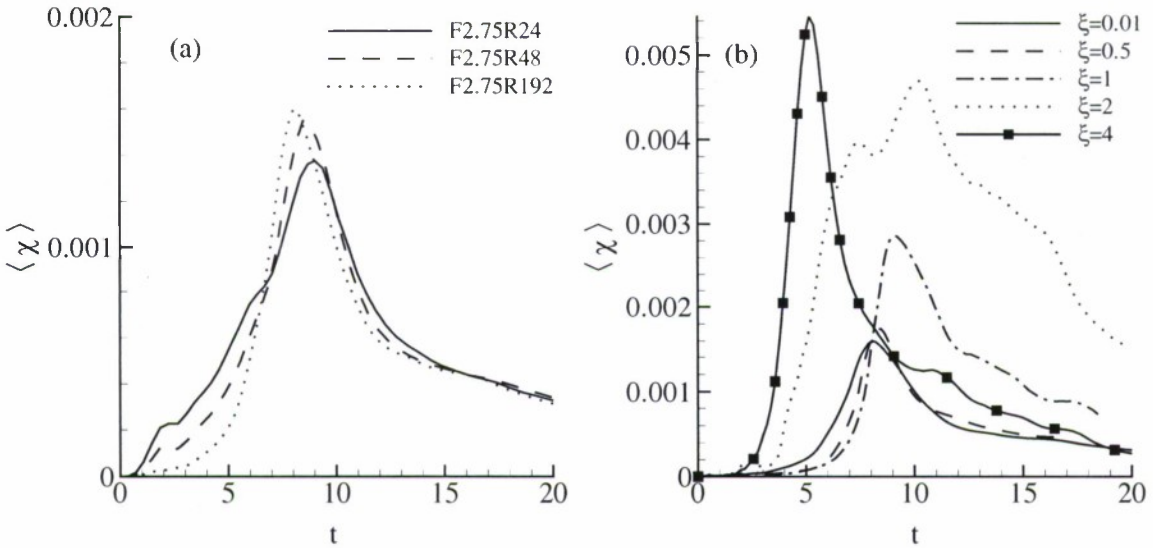

Figure 4.35: Evolution of $\langle \chi \rangle$ for (a) several $\mathrm{Re_r}$, $\xi = 0.01$, (b) Several ξ, $\overline{\mathrm{F}}_r = 2.75$, $\mathrm{Re_r} = 19200$.

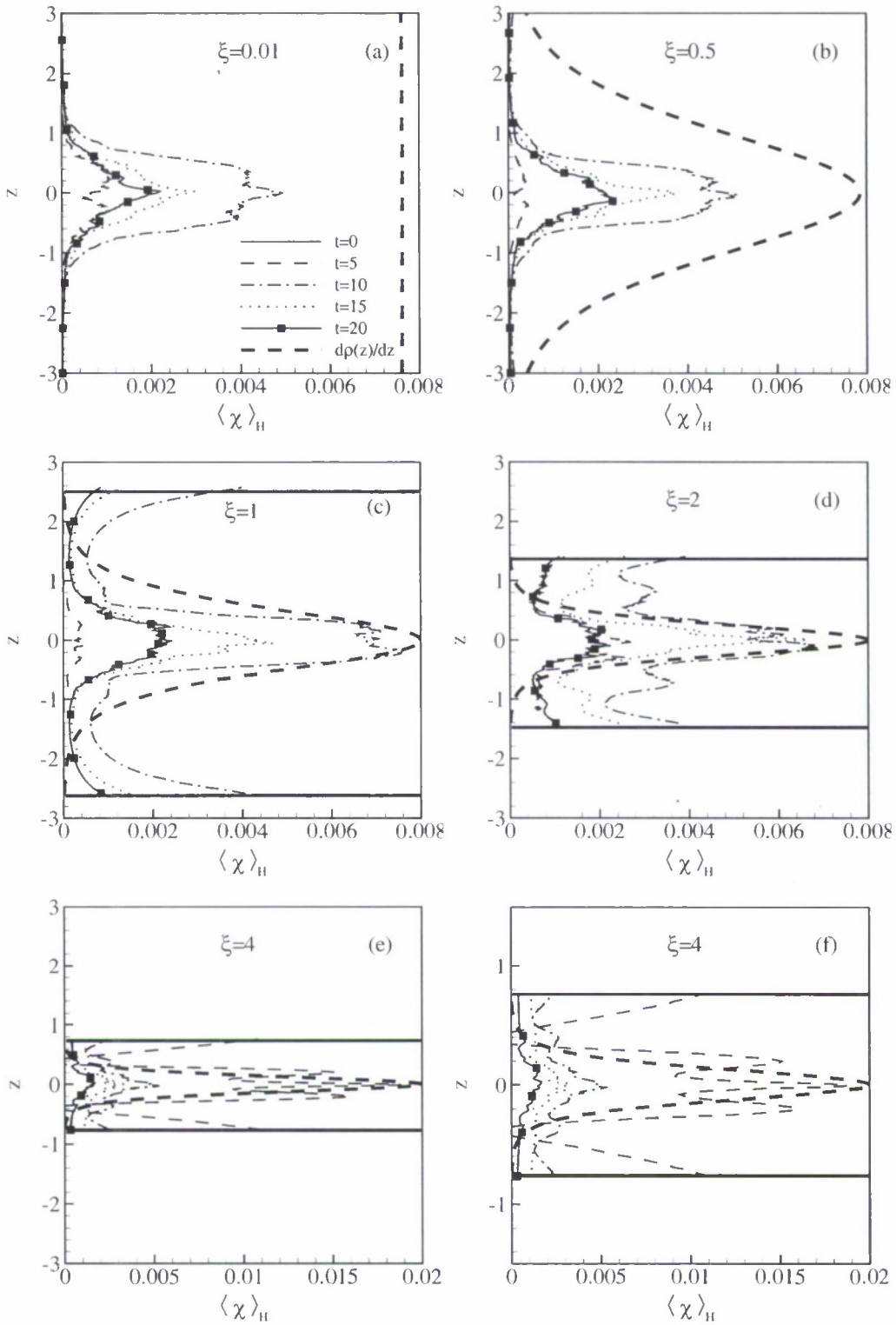

Figure 4.36: Evolution of $\langle\chi\rangle$ for each ξ. $d\bar{\rho}(z)/dz$ is scaled different for each figure, and is shown for comparison to $\langle\chi\rangle_H$. Bold horizontal lines mark where $d\bar{\rho}(z)/dz = -0.01$. Since the entire vertical domain satisfies this criterion for plots (a)-(b), no bold horizontal lines are shown.

2004, Marmorino and Caldwell, 1976, Robertson et al., 1995]. This imbalance may be due to the mixing results obtained with a linear density stratification throughout the Earth's atmosphere and ocean. From Figures 4.25 and 4.35(b), one can see that for the same initial flow conditions, peak $\langle\varepsilon\rangle$ increases by 25% when a sharp density gradient exists ($\xi = 4$), while $\langle\chi\rangle$ decreases by 50%. This results suggests that in areas of sharp density gradients, assuming a uniform density gradient leads to under-predicting mixing of kinetic energy ε, and over-predicting χ.

As discussed in §1.2.2, a quantity of interest is the mixing efficiency Γ, which is the ratio of the available potential energy lost by molecular diffusion to kinetic energy lost by viscous dissipation [e.g., Smyth et al., 2001, Winters et al., 1995]. Here Γ will be defined as in (1.4) (and dropping the subscript a):

$$\Gamma = \frac{\widetilde{\chi}}{\widetilde{\varepsilon}}. \tag{4.35}$$

Γ is of interest because it is difficult to measure both ε and χ simultaneously in field experiments due to the time scales required to measure each quantity [Gargett and Moum, 1995]. Thus, it would be beneficial to measure one quantity (usually ϵ) and relate it to the other [Osborn, 1980]. Figure 4.37(a) contains the volume averaged mixing efficiency $\langle\Gamma\rangle = \langle\widetilde{\chi}\rangle / \langle\widetilde{\varepsilon}\rangle$. Initially, $\Gamma = 0$ (since $\chi = 0$), after which there is a rapid increase in $\langle\Gamma\rangle$ to near 0.9 as the density field responds to the initial cyclostrophic imbalance. As the flow evolves and small-scale instabilities occur, $\widetilde{\varepsilon}$ increases and causes $\langle\Gamma\rangle$ to drop to ≈ 0.45, in agreement with results from other numerical simulations of uniformly stratified flows [e.g., Riley and de Bruyn Kops, 2003, Smyth et al., 2001, Staquet, 2000]. $\langle\Gamma\rangle$ is also shown to be relatively independent of $\mathrm{Re_r}$, which is consistent with the aforementioned studies.

The evolution of $\langle\Gamma\rangle$ for each ξ is shown in Figure 4.37(b), where the general trend is for a large initial $\langle\Gamma\rangle$ to form up to $t \approx 7$, after which $\langle\Gamma\rangle$ settles to a constant value related to the value of ξ. The early rise in $\langle\Gamma\rangle$ is due to the flow's initial ability to dissipate available potential energy to background potential energy (χ) faster than kinetic energy is dissipated to internal energy (ε). As the flow progresses and small-scale instabilities occur, ε increases and causes $\langle\Gamma\rangle$ to drop before settling to some constant value. These results are consistent with the aforementioned studies of uniformly stratified flows.

Since the vertical span of χ decreases as ξ increases (Figure 4.36), the value of $\langle\Gamma\rangle$ will also decrease due to the inclusion of areas of zero mixing in the volume average. It would be of interest to know what the mixing efficiency is inside the density stratification layer. In this case, the density stratification layer is defined where $|d\bar{\rho}(z)/dz| > 0.01$. The value of 0.01 is chosen because it is 1% of the stratification value when $\xi = 0.01$. Figure 4.38(b) contains a plot of the time evolution of $\langle\Gamma\rangle_{STRAT} = \langle\chi\rangle_{STRAT} / \langle\varepsilon\rangle_{STRAT}$, where the subscript $STRAT$ denotes average over the density stratification range. Large initial values of $\langle\Gamma\rangle_{STRAT}$ can be seen for the same reasons as $\langle\Gamma\rangle$. It is interesting to note that $\langle\Gamma\rangle_{STRAT}$ settles to near the same value for all ξ.

To get a better idea of how Γ is behaving throughout this flow, the planar averaged $\langle\Gamma\rangle_H = \langle\chi\rangle_H / \langle\varepsilon\rangle_H$ for each ξ is shown in Figure 4.39, where the value of $\langle\Gamma\rangle_H$ is relatively independent of ξ in the center of the domain. The peak at $z = 0$ is due to the centerplane dip in $\langle\varepsilon\rangle_H$ seen in Figures 4.26, 4.27. The trend for $\langle\Gamma\rangle_H$ to increase when $|z| > 0.5$ is due to the decreasing value of ε in this range. Outside $|z| > 0.5$ ε is very small and results in a noisy $\langle\Gamma\rangle_H$, particularly for $\xi = 0.5$. In addition, since χ is zero outside the stratification layer, Γ is also zero. This suggests that in an area with non-uniform density stratification, mixing can only occur in the region of high density gradient. Such a result is in agreement with the findings of Schmitt [2003], St. Laurent and Schmitt [1999], where increased mixing

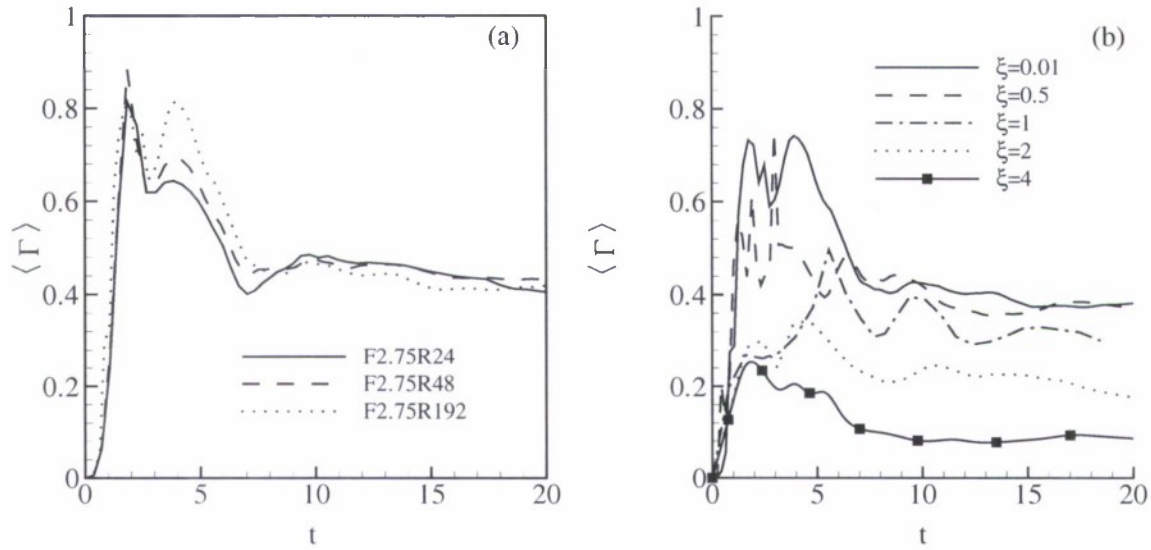

Figure 4.37: $\langle\Gamma\rangle$ for (a) several $\mathrm{Re_r}$, $\xi = 0.01$; (b) all ξ, $\overline{\mathrm{F}}_r = 2.75$, $\mathrm{Re_r} = 19200$.

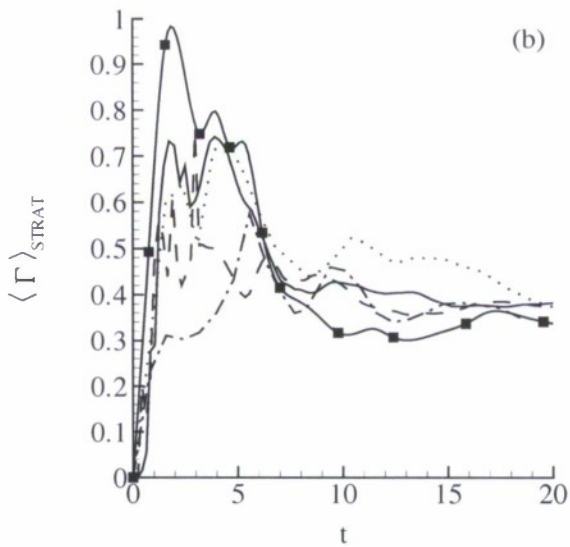

Figure 4.38: Evolution of $\langle\Gamma\rangle_{STRAT}$ for each ξ.

is found in the sharp density gradients of thermohaline staircases, where salt fingering is prone to occur.

4.5.4 Buoyancy Reynolds Number

In stratified flows, the importance of turbulence is often parameterized in terms of the buoyancy Reynolds number $\mathrm{Re_b}$ [e.g., Gibson, 1980, Gregg, 1987, Imberger and Boashash, 1986, Smyth and Moum, 2000a]. $\mathrm{Re_b}$ is usually defined as the ratio of the Ozmidov scale $\mathrm{L_o}$ to the Kolmogorov scale $\mathrm{L_k}$ (see §2.1.9 for further discussion on $\mathrm{Re_b}$). Recalling equation 2.57, $\mathrm{Re_b}$ is defined as:

$$\mathrm{Re_b} \equiv \left(\frac{\widetilde{\mathrm{L}}_\mathrm{o}}{\widetilde{\mathrm{L}}_\mathrm{k}}\right)^{\frac{4}{3}} = \frac{\widetilde{\epsilon}}{\tilde{\nu}\widetilde{\mathrm{N}}^2}. \tag{4.36}$$

From this definition, $\mathrm{Re_b} = 21.5$ for one decade of turbulent length scales to form. Analysis by Gibson [1980] resulted in $\mathrm{Re_b} \approx 30$ for "active" turbulence to form. Figure 4.40(a) is a plot of the time evolution of the volume averaged buoyancy Reynolds number $\langle \mathrm{Re_b} \rangle = \langle \widetilde{\varepsilon} \rangle / (\tilde{\nu}\widetilde{\mathrm{N}}^2)$ for several $\mathrm{Re_r}$, where the maximum $\langle \mathrm{Re_b} \rangle$ of 14 might suggest that the flow does not have an adequate range of length scales for turbulence to form. This is misleading, as the volume averaged data includes areas outside the wake "core" where there is little energy (and hence $\widetilde{\varepsilon}$), particularly at the outer edges of the flow where $|z| > 2$. Consequently, the planar averaged $\langle \mathrm{Re_b} \rangle_H = \langle \widetilde{\varepsilon} \rangle_H / \tilde{\nu} \left\langle \widetilde{\mathrm{N}} \right\rangle_H$ can be examined to get a better idea of how $\mathrm{Re_b}$ is acting locally. Figure 4.40(b) contains a plot of the time evolution of $\langle \mathrm{Re_b} \rangle_H$ for simulation F2.75R192, where the magnitude of $\langle \mathrm{Re_b} \rangle_H$ approaches 40 in the center of the vertical domain by $t = 10$. Thus, according to the criterion specified by Gibson, the simulated flow is in fact actively generating turbulent motions. It is also interesting to note the dip in $\langle \mathrm{Re_b} \rangle_H$ at $z = 0$, which occurs at the same location as the dip in $\langle S^2 \rangle_H$ (Figure 4.11), suggesting a strong role of S^2 in the formation of turbulent motions.

Figure 4.41(a), contains a plot of the volume averaged $\langle \mathrm{Re_b} \rangle$ for each ξ. Similar to Figure 4.40(a), the maximum value of $\langle \mathrm{Re_b} \rangle$ is less than the 21.5 needed for active turbulence to form. Also, at $t = 10$, the maximum $\langle \mathrm{Re_b} \rangle_H$ is between 22 and 40 (Figure 4.41(b)), indicating active turbulence formation. The rapid rise in $\langle \mathrm{Re_b} \rangle$ for $\xi = 4$ is attributed to the behavior of $\langle \varepsilon \rangle$, which increases rapidly due to the shear caused in the region where overturning flow intersects with strongly stratified flow.

4.5.5 Vertical shear vs. kinetic energy dissipation rate

In field studies, $\widetilde{\varepsilon}$ is usually inferred from measurements of one or two components of the strain rate tensor $\tilde{e}_{ij}$. In strong, stable density stratification, it is often assumed that $\widetilde{S}^2$ causes most of $\widetilde{\varepsilon}$, leading to the following relationship:

$$\tilde{\nu}\widetilde{S}^2 \approx \widetilde{\varepsilon}. \tag{4.37}$$

While the ratio $\tilde{\nu}\widetilde{S}^2/\widetilde{\varepsilon} \approx 0.9$ has been shown to hold for a large range of Reynolds numbers [Fincham et al., 1996, Praud et al., 2005], in §3.4.1 of this document the above relation was found to be true only when $\mathrm{Re_b} < \mathcal{O}(1)$. Figure 4.42 contains plots of the volume averaged quantity $\tilde{\nu} \left\langle \widetilde{S}^2 \right\rangle / \langle \widetilde{\varepsilon} \rangle$ vs. $\langle \mathrm{Re_b} \rangle$ for (a) several $\mathrm{Re_r}$, $\xi = 0.01$, and (b) several ξ, $\overline{\mathrm{F}}_r = 2.75$, $\mathrm{Re_r} = 19200$. In each plot, the heavy dashed line signifies the value $\tilde{\nu} \left\langle \widetilde{S}^2 \right\rangle / \langle \widetilde{\varepsilon} \rangle = 0.26$,

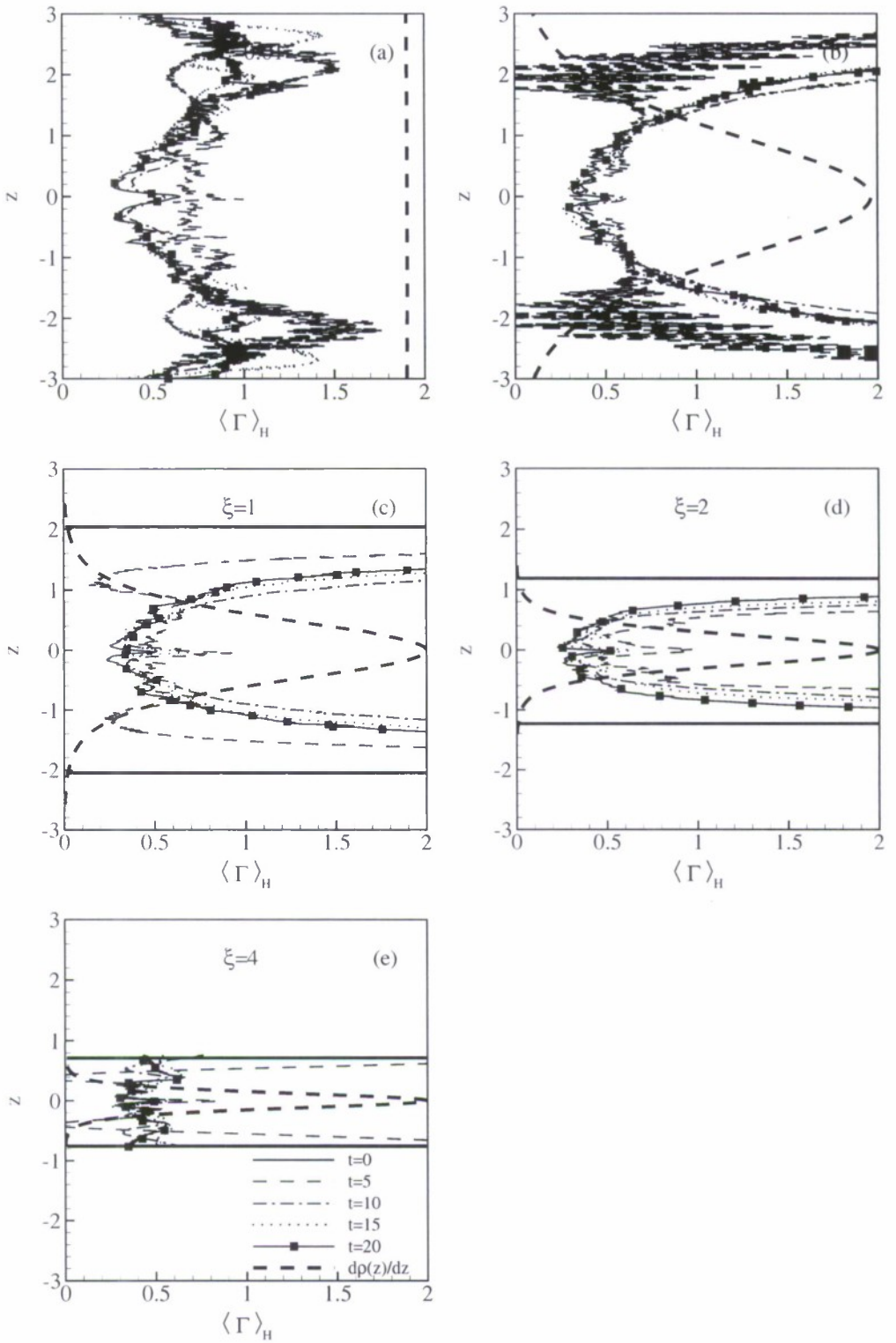

Figure 4.39: Evolution of $\langle \Gamma \rangle_H$ for each ξ. $d\bar{\rho}(z)/dz$ is shown as bold dashed line, and is scaled differently in each figure for comparison. Bold horizontal lines mark where $d\bar{\rho}(z)/dz = -0.01$. Since the entire vertical domain satisfies this criterion for plots (a)-(b), no bold horizontal lines are shown.

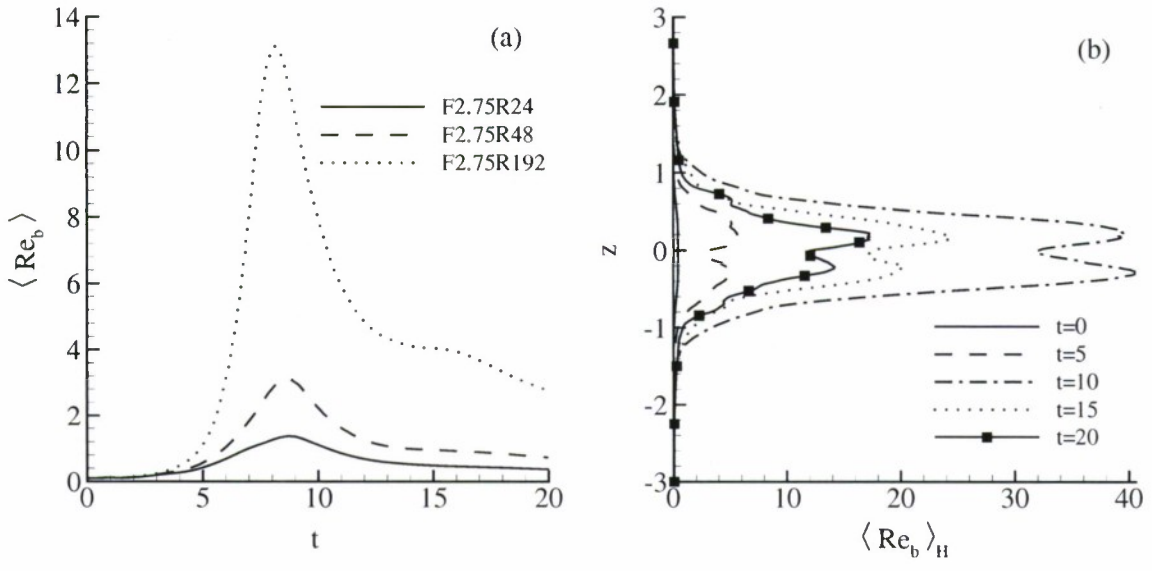

Figure 4.40: (a) $\langle \mathrm{Re_b} \rangle$ for several $\mathrm{Re_r}$. (b) $\langle \mathrm{Re_b} \rangle_H$ for F2.75R192.

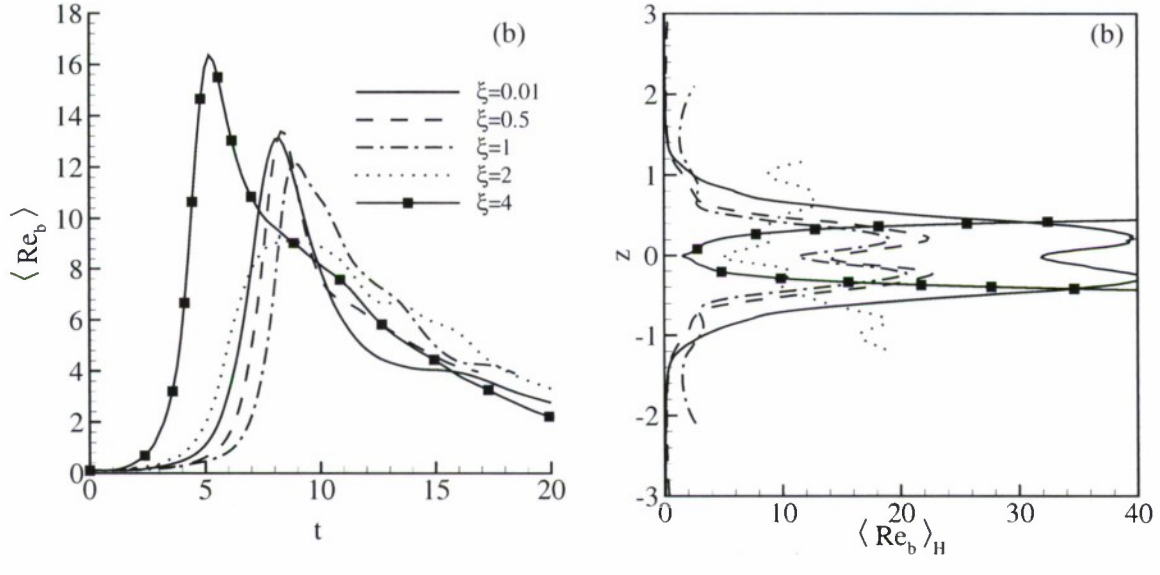

Figure 4.41: (a) $\langle \mathrm{Re_b} \rangle$ for each ξ, $\overline{\mathrm{F}}_r = 2.75$, $\mathrm{Re_r} = 19200$. (b) $\langle \mathrm{Re_b} \rangle_H$ for all ξ, t=10.

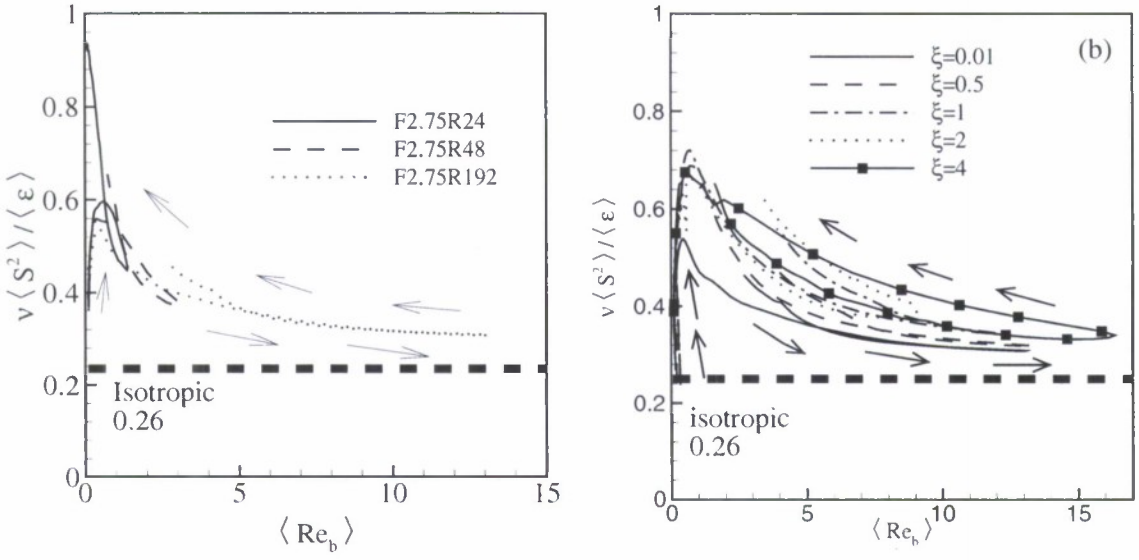

Figure 4.42: $\tilde{\nu}\left\langle \widetilde{S}^2 \right\rangle / \langle \widetilde{\varepsilon} \rangle$ vs. $\mathrm{Re_b}$ for several $\mathrm{Re_r}$.

which is the approximate value expected if the flow were isotropic [Hinze, 1975]. As in §3.4.1, $\langle \mathrm{Re_b} \rangle$ increases to above 1 as the flow evolves and turbulence forms. Correspondingly, $\tilde{\nu}\left\langle \widetilde{S}^2 \right\rangle / \langle \widetilde{\varepsilon} \rangle$ decreases to below 0.5, signifying $\widetilde{S}^2$ accounts for less than half the kinetic energy dissipation rate. (Note that with the influence of gravity on stratified flows, isotropy is not expected, hence $\nu \langle S^2 \rangle / \langle \varepsilon \rangle$ should not reach the isotropic limit). Then, as the flow decays, $\langle \mathrm{Re_b} \rangle$ decreases, and the ratio $\nu \langle S^2 \rangle / \langle \varepsilon \rangle$ increases.

In order to see if (4.37) holds locally, the quantity $\tilde{\nu}\left\langle \widetilde{S}^2 \right\rangle_H / \langle \widetilde{\varepsilon} \rangle_H$ is shown in Figure 4.43. In comparing with Figure 4.41(b), one can see that locally, $\tilde{\nu}\left\langle \widetilde{S}^2 \right\rangle_H / \langle \widetilde{\varepsilon} \rangle_H \approx 0.8$ only for $\xi = 4$, where $\langle \mathrm{Re_b} \rangle_H < 1$.

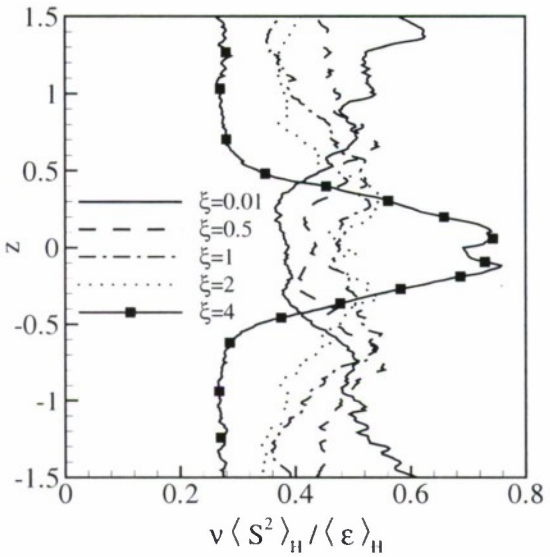

Figure 4.43: $\tilde{\nu}\left\langle \widetilde{S}^2 \right\rangle_H / \langle \widetilde{\varepsilon} \rangle_H$ for each ξ at $t = 10$.

Chapter 5

Summary and Suggested Future Work

5.1 Summary

5.1.1 Uniform Density Stratification

A series of high-resolution direct numerical simulations are used to investigate turbulence in stably stratified flows. The simulated flows are dominated by vortical modes and decay in time since there is no input of energy from the mean flow. In this regime, the Froude number decreases and the Reynolds number increases in time so that a strongly stratified flow with turbulence eventually develops except when the initial Reynolds number is extremely low. The predominant cause of turbulence in the simulations is Kelvin-Helmholtz instabilities that result when the flow organizes itself into quasi-horizontal vortices that are weakly coupled in the vertical direction.

This observation that shear instabilities are the primary trigger for turbulence in the simulations supports the theoretical derivation of the $F_h^2 Re_h$ parameterization developed in Riley and de Bruyn Kops [2003], namely that $1/F_h^2 Re_h$ is related to the Richardson number, so when $F_h^2 Re_h > \mathcal{O}(1)$ turbulence can be expected. To test this hypothesis, the horizontal length scale, L_h, on which F_h and Re_h are based, is defined as the correlation length of the horizontal velocity. When this definition is used it is observed that L_h, F_h, and Re_h all evolve in time consistently with theoretical predictions for all of the simulation cases. Furthermore, $1/F_h^2 Re_h \approx Ri$ over a two decade span of Richardson numbers. This result encourages the thought that $F_h^2 Re_h$ can be used *a priori* to estimate if a laboratory or simulated flow will involve considerable turbulence provided that the correlation length of the horizontal velocity can be estimated from the initial and boundary conditions for the flow.

$F_h^2 Re_h$ is compared with the buoyancy Reynolds number for all the simulation cases, and it is found that the two quantities are nearly the same. While Re_b is traditionally defined as the ratio of the overturning length scale to the viscous length scale, the fact that $F_h^2 Re_h \sim Re_b$ suggests that a shear-based argument might be used to better explain why Re_b has proven to be a useful parameterization. Also, since $F_h^2 Re_h$ involves the number of dimensionless groups predicted by dimensional analysis, it encourages considering turbulence in stratified flows as occurring when the Froude and Reynolds numbers are in some region of the two-dimensional Froude-Reynolds number space rather than when the buoyancy Reynolds number is above some transition value.

Finally, it is found that the contribution of vertical shear to the total dissipation rate of kinetic energy is a strong function $\langle \mathrm{Re_b} \rangle$. The simulation results, taken in conjunction with the laboratory experiments of Fincham et al. [1996] and Praud et al. [2005], indicate that the relation $\nu \langle S^2 \rangle / \langle \varepsilon \rangle \approx 0.9$ only applies when $\langle \mathrm{Re_b} \rangle$ is order one or less. For higher values of $\langle \mathrm{Re_b} \rangle$, normal strains make a significant contribution to $\langle \varepsilon \rangle$ and $\langle S^2 \rangle$ is not well correlated with $\langle \varepsilon \rangle$. As a result, field measurement of only one or two components of the strain rate in the ocean can lead to under-prediction of the true dissipation rate by as much as a factor of 7.

5.1.2 Nonuniform Density Stratification

Simulations are conducted for flows initialized with a von Kármán vortex street and no mean velocity or shear, similar to a momentumless wake. Each simulation was subject to a non-uniform density stratification which resembles the stratification found in natural settings such as a thermohaline staircase. A method is derived to determine available potential energy for this particular flow, followed by analysis of flow energetics. For each simulation, the overall change in density with height is the same, but the wake height relative to the density layer is altered. The results are also compared to a simulated flow in which no density stratification is present.

The simulated density stratified flows in which the wake height is less than or equal to twice the density layer height ($\xi \leq 2$) are shown to agree with the current understanding of density stratified flows. This includes growth of horizontal length scales and decrease in vertical length scales as the flow evolves, in agreement with the scaling arguments of Riley et al. [1981] and the horizontal layer decoupling heuristic by Lilly [1983]. However, when the wake is greater that twice the density layer height ($\xi > 2$), the importance of the density stratification is diminished, and the flow begins to demonstrate characteristics of non-stratified flows. That is, E_H dissipates faster and E_V, ε, and χ demonstrate rapid increases in magnitude. The transition point of $\xi \geq 2$ suggests that it is the relation of the local energy profile to the density layer, rather than velocity profile, that will determine if the flow will behave in a stratified manner.

The results also demonstrate that when a sharp, localized density gradient exists, assuming a uniform density gradient will under-report $\langle \varepsilon \rangle$ up to 25%, while over-reporting $\langle \chi \rangle$ by as much as 50%. This may help explain errors in the reporting of energy budgets from general circulation models currently in use. In addition, it has been shown that available potential energy, E_P, and potential energy dissipation rate, χ, are confined to the area of density stratification. Thus, when $\xi \geq 2$, the volume averaged $\langle E_P \rangle$ drops, while locally $\langle E_P \rangle_H$ is similar in magnitude for all ξ.

Finally, the mixing efficiency $\langle \Gamma \rangle$ is shown to drop significantly when $\xi \geq 2$. However, since χ is zero when there is no stratification, the average mixing efficiency inside the stratification region Γ_{STRAT} was computed. Γ_{STRAT} was found to be between 0.3 and 0.5 for all simulations, which is in agreement with previous studies of uniformly stratified fluids. Also, the notion that Γ will be confined to the area of density stratification by definition lends support to the results of St. Laurent and Schmitt [1999], in which large values of Γ are reported in regions where salt fingering occurs.

5.2 Suggested Future Work

5.2.1 Scales of Motion

Turbulent flows subject to strong stable stratification evolve differently from flows in which the stabilizing effect of gravity is either absent or negligible. Two reasons for this are (1) potential energy plays an important role in stratified flows and (2) stably stratified flows tend to be quasi-two-dimensional and hence lose less kinetic energy to heat through viscous mechanisms than similar unstratified flows. While these two differences between stratified and unstratified turbulence are readily apparent, just how they and other phenomena affect the flow dynamics, and the implications with respect to our ability to predict stably stratified turbulence, is not well understood. For example, questions remain as to what scales energy is converted from one form to another, e.g., from potential to kinetic, kinetic to heat, etc. Also, there is a question of how the scales of motion are affected when exposed to different density stratifications. The above questions can be examined using direct numerical simulations, since all terms in the momentum and density equations are directly computed, and all dynamically relevant scales of the flow are adequately resolved. (This is not to say that DNS can be used for large scale simulations, for which the required spatial resolution to perform a DNS makes such simulations impractical. Rather, DNS is a powerful tool when used for the appropriate sized case.) It is also of interest to compare how flow energetics differ (if at all) between the Taylor-Green and vortex street simulations.

5.2.2 Turbulent Patch Identification and Tracking

Turbulence in density stratified flows tends to form in intermittent patches, and requires a large number of data points to adequately describe the flow characteristics [Baker and Gibson, 1987, Gibson, 1981]. Also, it is in these turbulent patches that the majority of quantities of interest occur, including mixing and dissipation of energy. The ability to identify and track turbulent patches could lead to further insight into fundamental turbulent processes. Attempts at identifying turbulent structures have been made by using wavelet analysis [e.g., Dallman et al., 1999, Farge, 1992, Katul and Vidakovic, 1998], which is similar to the filtering process of large eddy simulations (LES). The difference is that while LES separates the fields in large and small scales, wavelet analysis separates the field into Gaussian and non-Gaussian components [Goldstein et al., 2000]. The Gaussian component represents random noise, while the non-Gaussian components represents coherent structures. A drawback of this method is that the portion of the flow identified as a turbulent structure is dependent on the type of wavelet filter used (e.g., Haar, Donoho, etc.) and the level of filtering applied, leaving the selection of coherent structures a subjective process. A more objective method would remove much of the arbitrariness involved in the wavelet method, and perhaps yield clearer turbulent phenomena insight.

Appendix A

Equation of state for seawater

The equation of state for the density of seawater (ρ) is given in terms of potential temperature ($\widetilde{\Theta}^oC$), practical salinity ($\widetilde{S}$, in practical salinity units), and pressure ($\tilde{p}$, in bars) [Millero and Poisson, 1981]:

$$\rho(\widetilde{S},\widetilde{\Theta},\tilde{p}) = \rho(\widetilde{S},\widetilde{\Theta},0)/[1-\tilde{p}\widetilde{K}(\widetilde{S},\widetilde{\Theta},\tilde{p})]\,, \tag{A.1}$$

where $\rho(\widetilde{S},\widetilde{\Theta},0)$ is the density at reference pressure of zero bars, and and $\widetilde{K}$ is the secant bulk modulus:

$$\begin{aligned}
\rho(\widetilde{S},\widetilde{\Theta},0) &= 999.842594 + 6.793952\times10^{-2}\widetilde{\Theta} - 9.09529\times10^{-3}\widetilde{\Theta}^2 \\
&\quad +1.001685\times10^{-4}\widetilde{\Theta}^3 - 1.120083\times10^{-6}\widetilde{\Theta}^4 + 6.536332\times10^{-9}\widetilde{\Theta}^5 \\
&\quad +8.24493\times10^{-1}\widetilde{S} - 4.0899\times10^{-3}\widetilde{S}\widetilde{\Theta} + 7.6438\times10^{-5}\widetilde{\Theta}^2\widetilde{S} \\
&\quad -8.2467\times10^{-7}\widetilde{\Theta}^3\widetilde{S} + 5.3875\times10^{-9}\widetilde{\Theta}^4\widetilde{S} - 5.72466\times10^{-3}\widetilde{S}^{1.5} \\
&\quad +1.0227\times10^{-4}\widetilde{\Theta}\widetilde{S}^{1.5} - 1.6546\times10^{-6}\widetilde{\Theta}^2\widetilde{S}^{1.5} + 4.8314\times10^{-4}\widetilde{S}^2
\end{aligned}$$

$$\begin{aligned}
\widetilde{K}(\widetilde{S},\widetilde{\Theta},\tilde{p}) &= 19652.21 + 148.4206\widetilde{\Theta} - 2.327105\widetilde{\Theta}^2 + \\
&\quad 1.360477\times10^2\widetilde{\Theta}^3 - 5.155288\times10^5\widetilde{\Theta}^4 + 3.239908\tilde{p} \\
&\quad +1.43713\times10^3\widetilde{\Theta}\tilde{p} + 1.16092\times10^4\widetilde{\Theta}^2\tilde{p} - 5.77905\times10^7\widetilde{\Theta}^3\tilde{p} \\
&\quad +8.50935\times10^5\tilde{p}^2 - 6.12293\times10^6\widetilde{\Theta}\tilde{p}^2 + 54.6746\widetilde{S} \\
&\quad -0.603459\widetilde{\Theta}\widetilde{S} + 1.09987\times10^2\widetilde{\Theta}^2\widetilde{S} - 6.167\times10^5\widetilde{\Theta}^3\widetilde{S} \\
&\quad +7.944\times10^2\widetilde{S}^{1.5} + 1.6483\times10^2\widetilde{\Theta}\widetilde{S}^{1.5} - 5.3009\times10^4\widetilde{\Theta}^2\widetilde{S}^{1.5} \\
&\quad +2.2838\times10^3\tilde{p}\widetilde{S} - 1.0981\times10^5\widetilde{\Theta}\tilde{p}\widetilde{S} - 1.6708\times10^6\widetilde{\Theta}^2\tilde{p}\widetilde{S} \\
&\quad +1.91075\times10^4\tilde{p}\widetilde{S}^{1.5} - 9.9348\times10^7\tilde{p}^2\widetilde{S} + 2.0816\times10^8\widetilde{\Theta}\tilde{p}^2\widetilde{S} \\
&\quad +9.1697\times10^{10}\widetilde{\Theta}^2\tilde{p}^2\widetilde{S};
\end{aligned}$$

Bibliography

D. Altman and A. Gargett. Differential property transport due to incomplete mixing in a stratified fluid. In E. List and G. Jirka, editors, *Stratified Flows*, pages 454–460. American Society of Civil Engineers, 1990.

Mark A. Baker and Carl H. Gibson. Sampling turbulence in the stratified ocean: statistical consequences of strong intermittency. *J. Phys. Oceanogr.*, 17, 1987.

P. Billant and J. M. Chomaz. Three-dimensional stability of a vertical columnar vortex pair in a stratified fluid. *J. Fluid Mech.*, 419:65–91, 2000a.

P. Billant and J. M. Chomaz. Experimental evidence for a new instability of a vertical columnar vortex pair in a strongly stratified fluid. *J. Fluid Mech.*, 418:167–188, 2000b.

P. Billant and J. M. Chomaz. Self-similarity of strongly stratified inviscid flows. *Phys. Fluids*, 13:1645–1651, 2001.

R. B. Bird, W. E. Stewart, and E. N. Lightfoot. *Transport Phenomena*. John Wiley and Sons, second edition, 2002.

M. Bonnier, P. Bonneton, and O. Eiff. Far-wake of a sphere in a stably stratified fluid: Characterization of the vortex structures. *Applied Scientific Researeh*, 59:269–281, 1998.

J. Boussinesq. *Théorie analytique de la ehaleur*, volume 2, p. 172. Gauthier-Villars, Paris, 1903.

J. D. Boyd. Properties of thermal staircase off the northeast coast of South America. *J. Geophys. Res.*, 94:8303–8312, 1989.

J. P. Boyd. *Chebyshev and Fourier Speetral Methods*. Dover, 2001.

G. Brasseur and S. Solomon. *Aeronomy of the middle atmosphere*. D. Reidel Publishing Company, Holland, 1984.

D. Cacchione and C. Wunsch. Experimental study of internal waves over a slope. *J. Fluid Meeh.*, 66:223–239, 1974.

D. A. Cacchione and J. B. Southard. Incipient sediment movement by shoaling internal gravity waves. *J. Geophys. Res.*, 79:2237–2242, 1974.

W. Chang, F. Giraldo, and B. Perot. Analysis of an exact fractional step method. *J. Comput. Phys.*, 180(1):183–199, 2002.

J.-M. Chomaz, P. Bonneton, A. Butet, and E. J. Hopfinger. Vertical diffusion of the far wake of a sphere moving in a stratified fluid. *Phys. Fluids A*, 5:2799, 1993.

Angela Colling, editor. *Ocean Circulation.* Butterworth-Heinemann, Oxford, England, 2nd edition, 2002.

U. C. Dallman, H. Volmers, and W. Su. Flow topology and tomography for vortex identification in unsteady and three-dimensional flows. In J. N. Sorensen, E. J. Hopfinger, and N. Aubry, editors, *Simulation and identificaiton of organized structures in Flows: Proc. IUTAM Symp*, pages 223–233. Kluwer, 1999.

S. M. de Bruyn Kops, J. J. Riley, and K. B. Winters. Reynolds and Froude number scaling in stably-stratified flows. In *Reynolds Number Scaling in Turbulent Flow.* Kluwer, 2003.

A. J. Elliot and R. I. Tait. On the steady-state nature of mediterranean outflow step structure. In M. V. Angel, editor, *A voyage of discovery*, pages 213–220. New York:Pergamon Press, 1977.

C. C. Eriksen. Observation of internal wave reflection off sloping bottoms. *J. Geophys. Res.*, 87(C1):525–538, 1982.

C. C. Eriksen. Implications of ocean bottom reflection for internal wave spectra and mixing. *J. Phys. Oceanogr.*, 15(9):1145–1156, 1985.

C. C. Eriksen. Internal wave reflection and mixing at fieberling guyot. *J. Geophys. Res.-Oceans*, 103(C2):2977–2994, 1998.

M. Farge. Wavelet transforms and their applications to turbulence. *Annu. Rev. Fluid Mech.*, 24:395–457, 1992.

A. M. Fincham, T. Maxworthy, and G. R. Spedding. Energy dissipation and vortex structure in freely decaying, stratified grid turbulence. *Dyn. Atmos. Oceans*, 23:155–169, 1996.

J. B. Flor, G. J. F. van Heijst, and R. Delfos. Experimental study of dipolar vortex structures in a stratified fluid. *J. Fluid Mech.*, 7:374–383, 1995.

N. P. Fofonoff and R. C. Millard, Jr. Algorithms for computation of fundamental properties of seawater. In *Unesco technical papers in marine science*, number 44, pages 1–53. 1983.

A. E. Gargett. Differential diffusion: an oceanographic primer. *Prog. Oceanogr.*, 56:559–570, 2003.

A. E. Gargett. The scaling of turbulence in the presence of stable stratification. *J. Geophys. Res.*, 93(C5):5021–5036, 1988.

A. E. Gargett and J. N. Moum. Mixing efficiencies in turbulent tidal fronts - results from direct and indirect measurements of density flux. *J. Phys. Oceanogr.*, 25:2583–2608, 1995.

A. E. Gargett, W. J. Merryfield, and G. Holloway. Direct numerical simulation of differential scalar diffusion in three-dimensional stratified turbulence. *J. Phys. Oceanogr.*, 33:1758–1782, 2003.

J. F. Garten, S. Arendt, D. C. Fritts, and J. Werne. Dynamics of counter-rotating vortex pairs in stratified and sheared environments. *J. Fluid Mech.*, 361:189–236, 1998.

C. H. Gibson. Fossil turbulence, salinity, and vorticity turbulence in the ocean. In J. C.J. Nihous, editor, *Marine Turbulence*, pages 221–257. Elsevier, 1980.

Carl H. Gibson. Buoyancy effects in turbulent mixing: Sampling turbulence in the stratified ocean. *AIAA Journal*, 19(11):1394–1400, 1981.

Carl H. Gibson. Fossil turbulence and intermittency in sampling oceanic mixing processes. *J. Geophys. Res.*, 92(C5):5383–5404, 1987.

E. Gill. *Atmossphere-Ocean Dynamics*. Academic Press, 1982.

D. E. Goldstein, O. V. Vasilyev, A. A. Wray, and R. S. Rogallo. Evaluation of the use of second generation wavelets in the coherent vortex simulation approach. *Center for Turbulence Research, Stanford University - Proceedings of the summer program 2000*, pages 293–304, 2000.

M. C. Gregg. Diapycnal mixing in the thermocline – a review. *J. Geophys. Res.–Oceans*, 92:5249–5286, 1987.

M. C. Gregg. Scaling turbulent dissipation in the thermocline. *J. Geophys. Res.*, 94:9686–9698, 1989.

M. C. Gregg and T. Sanford. Shear and turbulence in a thermohaline staircase. *Deep-Sea Research*, 34:1689–1696, 1987.

J. R. Herring and O. Métais. Numerical experiments in forced stably stratified turbulence. *J. Fluid Mech.*, 202:97, 1989.

J. O. Hinze. *Turbulence*. McGraw-Hill, New York, 2nd edition, 1975.

D. Holliday and M. McIntyre. On potential energy density in an incompressible, stratified fluid. *J. Fluid Mech.*, 107:221–225, 1981.

S. L. Howard, J. Hyatt, and L. Padman. Mixing in the pycnocline over the western Antarctic Peninsula shelf during Southern Ocean GLOBEC. *Deep Sea Research II*, 51:1965–1979, 2004.

Jörg Imberger and Boualem Boashash. Application of the Winger-Ville distribution to temperature gradient microstructure: A new technique to study small-scale variations. *J. Phys. Oceanogr.*, 16:1997–2012, 1986.

G. N. Ivey and J. Imberger. On the nature of turbulence in a stratified fluid. part 1: The energetics of mixing. *J. Phys. Oceanogr.*, 21:650–658, 1991.

G. N. Ivey and R. I. Nokes. Vertical mixing due to the breaking of critical internal waves on sloping boundaries. *J. Fluid Mech.*, 204:479–500, 1989.

P. R. Jackson and C. R. Rehmann. Laboratory measurements of differential diffusion in a diffusively stable, turbulent flow. *J. Phys. Oceanogr.*, 33:1592–1603, 2003.

Gabriel Katul and Brandi Vidakovic. Identification of low-dimensional energy containing / flux transporting eddy motion in the atmospheric surface layer using wavelet thresholding methods. *J. Atmos. Sci.*, 55:377–389, 1998.

D. E. Kelley. Explaining effective siffusivities within diffusive ocean staircases. In J. C. H. Nihoul and B. M. Jamart, editors, *Small Scale Turbulence and Mixing in the Ocean, Proceedings of the 19th International Liege Colloquium on Ocean Hydrodynamics*, volume 46, page 19889898. Elsevier, 1987.

R. M. Kerr. Higher-order derivative correlations and the alignment of small-scale structures in isotropic turbulence. *J. Fluid Mech.*, 153(31):31, 1985.

Pijush K. Kundu and Ira M. Cohen. *Fluid Mechanics.* Academic Press, 2nd edition, 2002.

K. G. Labitzke and H van Loon. *The stratosphere: phenomena, history, and relevance.* Springer, 1999.

R. B. Lambert and W. Sturges. A thermohaline staircase and vertical mixing in the thermocline. *Deep-Sea Research*, 24:211–222, 1977.

D. K. Lilly. Stratified turbulence and the mesoscale variability of the atmosphere. *J. Atmos. Sci.*, 40:749–761, 1983.

E. Lindborg. The energy cascade in a strongly stratified fluid. *J. Fluid Mech.*, 550:207–242, 2006.

P. N. Lombard and J. J. Riley. Instability and breakdown of internal gravity waves. I. Linear stability analysis. *Phys. Fluids*, 8:3271, 1996a.

P. N. Lombard and J. J. Riley. On the breakdown into turbulence of propagating internal waves. *Dyn. Atmos. Ocean.*, 23:345, 1996b.

E. N. Lorenz. Available potential energy and the maintenance of the general circulation. *Tellus*, 7:157–167, 1955.

F. K. Lutgens and E. J. Tarbuck. *The atmosphere: an introduction to meteorologly.* Prentice Hall, New Jersey, 1995.

G. O. Marmorino. Observations of small-scale mixing processes in the seasonal thermocline. Part i: Salt fingering. *J. Phys. Oceanogr.*, 17:1339–1347, 1987.

G. O. Marmorino and D. R. Caldwell. Heat and salt transport through a diffusive thermohaline interface. *Deep Sea Research*, 23:59–67, 1976.

T. McDougal, S. Thorpe, and C. Gibson. Small-scale turbulence and mixing in teh ocean: a glossary. In J.C.H Nihoul and B. M. Jamart, editors, *Small Scale Turbulence and Mixing in the Ocean, Proceedings of the 19th International Liege Colloquium on Ocean Hydrodynamics*, volume 46, pages 3–9. Elsevier, 1988.

P. Meunier and G. Spedding. Stratified propelled wakes. *J. Fluid Mech.*, 522:229–256, 2006.

F. J. Millero and A. Poisson. International one-atmosphere equation of state of seawater. *Deep-Sea Research*, 28A:625–625, 1981.

R. Molcard and R. I. Tait. The steady state of the step structure in the Tyrrhenian Sea. In M. V. Angel, editor, *A voyage of discovery*, pages 221–233. New York:Pergamon Press, 1977.

J. N. Moum. The quest for κ_ρ – preliminary-results from direct measurements of turbulent fluxes in the ocean. *J. Phys. Oceanogr.*, 20:1980–1984, 1990.

J. N. Moum. Energy-containing scales of turbulence in the ocean thermocline. *J. Geophys. Res.-Oceans*, 101:14095–14109, 1996.

T. R. Osborn. Estimates of the local-rate of vertical diffusion from dissipation measurements. *J. Phys. Oceanogr.*, 10:83–89, 1980.

R. V. Ozmidov. On the turbulent exchange in a stable stratified ocean. *Izv. Atmospheric and Oceanic Physics*, 1:493–497, 1965.

Ronald L. Panton. *Incompressible Flow*. John Wiley and Sons, 2nd edition, 1996.

W. R. Peltier and C. P. Caulfield. Mixing efficiency in stratified shear flows. *Annu. Rev. Fluid Mech.*, 35:135–167, 2003.

J. B. Perot. An analysis of the fractional step method. *J. Comput. Phys.*, 108:51–58, 1993.

O. Praud and A. M. Fincham. The structure and dynamics of stratified dipolar vorticies. *J. Fluid Mech.*, 2003.

O. Praud, A. M. Fincham, and J. Sommeria. Decaying grid turbulence in a strongly stratified fluid. *J. Fluid Mech.*, 522:1–33, 2005.

J. J. Riley and S. M. de Bruyn Kops. Dynamics of turbulence strongly influenced by buoyancy. *Phys. Fluids*, 15(7):2047–2059, 2003.

J. J. Riley and M. P. Lelong. Fluid motions in the presence of strong stable stratification. *Annu. Rev. Fluid Mech.*, 32:613–657, 2000.

J. J. Riley, R. W. Metcalfe, and M. A. Weissman. Direct numerical simulations of homogeneous turbulence in density stratified flows. In B. J. West, editor, *Proc. AIP Conf. Nonlinear Properties of Internal Waves*, pages 79–112, New York, 1981. American Institute of Physics.

R. Robertson, L. Padman, and M. D. Levine. Finestructure, microstructure, and vertical mixing processes in the upper ocean in the western wedell sea. *JGR*, 100:18517–18536, 1995.

B. Ruddick and A. E. Gargett. Oceanic double-diffusion: introduction. *Progress in Oceanography*, 56:381–393, 2003.

R. W. Schmitt. Observational and laboratory insights into salt finger convection. *Progress in Oceanography*, 56:419–433, 2003.

R. W. Schmitt. Form of the temperature - salinity relationship in the central water: evidence for double-diffusive mixing. *J. Phys. Oceanogr.*, 11(7):1015–1026, 1981.

R. W. Schmitt. Mixing in a thermohaline staircase. In J.C.H Nihoul and B. M. Jamart, editors, *Small Scale Turbulence and Mixing in the Ocean, Proccedings of the 19th International Liee Colloquium on Ocean Hydrodynamics*, volume 46, pages 435–452. Elsevier, 1988.

R. W. Schmitt. Double diffusion in oceanography. *Annu. Rev. Fluid Mech.*, 26:255–285, 1994.

R. W. Schmitt, H. Perkins, J. D. Boyd, and M. C. Stalcup. C-SALT: An investigation of the thermohaline staircase in the western tropical North Atlantic. *Deep-Sea Research*, 34:1655–1665, 1987.

Lucinda H. Shih, Jeffrey R. Koseff, Gregory N. Ivey, and Joel H. Ferziger. Parameterization of turbulent fluxes and scales using homogeneous sheared stably stratified turbulence simulations. *J. Fluid Mech.*, 525:193–214, 2005.

D. N. Slinn and J. J. Riley. Turbulent mixing in the oceanic boundary layer caused by internal wave reflection from sloping terrain. *Dyn. Atmos. Oceans*, 24:51–62, 1996.

D. N. Slinn and J. J. Riley. Turbulent dynamics of a critically reflecting internal gravity wave. *Theor. Comp. Fluid Dyn.*, 11:281–303, 1998.

W. D. Smyth and J. N. Moum. Length scales of turbulence in stably stratified mixing layers. *Phys. Fluids*, 12:1327–1342, 2000a.

W. D. Smyth and J. N. Moum. Anisotropy of turbulence in stably stratified mixing layers. *Phys. Fluids*, 12:1343–1362, 2000b.

W. D. Smyth, D. Hebert, and J. Moum. Local ocean response to a multiphase westerly wind-busrt. Part2: Thermal and freshwater responses. *J. Gcophys. Res.*, 101:22495–22512, 1996.

W. D. Smyth, J. N. Moum, and D. R. Caldwell. The efficiency of mixing in turbulent patches: inferences from direct simulations and microstructure observations. *J. Phys. Oceanogr.*, 31:1969–1992, 2001.

W. D. Smyth, J. D. Nash, and J. N. Moum. Differential diffusion in breaking Kelvin-Helmholtz billows. *J. Phys. Oceanogr.*, 35:1004–1022, 2005.

G. R. Spedding. Vertical structure in stratified wakes at high initial froude number. *J. Fluid Mech.*, 454:71, 2002.

G. R. Spedding, F. K. Browand, and A. M. Fincham. The long-time evolution of the initially-turbulent wake of a sphere in a stable stratification. *Dyn. Atmos. Ocean.*, 23: 171–182, 1996a.

G. R. Spedding, F. K. Browand, and A. M. Fincham. Turbulence, similarity scaling and vortex geometry in the wake of a towed sphere in a stably stratified fluid. *J. Fluid Mech.*, 314:53, 1996b.

E. A. Spiegel and G. Veronis. On the boussinesq approximation for a compressible fluid. *Astro-physical Journal*, 131:442–447, 1960.

L. St. Laurent and R. W. Schmitt. The contribution of salt fingers to vertical mixing in the North Atlantic tracer release experiment. *J. Phys. Oceanogr.*, 29:1404–1424, 1999.

C. Staquet. Mixing in a stably-stratified shear layer: two- and three-dimensional numerical experiments. *Fl. Dyn. Res.*, 27:367, 2000.

M. E. Stern. The "salt fountain" and thermohaline convection. *Tellus*, 12:172–175, 1960.

M. E. Stern. The collective instability of salt fingers. *J. Fluid Mech.*, 35:209–218, 1969.

J. R. Taylor. Turbulence and mixing in teh boundary layer generated by shoaling internal waves. *Dyn. Atmos. Oceans*, 23:233–258, 1993.

S. A. Thorpe. Turbulence and mixing in a Scottish loch. *Philos. Trans. Roy. Soc. London*, A286:125–181, 1977.

L. N. Trefethen. *Spectral methods in MATLAB*. SIAM, Philadelphia, PA, 2000.

Yu-heng Tseng and J. H. Ferziger. Mixing and available potential energy in stratified flows. *Phys. Fluids*, 13(5):1281–1293, 2001.

J. Turner. The influence of molecular diffusivity on turbulent entrainment across a density interface. *J. Fluid Mech.*, 317:179–193, 1968.

J. S. Turner. *Buoyancy Effects in Fluids*. Cambridge University Press, 1973.

S. I. Voropayev and Ya. D. Afanasyev. Two-dimensional vortex-dipole interactions in a stratified fluid. *J. Fluid Mech.*, 236:665–689, 1992.

A. J. Williams. Salt fingers observed in the Mediterranean outflow. *Science*, 185:941–943, 1974.

K. B. Winters, P. N. Lombard, J. J. Riley, and E. A. D'Asaro. Available potential energy and mixing in density-stratified fluids. *J. Fluid Mech.*, 289:115–128, 1995.